

Theoretical and experimental
investigation of III-V semiconductor
nanowire heterostructures



Andrew Peter Foster

Department of Physics and Astronomy

University of Sheffield

A thesis submitted for the degree of

Doctor of Philosophy

November 2013

Abstract

This thesis concerns a theoretical and experimental investigation of two applications of semiconductor nanowires and nanowire heterostructures. First, the development of nanowire-planar tandem solar cells is considered from a theoretical standpoint. The maximum efficiency of the solar cell is determined in the radiative limit as a function both of the material bandgaps and the absorption efficiency of the nanowire array. This work provides design guidelines for the experimental realisation of such a solar cell.

The catalyst-free growth of GaAs nanowires is then developed, with potential for future use within a nanowire solar cell. Control over radial and axial nanowire growth is demonstrated. GaAs nanowires are employed as the host for single photon emitters in the form of InGaAs nanowire quantum dots. This leverages the position control inherent in the growth technique, and represents the first realisation of individually addressable nanowire quantum dots grown by this technique. This provides a promising route for future scale up for quantum information applications.

The limits of the catalyst-free growth technique are investigated, leading to the first demonstration of morphology control of a catalyst-free nanowire. Nanowires are grown with elongated cross-section, resulting in the emission of linearly polarized light from the top facet of the nanowire.

Finally, the growth of InAsP nanowire quantum dots within InP nanowires is developed. Photoluminescence emission is detected at lower energy than expected for polytypic InP, demonstrating successful growth of an InAsP nanowire heterostructure.

This thesis is dedicated to my parents.

Acknowledgements

I would like to acknowledge the significant input of colleagues without whom this thesis would never have been written: my co-supervisor Andrey Krysa, for letting me use the MOCVD reactor at a moment's notice; Maxim Makhonin, for his patience in the lab and putting the 'quantum' in quantum light emission; Dyfrig Davies for his cleanroom expertise; and Kenny Larsen for introducing me to Linux. My thanks also go to John Bradley and Alex Barrows, for their experimental endeavour, and to the staff of the EPSRC National Centre for III-V Technologies, in particular Paul Fry, Ken Kennedy and Rob Airey.

This research was undertaken whilst I was a member of the E-Futures DTC, funded by EPSRC. I would like to thank Alistair Buckley for pointing me in the right direction; Neil Lowrie, Tony West, Geraint Jewell *et al.* for their hard work in making E-Futures a success; and everyone in E-Futures for making it such an enjoyable time.

It hasn't just been work for the last few years.... my thanks go to everyone in the LDS group both for useful discussions in the office and (less) useful ones on a Friday night! Thanks also for the friendship and encouragement of the many members of the E-House, Blake Street.

Finally, I would like to thank the head of the LDS group, Maurice Skolnick, for allowing me to develop my academic career in the company of experts, and acknowledge the fantastic support of my supervisor Luke Wilson, in particular for his meticulous attention to detail and from whom (I hope!) I have learnt greatly.

Andrew Foster
Sheffield, November 2013.

List of Publications

A.P. Foster and L.R. Wilson (2013) ‘*Design parameters for nanowire-planar tandem solar cells*’ *Physica Status Solidi A* **210** 425-429

M.N. Makhonin[†], **A.P. Foster**[†], A.B. Krysa, P.W. Fry, D.G. Davies, T. Grange, T. Walther, M.S. Skolnick and L.R. Wilson (2013) ‘*Homogeneous array of nanowire-embedded quantum light emitters*’ *Nano Letters* **13**(3) 861-865 ([†] contributed equally to this work)

A.P. Foster, M.N. Makhonin, A.B. Krysa, P.W. Fry, D.G. Davies, T. Grange, T. Walther, M.S. Skolnick and L.R. Wilson ‘*InGaAs nanowire quantum dots*’ Oral presentation, UK Semiconductors, Sheffield, UK, 2012

A.P. Foster, M.N. Makhonin, A.B. Krysa, P.W. Fry, D.G. Davies, T. Grange, T. Walther, M.S. Skolnick and L.R. Wilson ‘*Nanowire-embedded quantum light emitters*’ Poster presentation, QD-7, New Mexico, UK, 2012

A.P. Foster, M.N. Makhonin, A.B. Krysa, P.W. Fry, D.G. Davies, T. Grange, T. Walther, M.S. Skolnick and L.R. Wilson ‘*Homogeneous array of nanowire-embedded quantum light emitters*’ Poster presentation, ICPS-31, Zurich, Switzerland, 2012

A.P. Foster, M.N. Makhonin, A.B. Krysa, P.W. Fry, D.G. Davies, T. Grange, T. Walther, M.S. Skolnick and L.R. Wilson ‘*Homogeneous array of nanowire-embedded quantum light emitters*’ Poster presentation, IOP QD One Day Meeting, Nottingham, UK, 2013

A.P. Foster, J.P. Bradley, M.N. Makhonin, A.B. Krysa, P.W. Fry, D.G. Davies, T. Grange, T. Walther, M.S. Skolnick and L.R. Wilson ‘*Quantum light emitters in semiconductor nanowire arrays*’ Oral presentation, UK Semiconductors, Sheffield, UK, 2013

A.P. Foster, J.P. Bradley, M.N. Makhonin, A.B. Krysa, P.W. Fry, D.G. Davies, T. Grange, T. Walther, M.S. Skolnick and L.R. Wilson ‘*Nanowire-embedded quantum light emitters and linearly polarized sources*’ Oral presentation, ICON-5, Annecy, France, 2013

Contents

Abstract	v
Acknowledgements	ix
List of Publications	xi
List of Figures	xvii
1 Introduction	1
1.1 Background	2
1.1.1 Low dimensional semiconductors	2
1.1.2 Semiconductor nanowires	5
1.1.3 Nanowire crystal structure	7
1.1.4 Semiconductor nanowires for photovoltaics	9
1.1.5 Semiconductor quantum dots	11
1.1.5.1 Semiconductor quantum dot growth	12
1.1.5.2 Energy states and optical properties of quantum dots	13
1.1.5.3 Improving upon standard quantum dot growth techniques	18
1.2 Summary of chapters	19
2 Design considerations for nanowire-planar tandem solar cells	23
2.1 Introduction	23
2.2 Benefits of nanowire arrays for solar cell applications	24
2.2.1 Antireflection and enhanced absorption properties of a nanowire array	24
2.2.2 Lattice mismatched nanowire epitaxy	28
2.2.3 Radial p-n junction in a nanowire	29
2.3 Nanowire solar cells in the literature	30
2.4 Modelling the nanowire-planar tandem solar cell	34

2.4.1	Theory	34
2.4.2	Results	40
2.5	Conclusion	45
3	Fabrication and growth of GaAs nanowire arrays	51
3.1	Introduction	51
3.2	Overview of the growth technique	53
3.3	Fabrication prior to MOCVD growth	55
3.3.1	Step 1: Marker development	55
3.3.2	Step 2: SiO ₂ deposition	56
3.3.3	Step 3: SiO ₂ square definition	57
3.3.4	Step 4: Formation of nanohole arrays	57
3.4	Growth of GaAs nanowires	59
3.4.1	Nanowire growth in the presence of rough planar surface growth	62
3.4.2	Achieving low surface roughness planar epitaxy on (111)B GaAs	68
3.4.3	Nanowire growth in the presence of smooth planar surface growth	69
3.5	Conclusion	72
4	InGaAs nanowire quantum dots	75
4.1	Introduction	75
4.2	Background	76
4.2.1	Position controlled quantum dots	76
4.2.2	Nanowire quantum dots	79
4.3	MOCVD growth of InGaAs NWQDs	82
4.4	Results and discussion	84
4.4.1	Structural characterisation	84
4.4.1.1	Scanning electron microscopy	84
4.4.1.2	Transmission electron microscopy	87
4.4.2	Optical characterisation	91
4.4.2.1	Low power PL measurements	92
4.4.2.2	Evidence for a single NWQD in a single nanowire	95
4.4.2.3	NWQD excited states observation and modelling .	97

4.4.2.4	NWQD PL homogeneity	102
4.4.2.5	NWQDs for quantum computing?	105
4.5	Further work	110
4.5.1	Spectral diffusion measurements	110
4.5.2	In-situ laser annealing of a NWQD	117
4.5.3	NWQD growth studies	119
4.5.3.1	Towards optically coupled NWQDs	120
4.5.3.2	Blueshift of NWQD PL emission	123
4.6	Conclusion	127
5	Morphology control of GaAs nanowires	135
5.1	Introduction	135
5.2	Sample growth	136
5.3	Linearly polarized PL from an elongated nanowire	138
5.3.1	Nanowire morphology control	139
5.3.2	PL measurements	141
5.3.3	Origin of PL polarization	144
5.3.4	Extending the growth concept	149
5.3.5	Limits on nanowire elongation for single mode coupling	150
5.4	Conclusion	153
6	Growth and characterisation of InP nanowires	157
6.1	Introduction	157
6.2	Sample fabrication	158
6.3	Growth of InP nanowires	161
6.3.1	SEM analysis	162
6.3.2	PL measurements	169
6.3.3	Further development	171
6.3.4	Conclusion	174
7	Conclusions and outlook	177
7.1	Chapter summaries	177
7.1.1	Chapter 2	177
7.1.2	Chapter 3	178
7.1.3	Chapter 4	178

7.1.4	Chapter 5	179
7.1.5	Chapter 6	179
7.2	Outlook	181
7.2.1	Nanowire-on-silicon tandem solar cells	181
7.2.2	Control of nanowire crystal structure	182
7.2.3	Exploring the limits of catalyst-free nanowire growth	184
7.2.4	NWQD integration with photonic crystals	186

List of Figures

1.1	Density of conduction band states for semiconductors of reduced dimensionality	3
1.2	Transition from classical to quantum regimes in a semiconductor	4
1.3	Scanning electron microscope image of a GaAs nanowire	5
1.4	Schematics of crystal structures observed in nanowires	7
1.5	Schematic showing twin plane formation in a zinc blende nanowire	8
1.6	Schematic of the nanowire-planar tandem solar cell modelled in Chapter 2	11
1.7	Schematic illustrating the Stranski-Krastanow growth process	13
1.8	Band diagram showing direct and indirect interband transitions in bulk semiconductors	14
1.9	Schematic representation of energy band alignment in type-I and type-II quantum dots	15
1.10	Electron and hole energy states within a QD	16
2.1	Antireflection and enhanced absorption by a nanowire array	26
2.2	Leveraging the nanowire morphology for solar cell applications	29
2.3	Efficiency limits for a tandem solar cell formed from a nanowire array grown on a planar substrate	41
2.4	Efficiency limits for a nanowire array–silicon substrate tandem solar cell	42
2.5	FDTD simulations of the optical properties of a nanowire array on a semi-infinite substrate	44
3.1	Overview of nanowire growth techniques	52
3.2	Overview of fabrication procedure prior to growth of GaAs nanowires	54
3.3	Process steps for etching markers into a GaAs substrate	56
3.4	Schematic overview of MR350 MOCVD reactor	59
3.5	Scanning electron microscope image of a GaAs nanowire	61

3.6	SEM image revealing rough planar growth on the exposed GaAs substrate	63
3.7	Characterisation of Samples 3A–3D	64
3.8	Height versus diameter for the nanowires grown on Sample 3E	67
3.9	Characterisation of Sample 3G	70
3.10	Height and radial growth versus diameter for the nanowires grown on Sample 3H	71
4.1	Schematic overview of the NWQD growth process	80
4.2	SEM analysis of the nanowires grown on Sample 4A	85
4.3	TEM analysis of nanowires containing NWQDs	88
4.4	Low power PL measurements on a single NWQD	93
4.5	PL intensity map for a nanowire lying on the growth substrate	96
4.6	Modelling NWQD PL characteristics	98
4.7	Ensemble PL statistics from an array of NWQDs	103
4.8	PL lifetime measurement for a single NWQD	106
4.9	Second order autocorrelation measurement for exciton PL emission from a NWQD	108
4.10	Low power PL measurements on individual NWQDs revealing spectral diffusion effects	112
4.11	<i>Ex-situ</i> radial overgrowth of GaAs nanowires	116
4.12	<i>In-situ</i> laser annealing of a single NWQD	118
4.13	PL emission spectra from a nanowire containing two NWQDs	122
4.14	Observation of blueshift in power dependent PL measurements on NWQDs	125
5.1	Investigation of growth from nanohole pairs	136
5.2	SEM images of elongated nanowires used for polarization measurements	140
5.3	PL spectra from elongated nanowires	141
5.4	Polarization-dependent PL emission from elongated nanowires	143
5.5	Fundamental mode analysis for circular and elliptical cross-section infinite waveguides	145
5.6	Nanowire optical mode analysis	147
5.7	SEM images of elongated nanowires grown from nanoslots	150

5.8	Growth considerations for nanowire morphology control	151
5.9	Schematic proposal for combined VLS and catalyst-free growth of elongated nanowires	153
6.1	Definition of gold markers on an InP substrate	159
6.2	SEM images of Samples 6A and 6B	163
6.3	Nanowire height and diameter versus pitch for Samples 6A and 6B .	165
6.4	SEM images of Samples 6C and 6D	167
6.5	Nanowire height and diameter versus pitch for Samples 6C and 6D .	168
6.6	PL spectra for InP nanowires	170
6.7	SEM images and PL spectra for Sample 6F	173
7.1	Normalised power dependent PL spectra for 100nm diameter InP nanowires with a pitch of 250nm	182
7.2	SEM images of GaAs nanowires	185
7.3	Nanowire integration with a slot photonic crystal cavity	186

1 Introduction

Semiconductor nanowires are the present focus of intense research efforts covering a wide range of fundamental and device physics. These include nanowire photovoltaic devices with the potential to achieve high efficiency^{1,2}, and hosts for single photon sources^{3,4} which are desirable for quantum information applications⁵. Research has been undertaken into nanowires for the realisation of high brightness LEDs⁶, harnessing of optomechanical effects^{7,8} and the first observation⁹ and future manipulation¹⁰ of Majorana fermion-like particles. The large nanowire surface area to volume ratio may be leveraged for sensing applications¹¹ whilst lattice mismatched nanowire growth provides exciting possibilities for the integration of III-V semiconductors with silicon electronics¹².

This thesis concerns the modelling and experimental investigation of III-V inorganic semiconductor nanowires and nanowire heterostructures. Two applications are considered: nanowires as active elements within solar cells, and nanowires as the host for single photon emitters. These were studied using a combination of theoretical and experimental techniques. The efficiency limits of the nanowire-planar tandem solar cell were first determined using a detailed balance-based approach, to provide design guidelines for the experimental realisation of such a device. The catalyst-free growth of GaAs and InP nanowires was then developed, with the nanowires containing quantum dot heterostructures. These structures are of great interest for the creation of position controlled single photon sources, with potential for use in quantum information applications, for instance by utilising the emission of entangled photons¹³.

1.1 Background

In the following sections, the concept of reduced dimensionality in semiconductor materials is introduced, which naturally leads to a discussion of nanowire and quantum dot structures.

1.1.1 Low dimensional semiconductors

The properties of semiconductors can be significantly modified by reducing the physical extent of at least one of the dimensions to the order of the exciton Bohr radius. The Bohr radius depends on the relative permittivity and carrier reduced mass of the semiconductor. This thesis focuses on GaAs and InP, for which the exciton Bohr radius is $\sim 13\text{nm}$ and $\sim 12\text{nm}$ respectively¹⁴. In this regime, quantized charge carrier energy levels manifest as a result of quantum confinement. This allows for a much greater range of functionality through the ability to leverage physical phenomena in the quantum rather than classical regime. A semiconductor confined in one dimension is termed a quantum well (QW) and described as a two-dimensional (2D) system, where the number refers to the dimensions in which the exciton may freely propagate. Reducing the dimensionality further results in 1D quantum wires which, amongst other effects, exhibit quantized conductance. Finally, further reduction of the dimensions leads to a 0D system known as a quantum dot (QD). An ideal QD is capable of emitting single photons, as discussed later.

The influence of reduced dimensionality can be visualized clearly in the density of states (DOS) for electrons in the semiconductor. This is shown in Figure 1.1 alongside the energy-momentum (E-k) dispersion for carriers in the conduction band for the bulk and 2D cases. In a bulk semiconductor the E-k dispersion for electrons is

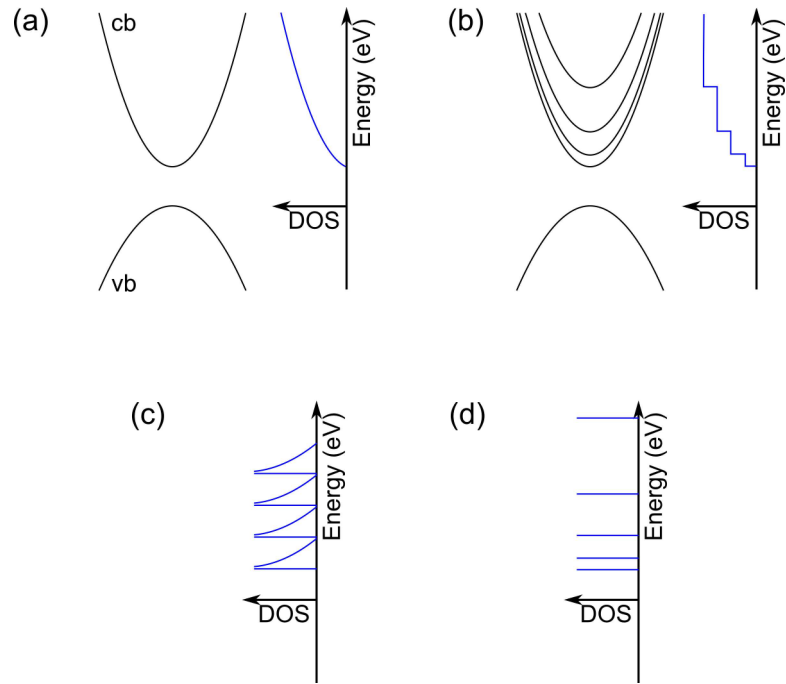


Figure 1.1. Density of conduction band states for semiconductors of reduced dimensionality. (Left) E-k relationship for a direct bandgap semiconductor, (right) associated DOS for the conduction band for the case of (a) bulk semiconductor and (b) quantum well. cb – conduction band, vb – valence band; DOS for electrons in a (c) quantum wire and (d) quantum dot.

approximately parabolic about the minimum separation between the valence band maximum and the conduction band minimum (the Brillouin zone Γ -point for a direct bandgap material like GaAs). Above the bandgap energy the E-k dispersion forms a continuous conduction band containing $2N$ possible states, where N is the number of atoms forming the semiconductor and the prefactor accounts for the electron spin. Upon reducing the physical extent of a single dimension so that it is comparable to the exciton Bohr radius, electrons are confined in that dimension. This leads to the formation of discrete energy levels in the confined dimension, whilst the parabolic dispersion in the unconfined dimensions is unaffected. The result is the well-known ladder observed in the

DOS for a QW (Figure 1.1(b)). In the case of a 1D quantum wire the DOS becomes much more discrete, with a residual tail indicating the influence of exciton propagation in the unconfined dimension. Finally, a 0D QD exhibits a purely discrete DOS function.

The transition from the classical bulk semiconductor to the quantized regime is not abrupt, and the change in the dispersion relations and DOS reflect this. Two regimes can be considered in this regard, those of weak and strong confinement. In the former, relatively weak quantization effects are observed despite the exciton Bohr radius being less than the minimum size of the semiconductor. Quantization effects can be observed so long as the energy spacing between quantized energy states is larger than the thermal energy of charge carriers, $k_B T$, where k_B is the Boltzmann constant. This corresponds to $\sim 0.34 \text{ meV}$ at $T=4\text{K}$. The strong confinement regime concerns the opposite case, where the exciton Bohr radius is larger than the minimum size of the semiconductor. This can be seen in the dispersion relation for a QW (Figure 1.2) in which the separation of the energy bands increases during the transition from the weak to strong confinement regimes.

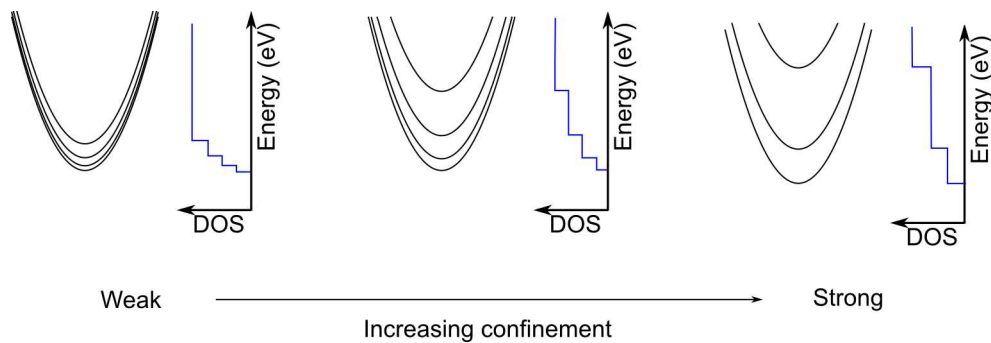


Figure 1.2. Transition from weak to strong confinement in a semiconductor. (Left to right) A small perturbation of the bulk conduction band in the presence of weak confinement becomes more significant with increasing carrier confinement, leading to well-spaced energy levels in the strong confinement regime.

In the following sections, an introduction to semiconductor nanowires and quantum dots is presented. The unique crystal structure observed following the bottom-up growth of nanowires is discussed, and the appeal of nanowires for photovoltaic applications is described.

1.1.2 Semiconductor nanowires

Semiconductor nanowires are columnar nanostructures with a radial dimension of the order of nanometres and an unconstrained length, typically 1-10 microns. They often have a hexagonal cross-section when grown in a bottom-up process, reflecting the crystal structure of the nanowire, although other geometries have been observed¹⁵. A representative scanning electron microscope image of a GaAs nanowire is shown in Figure 1.3. It should be recognized that the nanowire diameter is not necessarily small enough to reach the strongly confined 1D quantum regime. Indeed, for nanowires with diameter much larger than 100nm the nanowire structure may influence optical and electrical properties through surface and waveguiding effects rather than quantum

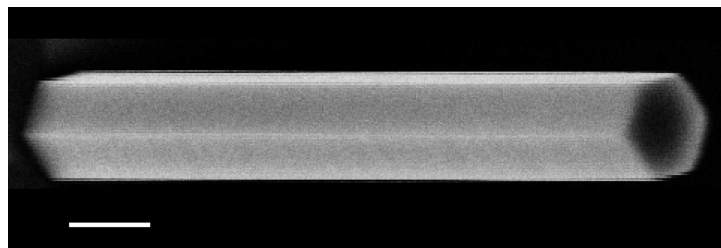


Figure 1.3. Scanning electron microscope image of a GaAs nanowire. Scale bar 200nm.

confinement. Waveguiding is of particular interest for photovoltaic applications. In this work, the term nanowire is used to describe any columnar structure with a diameter between 1nm and 1 μ m. Structures larger than 1 μ m in diameter are frequently referred to as microwires within the literature.

Semiconductor nanowires may be fabricated using either top-down or bottom-up approaches. The former commonly relies on anisotropic etching techniques, whereas the latter is generally an epitaxial growth technique (growth on non-crystalline substrates has also been demonstrated however^{16,17}). Bottom-up growth is of interest here, for it gives great scope in tuning of the nanowire characteristics, for instance through radial growth procedures which are not possible using a purely top-down approach. Bottom-up growth also develops epitaxial quality surfaces unlike etching process which may produce damaged facets, impairing the optical performance of the structures¹⁸.

The earliest semiconductor nanowire growth was observed to be mediated by metal impurities on a crystalline substrate¹⁹. This was soon followed by a description of the growth process, which became known as the vapour-liquid-solid growth technique²⁰. It is also possible to obtain nanowires in some cases if the growth conditions are chosen incorrectly during planar epitaxy, particularly in the case of growth on substrates other than the conventional (100) orientation. This is a demonstration of facet led growth, whereby variable growth rates lead to the preferential incorporation of adatoms on, and development of, specific crystal facets. Facet led growth was first combined with selective dielectric masking of planar substrates to force growth at specific locations, leading to the formation of in-plane nanowires^{21,22}. Further refinement of this approach then allowed the realisation of vertical nanowire structures²³. This selective area, catalyst-free approach to nanowire growth is the second most common of the bottom-up growth

techniques after the VLS approach. In the experimental work reported in Chapters 3-6, catalyst-free growth was utilised. This was motivated by the prevention of impurities which may be transferred from the catalyst during VLS growth. There is also the potential to obtain higher quality heterointerfaces utilising the catalyst-free growth mode. This choice is discussed in more detail in Chapter 3.

1.1.3 Nanowire crystal structure

The nanowires grown during the course of this research were formed from GaAs and InP, and grew vertically on (111)B and (111)A orientated substrates respectively. When grown in bulk, the crystal structure of both these semiconductors takes the zinc blende form. The zinc blende crystal comprises two interpenetrating face-centred cubic crystals, as shown in Figure 1.4(a) and Figure 1.4(b). For GaAs nanowires grown the by catalyst-free technique the crystal structure is typically that of bulk GaAs. However, studies of InP

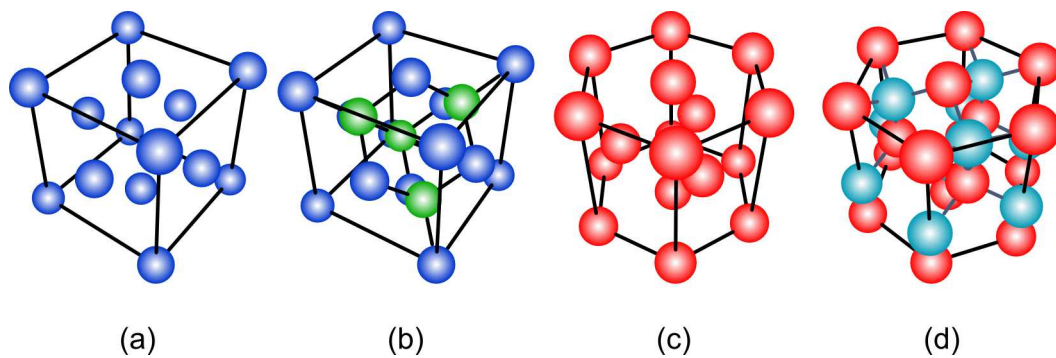


Figure 1.4. Schematics of crystal structures observed in nanowires. (a) The face centred cubic (FCC) crystal structure; (b) Two interpenetrating FCC lattices forming the zinc blende structure. Here, blue (green) atoms represent gallium (arsenic) forming zinc blende GaAs; (c) The hexagonal close packed (HCP) crystal structure; (d) Two interpenetrating HCP crystals forming the wurtzite structure. Here, red (light blue) atoms represent indium (phosphorus) forming wurtzite InP.

nanowires grown in the same way have shown these often develop with the wurtzite crystal structure²⁴. This is formed from two hexagonal close packed crystals, shown in Figure 1.4(c) and Figure 1.4(d).

The GaAs nanowires studied in this work contained twinning planes, where a single crystal phase rotated 180° about the growth axis. These are commonly observed in zinc blende GaAs nanowires grown by the catalyst-free technique^{25,26} and are visible in transmission electron microscope imaging due to the difference in electron diffraction conditions on either side of the twin plane. A zinc blende twin plane may be viewed as a monolayer of wurtzite crystal structure²⁷. This can be seen in Figure 1.5(a). Consecutive formation of twin planes in a zinc blende nanowire effectively forms a region of wurtzite nanowire. As zinc blende and wurtzite GaAs have different bandgaps and electron affinities, there is a discontinuous band alignment at the interface between the two crystal

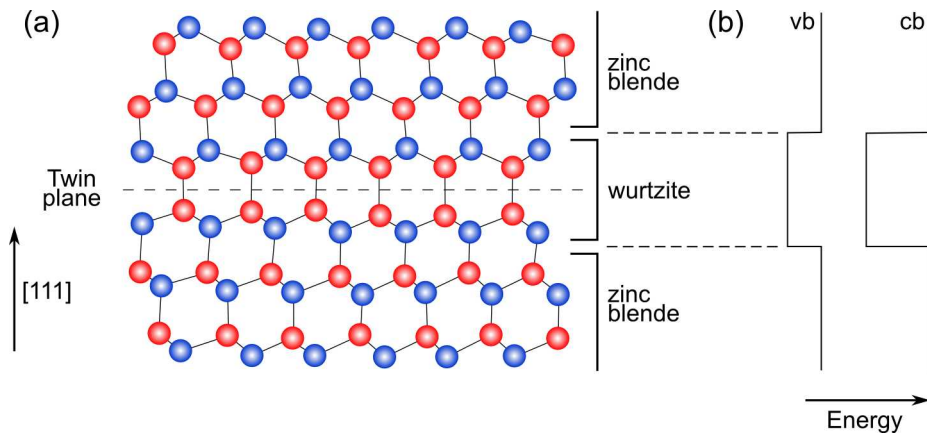


Figure 1.5. Schematic showing twin plane formation in a zinc blende nanowire. (a) Rotation of the crystal through 180° produces an effective monolayer of wurtzite crystal structure. Red and blue circles denote the two different atomic species forming the crystal (e.g. gallium and arsenic in GaAs); (b) Conduction and valence band alignment across the twin plane. cb – conduction band, vb – valence band.

phases. This is shown in Figure 1.5(b). The discontinuity influences the optical properties of the nanowire, for instance by acting to localize charge carriers. The occurrence of twin planes is in general significant in the case of growth in the (111)B direction and is consequently an important issue to be contended with when fabricating nanowire devices. To date the elimination of twinning planes from GaAs nanowires grown in the (111)B direction by the catalyst-free technique has not been reported.

The structure of InP nanowires grown by the catalyst-free technique is generally different to that of GaAs. InP nanowires commonly contain wurtzite sections, and often alternate between zinc blende and wurtzite structure along the growth axis²⁸. The resulting nanowires are known as polytypic. Polytypism is accompanied by a stacking fault perpendicular to the nanowire growth axis between the wurtzite and zinc blende crystal phases. As for GaAs, the zinc blende and wurtzite crystal phases of InP have different bandgaps and electron affinities, resulting in discontinuous band alignment in polytypic nanowires. This has a significant impact on the optoelectronic properties of the nanowires. For instance, photoluminescence from such a nanowire shows a broad range of emission energies, reflecting radiative recombination not only within a single crystal phase but also between the two different phases. This is discussed in more detail in Chapter 6.

1.1.4 Semiconductor nanowires for photovoltaics

Solar energy conversion has the potential to provide a significant fraction of the world's energy demand²⁹. Conversion of solar photons to electricity is particularly appealing due to the practical utility of electricity. This can be achieved using a semiconductor photovoltaic device (solar cell). The presence of a bandgap in semiconductor materials

provides a route for the absorption of photons and the formation of an electron-hole pair. The ability to create an inbuilt electric field using p-type and n-type doping of the semiconductor allows for the consequent separation and extraction of charge carriers, generating a current at non-zero voltage. Semiconductors such as silicon, InP and GaAs have bandgaps which are almost ideally matched to the solar spectrum for the formation of single junction solar cells.

Commercially, terrestrial electricity generation using photovoltaics is dominated by silicon technology. This is due in part to the abundance of silicon, and furthermore to the advances made in silicon technology for classical computing which led to the development of ultrahigh purity silicon. However, a single junction solar cell formed from silicon has a limited efficiency due to multiple loss processes, in particular the thermalisation of high energy carriers to the bottom (top) of the conduction (valence) bands. This limits a single junction device to an efficiency of $\sim 33\%$ ³⁰. A common technique to overcome this particular loss process is to combine several different semiconductors in the same solar cell. Correct choice of the semiconductor bandgaps results in a net absorption (after thermalisation) that is significantly higher than that for a single junction solar cell. Such devices typically utilise more expensive tertiary III-V semiconductors such as InGaAs, and are limited to lattice matched alloys. Multijunction (tandem) solar cells are thus limited at present to those applications for which price is relatively unimportant, for instance in satellites.

Semiconductor nanowires have several properties which make them prospective candidates to form high efficiency photovoltaic devices. The sub-wavelength columnar structure of a nanowire results in waveguide effects which may efficiently trap light, thus allowing for strong light absorption in a relatively small material volume. This reduces

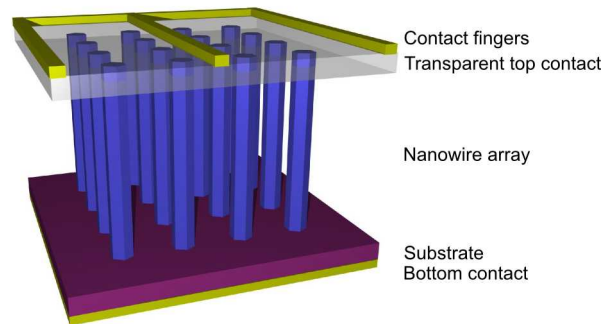


Figure 1.6. Schematic of the nanowire-planar tandem solar cell modelled in Chapter 2.

the material demand for each solar cell. Furthermore, nanowires may be grown with much greater lattice mismatch than is possible for planar epitaxy. This is due to efficient strain relaxation at the nanowire surface³¹ and allows a greater combination of materials to be used in the same device, ultimately providing a route for high efficiency multijunction photovoltaics. The modelling of a nanowire-planar tandem solar cell (Figure 1.6) is the subject of Chapter 2.

1.1.5 Semiconductor quantum dots

A QD is a nanoscale volume of semiconductor whose dimensions lead to three dimensional carrier confinement. Confinement imposes discrete energy levels on carriers in the QD, which manifest in its physical properties. As an example, an ideal zero dimensional QD emits photons at discrete energies. This has led to a popular description of the QD as an ‘artificial atom’. An important result of carrier confinement is the potential for emission of single photons from the QD. This non-classical state of light is evidence of the quantum nature of energy states within the QD, and has potential benefit

for future quantum information applications. For instance, the emission of single photons may be utilised in long distance quantum cryptography⁵. In the following sections, the growth of QDs is first described. The energy levels for carriers within the QD are then discussed, and the mechanism for single photon emission is explained. Finally, the limits of SK growth and ways to overcome these are briefly discussed.

1.1.5.1 Semiconductor quantum dot growth

Many different techniques have been used to form QD structures in inorganic semiconductors, including epitaxial growth³², electrostatic definition³³ and etching of quantum well structures¹⁸. Electrostatic definition relies on the formation of an electrostatic confinement potential across a small region of a quantum well by patterning and electrically contacting metal gates on the surface of the sample. The resulting QD is usually only weakly confined. Etching of quantum wells to form QDs may generate damaged facets which impair the optical performance of the QD, exacerbated by the proximity of the QD to the surface. Here, bottom-up epitaxial growth techniques are considered which are commonly used to obtain well-confined QDs exhibiting high quality optical properties.

Epitaxial growth of an inorganic semiconductor QD involves embedding a small volume of one semiconductor in a matrix formed from a semiconductor with a larger bandgap. QDs may be grown through a process known as self-assembly using for instance metal organic chemical vapour deposition (MOCVD) or molecular beam epitaxy (MBE). A common QD growth mechanism is the Stranski-Krastanow (SK) technique. This involves the epitaxial growth of a semiconductor (A) on a lattice mismatched substrate (B). Below the critical thickness for strain relaxation, a thin planar layer of A forms on B . This is



Figure 1.7. Schematic illustrating the Stranski-Krastanow growth process. (a) Planar growth substrate (formed from material A in the main text); (b) a strained, lattice mismatched layer is deposited epitaxially onto the substrate (material B in main text); (c) after further deposition of the lattice mismatched material, strain is relieved through formation of islands on the surface – these form QDs; (d) the QDs are capped, resulting in a planarised surface.

known as the wetting layer. Upon further growth of A , the strain which builds up due to the lattice mismatch may be relieved by the formation of islands (QDs). The SK technique is therefore only able to produce strained QDs. The QDs are capped by continuing growth with the same semiconductor as the underlying substrate (B). This removes unsatisfied dangling bonds at the surface of the QD, which may act as non-radiative recombination centres and thus impair the optoelectronic properties of the QD. The SK growth procedure is described schematically in Figure 1.7. QDs formed using the SK technique are typically asymmetric, with a diameter of a few tens of nanometres, and a height of a few nanometres.

1.1.5.2 Energy states and optical properties of quantum dots

Optically-active QDs are formed within direct bandgap semiconductors in order to maximise transition oscillator strengths, increasing for instance the photon emission rate. Figure 1.8 shows schematics of the band edge transitions for bulk semiconductors for the case of a direct and indirect bandgap semiconductor. In a direct bandgap semiconductor the transition requires little change in momentum and is mediated by the emission or

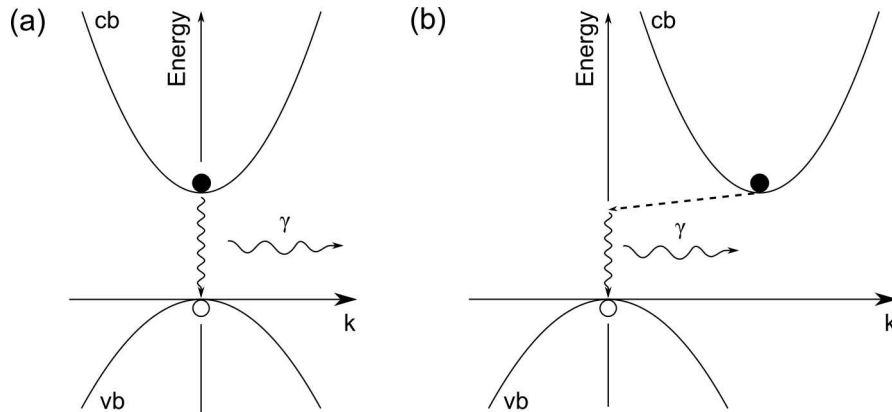


Figure 1.8. Band diagram showing direct and indirect interband transitions in bulk semiconductors. (a) Band edge recombination in a direct bandgap semiconductor; (b) Indirect, phonon assisted recombination in an indirect bandgap semiconductor. Dashed line denotes phonon emission. cb – conduction band, vb – valence band, k – momentum, γ – photon emission. Full (empty) circles correspond to electrons (holes).

absorption of a single photon. In contrast, for an indirect bandgap semiconductor such as GaP or Si the valence band maximum / conduction band minimum occur for different values of the crystal momentum. The transition between the two bands therefore requires either absorption or emission of a phonon, and is consequently much weaker than a direct transition. The direct transition is therefore more appealing for the formation of optically active QDs.

The form of the confinement potential in a QD is dependent on the choice of semiconductors for both the QD and the surrounding matrix, as well as the physical dimensions of the QD. Two energy band configurations are possible for self-assembled QDs, categorised as type-I and type-II band alignment. These are described schematically in Figure 1.9. In a QD exhibiting type-I confinement, the valence band of the QD is at higher energy than that of the surrounding semiconductor, whilst the opposite is true for

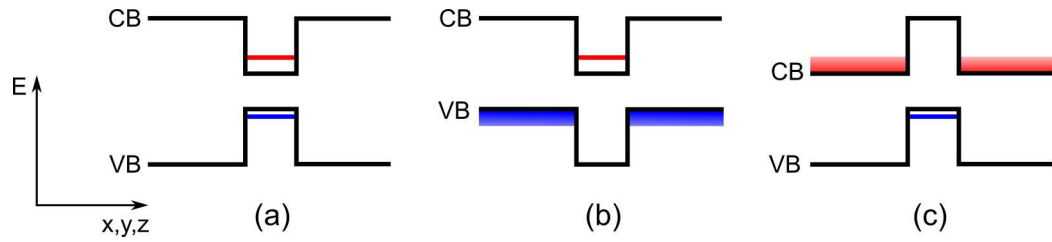


Figure 1.9. Schematic representation of energy band alignment in (a) type-I and (b), (c) type-II quantum dots. The central region of each configuration forms the quantum dot. Red (blue) lines mark electron (hole) lowest energy confined states. Red (blue) shaded regions denote continua of electron (hole) energy states. The vertical axis represents energy, the horizontal axis three orthogonal spatial directions. (a) Both holes and electrons are confined within the lower bandgap quantum dot; (b) Electrons are confined within the quantum dot but holes are not; (c) Holes are confined to the quantum dot but electrons are not.

the conduction band. This results in both holes and electrons being confined to the QD. In type-II QDs, either the valence band is at lower energy than that of the surrounding semiconductor, or the conduction band of the QD is at higher energy than that of the surrounding semiconductor. In both cases the other band lies energetically as in a type-I QD. In the former case this leads to only electrons being confined in the QD, whilst in the latter case only holes are confined to the QD.

Due to the radial / axial asymmetry of an SK QD, the separation of the lowest energy states is determined by the weaker radial confinement. This is often approximated as a circularly symmetric harmonic function for the lens-shaped QDs formed by SK growth³⁴. The discrete energy states are therefore separated equally in energy, as for the harmonic oscillator. The Pauli Exclusion Principle provides limits on the occupation of the energy states. The ground state can hold two electrons with opposite spin, whilst higher order states are filled with electrons of increasing angular momentum. This is shown

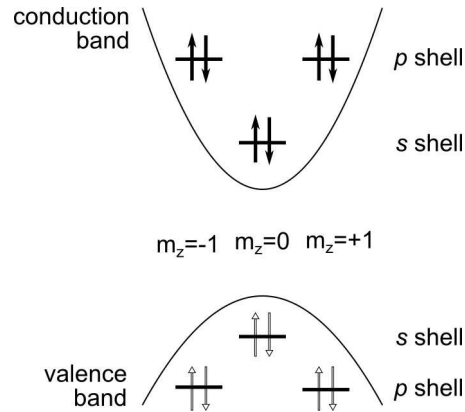


Figure 1.10. Electron and hole energy states within a QD. The energy levels are shown for the z -resolved angular momentum $m_z = -1, 0, +1$. The levels are labelled with the $s, p, d...$ notation for angular momentum from atomic physics. Full (empty) arrows correspond to electrons (holes) – arrows pointing up (down) denote the spin orientation. Curves provide a reminder of the parabolic band potentials.

schematically in Figure 1.10. The confining potential provided by the QD ensures that the lowest energy electron and hole are bound to form an exciton. The strain inherent to this type of QD lifts the degeneracy of the heavy and light hole valence bands, meaning that to a first approximation the QD states have heavy hole character, although mixing of the light and heavy holes may occur³⁵.

In the absence of such mixing, the total angular momentum of the exciton is given by the sum of the angular momentum for the single particle electron and hole states. Taking the QD to lie in the x - y plane, such that the harmonic potential lies in that plane also, the total angular momentum can be projected into the z direction (growth direction)³⁶. The conduction band s -shell electrons then have a projected spin of $\pm 1/2$ in units of the reduced Planck constant \hbar . The heavy s -shell holes have total projected angular momentum $\pm 3/2$. The total angular momentum is therefore $+2, +1, -1$ or -2 corresponding

to four possible exciton states. The ± 1 states may recombine and emit a photon, whilst for the ± 2 states this is forbidden by conservation of momentum. States with spin ± 1 are therefore termed bright excitons and are observed in photoluminescence from an excited QD. States with angular momentum of ± 2 form the so-called dark exciton states.

Experimentally, other effects must be taken into account when accounting for the energy levels of a QD. Asymmetry in the x-y confinement leads to a fine structure splitting which lifts the degeneracy of the bright excitons. This is discussed in Chapter 4. Adding a single charge carrier to a QD perturbs the energy levels of the QD. A simple example involves the exciton and biexciton states of a neutral QD. A biexciton is formed when two confined excitons interact in a type-I QD. A renormalization energy is required to describe the interaction, known as the biexciton binding energy. This shifts the energy of the biexciton transition relative to the exciton, the magnitude and sign of the shift being dependent on the size of the QD. In general the binding energy is predicted to be positive and increase with decreasing QD dimensions, due to exchange interactions between the four carriers. However, reducing the dimensions of the QD further may lead to Coulomb repulsion and a negative binding energy³⁷. Further additions to the photoluminescence spectra arise due to charging of the QD, for instance forming charged positive or negative trion states. A QD may thus exhibit much richer optical properties than simple models suggest.

As mentioned previously, an important property of QDs is their ability to emit single photons. This is a result of the discrete energy states of the QD. Consider a QD which is excited with a continuous wave laser, such that at most only the ground state is populated. Due to the Pauli Exclusion Principle only two excitons may reside in the QD at the same time, and a non-zero biexciton energy means that only one electron-hole pair will be

formed at the exciton energy. Therefore, only a single photon can be emitted at the exciton energy at a single point in time. The exciton state must then be repopulated before radiative recombination can produce another photon at the exciton energy. The photons emitted at the exciton energy are therefore spaced more equally in time than is possible for even a perfectly coherent classical light source. Single photon generation in this manner produces light characterised by sub-Poissonian statistics, demonstrating the quantum nature of light. The standard measurement technique used to demonstrate single photon emission from a QD is discussed in Chapter 4.

1.1.5.3 Improving upon standard quantum dot growth techniques

There are some significant drawbacks to the standard mechanisms for QD epitaxy which have motivated research into alternative approaches for QD formation. Two such challenges involve the random location and size dispersion of the QDs grown by these techniques. This has ramifications for the scale up required for some future applications, including integration with photonic crystals. Position-controlled epitaxy of QDs has therefore been the subject of significant research efforts in the last decade. With regards to growth in the plane of the substrate, the most impressive work to date has concerned the growth of QDs within pyramidal pits etched into (111)B GaAs substrates³⁸. Extremely low ensemble broadening for excitonic photon emission of $\sim 1\text{meV}$ has been achieved in this manner.

In this work, an alternative technique for position control was investigated. QDs were formed within individual nanowires, leveraging the lithographic definition inherent to the selective area growth of nanowires to ensure position control of the QDs. The nanowire diameter was also controlled, which naturally controlled the diameter of the QD.

Particular advantages of the nanowire geometry for QD growth include the potential to realise multiple, optically coupled QDs in the same nanowire, and the enhancement of photon count rates as the waveguide geometry efficiently couples light into external optics. The layer by layer nature of nanowire growth means that strain is not a prerequisite for nanowire QD realisation. The growth of QDs in the [111] directions preferred by GaAs and InP nanowires has also been shown to reduce the fine structure splitting which is of particular interest for the emission of entangled photons¹³.

1.2 Summary of chapters

In Chapter 2, a model is developed to determine the radiative efficiency limits of the nanowire-planar tandem solar cell and to provide design guidelines for the fabrication of such a solar cell. Chapter 3 discusses the extensive efforts undertaken to produce GaAs nanowires by the catalyst-free growth technique, which is expanded in Chapter 4 to include InGaAs QDs embedded within the nanowires. In Chapter 5 a new means to control the nanowire morphology using the catalyst-free growth technique is presented, leading to elongated cross-section nanowires emitting linearly polarized light from the top facet. Finally in Chapter 6 efforts to develop the catalyst-free growth of InP nanowires containing InAsP QDs are discussed, with the prospect for superior single photon emission relative to the InGaAs material system.

Bibliography

- (1) Wallentin, J.; Anttu, N.; Asoli, D.; Huffman, M.; Aberg, I.; Magnusson, M. H.; Siefert, G.; Fuss-Kailuweit, P.; Dimroth, F.; Witzigmann, B.; Xu, H. Q.; Samuelson, L.; Deppert, K.; Borgström, M. T. *Science*. **2013**, *339*, 1057–60.
- (2) Kupec, J.; Stoop, R. L.; Witzigmann, B. *Opt. Express* **2010**, *18*, 27589–27605.
- (3) Dorenbos, S. N.; Sasakura, H.; van Kouwen, M. P.; Akopian, N.; Adachi, S.; Namekata, N.; Jo, M.; Motohisa, J.; Kobayashi, Y.; Tomioka, K.; Fukui, T.; Inoue, S.; Kumano, H.; Natarajan, C. M.; Hadfield, R. H.; Zijlstra, T.; Klapwijk, T. M.; Zwiller, V.; Suemune, I. *Appl. Phys. Lett.* **2010**, *97*, 171106.
- (4) Dalacu, D.; Mnaymneh, K.; Lapointe, J.; Wu, X.; Poole, P. J.; Bulgarini, G.; Zwiller, V.; Reimer, M. E. *Nano Lett.* **2012**, *12*, 5919–23.
- (5) Shields, A. J. *Nat. Photonics* **2007**, *1*, 215–233.
- (6) Kim, H.-M.; Cho, Y.-H.; Lee, H.; Kim, S. Il; Ryu, S. R.; Kim, D. Y.; Kang, T. W.; Chung, K. S. *Nano Lett.* **2004**, *4*, 1059–1062.
- (7) Ramos, D.; Gil-Santos, E.; Pini, V.; Llorens, J. M.; Fernández-Regúlez, M.; San Paulo, Á.; Calleja, M.; Tamayo, J. *Nano Lett.* **2012**, *12*, 932–7.
- (8) Arcizet, O.; Jacques, V.; Siria, a.; Poncharal, P.; Vincent, P.; Seidelin, S. *Nat. Phys.* **2011**, *7*, 879–883.
- (9) Mourik, V.; Zuo, K.; Frolov, S. M.; Plissard, S. R.; Bakkers, E. P. A. M.; Kouwenhoven, L. P. *Science*. **2012**, *336*, 1003–1007.
- (10) Plissard, S. R.; van Weperen, I.; Car, D.; Verheijen, M. a; Immink, G. W. G.; Kammhuber, J.; Cornelissen, L. J.; Szombati, D. B.; Geresdi, A.; Frolov, S. M.; Kouwenhoven, L. P.; Bakkers, E. P. a M. *Nat. Nanotechnol.* **2013**, 1–6.
- (11) Cui, Y.; Wei, Q.; Park, H.; Lieber, C. M. *Science* **2001**, *293*, 1289–92.
- (12) Tomioka, K.; Yoshimura, M.; Fukui, T. *Nature* **2012**, *488*, 189–193.
- (13) Singh, R.; Bester, G. *Phys. Rev. Lett.* **2009**, *103*, 063601.

-
- (14) Fox, M. *Optical Properties of Solids*; Second edi.; Oxford University Press: Oxford.
- (15) Kim, S.-K.; Day, R. W.; Cahoon, J. F.; Kempa, T. J.; Song, K.-D.; Park, H.-G.; Lieber, C. M. *Nano Lett.* **2012**, *12*, 4971–6.
- (16) Tsakalakos, L.; Balch, J.; Fronheiser, J.; Korevaar, B. A.; Sulima, O.; Rand, J. *Appl. Phys. Lett.* **2007**, *91*, 233117.
- (17) Han, N.; Wang, F.; Hui, A. T.; Hou, J. J.; Shan, G.; Xiu, F.; Hung, T.; Ho, J. C. *Nanotechnology* **2011**, *22*, 285607.
- (18) Clausen, E. M.; Craighead, H. G.; Worlock, J. M.; Harbison, J. P.; Schiavone, L. M.; Florez, L.; Van der Gaag, B. *Appl. Phys. Lett.* **1989**, *55*, 1427.
- (19) Wagner, R. S.; Ellis, W. C.; Jackson, K. a.; Arnold, S. M. *J. Appl. Phys.* **1964**, *35*, 2993.
- (20) Wagner, R. S.; Ellis, W. C. *Appl. Phys. Lett.* **1964**, *4*, 89.
- (21) Nakajima, F.; Ogasawara, Y.; Motohisa, J.; Fukui, T. *J. Appl. Phys.* **2001**, *90*, 2606.
- (22) Takahashi, H.; Miyoshi, Y.; Nakajima, F.; Mohan, P.; Motohisa, J.; Fukui, T. *Appl. Surf. Sci.* **2003**, *216*, 402–406.
- (23) Motohisa, J.; Takeda, J.; Inari, M.; Noborisaka, J.; Fukui, T. *Phys. E* **2004**, *23*, 298–304.
- (24) Mohan, P.; Motohisa, J.; Fukui, T. *Nanotechnology* **2005**, *16*, 2903–2907.
- (25) Ikejiri, K.; Sato, T.; Yoshida, H.; Hiruma, K.; Motohisa, J.; Hara, S.; Fukui, T. *Nanotechnology* **2008**, *19*, 265604.
- (26) Motohisa, J.; Noborisaka, J.; Takeda, J.; Inari, M.; Fukui, T. *J. Cryst. Growth* **2004**, *272*, 180–185.
- (27) Hiruma, K.; Yazawa, M.; Katsuyama, T.; Ogawa, K.; Haraguchi, K.; Koguchi, M.; Kakibayashi, H. *J. Appl. Phys.* **1995**, *77*, 447.

-
- (28) Kitauchi, Y.; Kobayashi, Y.; Tomioka, K.; Hara, S.; Hiruma, K.; Fukui, T.; Motohisa, J. *Nano Lett.* **2010**, *10*, 1699–703.
- (29) Lewis, N. S. *Science* **2007**, *315*, 798–801.
- (30) Marti, A.; Araujo, G. L. *Sol. Energy Mater. Sol. Cells* **1996**, *43*, 203–222.
- (31) Kavanagh, K. L. *Semicond. Sci. Technol.* **2010**, *25*, 024006.
- (32) Marzin, J.-Y.; Gerard, J.-M.; Izrael, A.; Barrier, D.; Bastard, G. *Phys. Rev. Lett.* **1994**, *73*, 1–4.
- (33) Kouwenhoven, L. P.; Johnson, A. T.; van der Vaart, N. C.; Harmans, C. J. P. M.; Foxon, C. T. *Phys. Rev. Lett.* **1991**, *67*, 1626–1629.
- (34) Michler, P. *Single quantum dots. Fundamentals, Applications and New Concepts*, vol 90 of *Topics in Applied Physics*; Springer, 2003.
- (35) Plumhof, J. D.; Trotta, R.; Křápek, V.; Zallo, E.; Atkinson, P.; Kumar, S.; Rastelli, A.; Schmidt, O. G. *Phys. Rev. B* **2013**, *87*, 075311.
- (36) Johansen, J.; Julsgaard, B.; Stobbe, S.; Hvam, J. M.; Lodahl, P. *Phys. Rev. B* **2010**, *81*, 081304.
- (37) Rodt, S.; Heitz, R.; Schliwa, A.; Sellin, R.; Guffarth, F.; Bimberg, D. *Phys. Rev. B* **2003**, *68*, 035331.
- (38) Mohan, A.; Gallo, P.; Felici, M.; Dwir, B.; Rudra, A.; Faist, J.; Kapon, E. *Small* **2010**, *6*, 1268–72.

2 Design considerations for nanowire-planar tandem solar cells

2.1 Introduction

In the last few years there has been increasing interest in the utilisation of nanowire arrays within solar cells, either as antireflection coatings¹⁻³ or optically and electronically active components⁴⁻⁹. There are multiple incentives for the application of such structures to photovoltaic devices. An array of nanowires may be designed such that reflection of a plane wave incident on the end facets of the nanowires is significantly reduced relative to that from a planar interface. Whilst clearly of benefit for antireflection applications, minimised reflection is often accompanied by minimised transmission through the array i.e. the array can be designed to efficiently absorb light. Indeed, the absorption coefficient of an array of nanowires may be significantly greater than that of the equivalent planar film¹⁰. The volume of semiconductor material required is therefore smaller, reducing costs. With cost in mind, the nanowire growth rate is typically much greater than the equivalent rate for planar epitaxy, allowing greater throughput in a commercial setting. Furthermore, nanowires may be grown heterogeneously with lattice mismatch much greater than is possible for planar epitaxy, allowing consideration of a greater range of materials combinations¹¹. An interesting extension of this concept is growth on cheap substrates such as glass and metal foil^{4,5} or substrate reuse following removal of the

nanowires embedded in a polymer support film¹². Finally, the ability to form a radial p-n junction is almost unique to the nanowire morphology, and allows orthogonal separation of light absorption and carrier extraction from a nanowire. In so doing the distance from excitation location to the electrical contact is minimised resulting in the reduction of carrier recombination losses¹³. This is particularly appealing when cheaper, more defective materials are used within the solar cell.

In this chapter the theoretical efficiency limits of nanowire solar cells are investigated. In section 2.2 the theoretical basis for the inclusion of nanowire arrays in solar cells is discussed in more detail. Section 2.3 reviews the current state of the art of nanowire solar cells. In section 2.4 an optical model is developed to evaluate the efficiency limits of a solar cell formed from an optoelectronically active nanowire array grown on top of an active planar substrate. This is required as few papers have considered this application in depth to date. The model provides an estimate of the maximum theoretical efficiency of such a solar cell, leading to overarching design guidelines for the experimental realisation of the solar cell in contrast to focussing on individual structures.

2.2 Benefits of nanowire arrays for solar cell applications

2.2.1 Antireflection and enhanced absorption properties of a nanowire array

Arrays of nanowires with individual diameters on the order of several hundred nanometres are particularly appealing for use as the absorbing elements of solar cells due

to enhanced coupling of incident radiation into the structure. For the nanowire diameter and pitches commonly used in solar cell designs within the literature, the optical properties of the structure cannot be described by the Maxwell-Garnett effective medium approximation¹⁴, but are instead dominated by the optical modes supported by the array.

Given the correct choice of nanowire diameter and pitch (the separation between nanowires), a plane wave normally incident on the top facets of a square nanowire array may be coupled to one of two ‘key’ modes which play a large role in governing the optical response of the system¹⁰. Coupling of the incident plane wave is greatest when the modal effective index is closest to 1 (i.e. a wave in free space), and the overlap of the electric fields of the mode and the incident wave is maximised. The two ‘key’ modes satisfy these criteria in different wavelength ranges, with the net result that the full wavelength range of interest is accounted for. The wavelength range is limited at low energy by the nanowire bandgap (typically of the order of 1eV) and at high energy by the properties of the solar spectrum, which contains negligible power for wavelengths shorter than ~300nm (~4.14eV).

To demonstrate the efficient absorption properties of nanowire arrays, the results of finite-difference time-domain (FDTD) simulations are presented Figure 2.1. First, an infinite periodic square array of InP nanowires with a height of 2 μm , diameter $d=180\text{nm}$ and pitch $p=360\text{nm}$ was modelled. The dimensions have been reported elsewhere to achieve close to maximal absorption¹⁰ and correspond to a packing fraction of 0.196 ($=\pi d^2/4p^2$). The simulation was undertaken in the absence of a substrate to access the properties of the nanowire array only, whilst the space between nanowires had a refractive index of unity. A schematic of the array is shown in Figure 2.1(a) whilst the simulation domain is shown in Figure 2.1(b). A plane wave generated by a current source

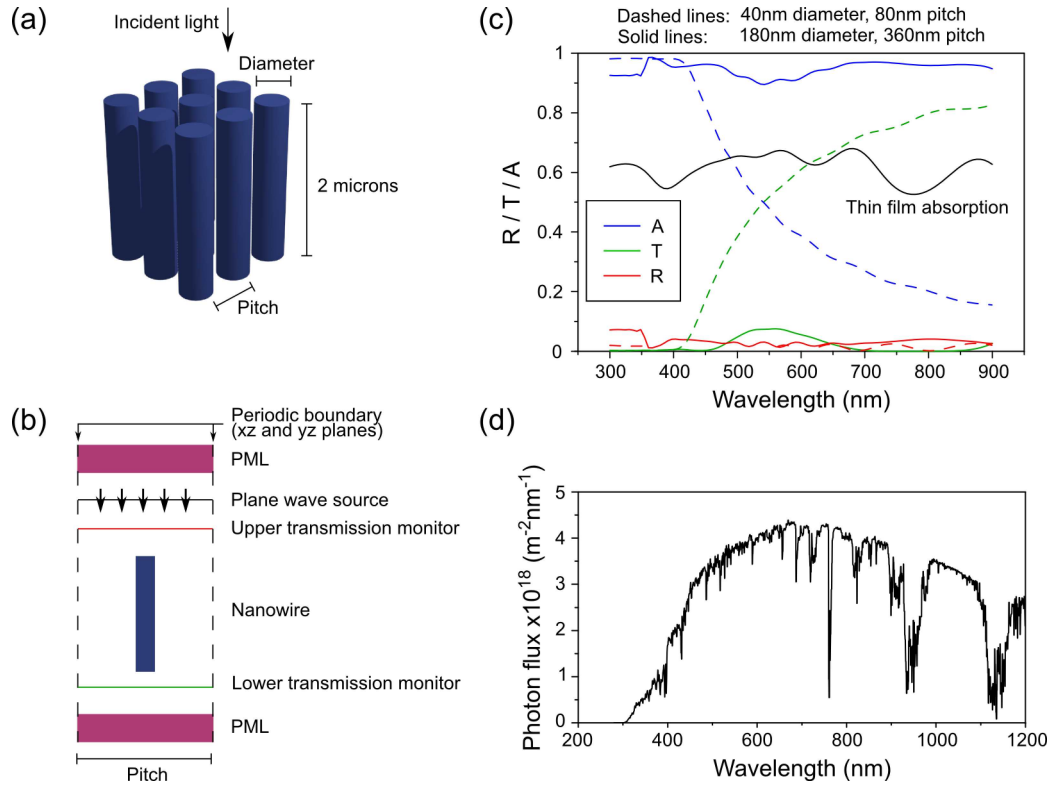


Figure 2.1. Antireflection and enhanced absorption by a nanowire array. (a) Schematic overview of a square nanowire array with definition of the nanowire pitch. A plane wave is incident parallel to the nanowire axis (z-axis); (b) x-z cross-section of the 3D FDTD model used to analyse the optical properties of the array in (a). PML – perfectly matched layer boundary condition; (c) Reflection (R), transmission (T) and absorption (A) coefficients as a function of wavelength for an InP nanowire array with pitch of 360nm and nanowire diameter of 180nm (solid coloured lines), and for a nanowire array with pitch of 80nm and nanowire diameter of 40nm (dashed coloured lines). The black solid line shows absorption by a 392nm thick InP film; (d) The AM1.5 solar spectrum used for solar cell efficiency calculations.

propagates downwards in the simulation domain. This is used to simulate light incident from the Sun. Monitors above and below the nanowire determine the power emitted by the source as well as the power reflection by and transmitted through the nanowire. From this data absorption within the nanowire can be determined as a function of wavelength. Periodic boundary conditions are used perpendicular to the direction of light propagation to create an infinite square array of nanowires. Perfectly matched absorbing layers are used above the source and below the nanowire to eliminate unphysical reflections. The

calculated reflection, transmission and absorption coefficients for a plane wave at normal incidence are shown in Figure 2.1(c). The reflection coefficient is less than 0.04 for wavelengths longer than 360nm, whilst transmission through the array is similarly low, with a slight peak around 550nm which could likely be eliminated by use of longer nanowires. The net result is that absorption remains high across the entire wavelength of interest, at the very least 90%. Also shown are the corresponding values for a nanowire diameter of 40nm and pitch of 80nm (i.e. the same packing fraction). The latter case demonstrates how care must be taken to determine optimum parameters for the array – in this case high absorption at longer wavelengths can only be achieved by significantly increasing the length of the nanowires, which may prove impractical in reality. For comparison, the absorption coefficient for a planar InP thin film of 392nm thickness is shown (392nm = 2 μ m x 0.196). No antireflection coatings were used in the FDTD simulations. Weighting the AM1.5 solar spectrum (shown in Figure 2.1(d)¹⁵) with the absorption coefficient of the nanowire array allows the theoretical maximum short circuit current density J_{sc} of the solar cell formed from the array to be determined. This is given by

$$J_{sc} = \frac{q}{nhc} \int_0^{\lambda_g} \lambda a(\lambda) P_{AM1.5}(\lambda) d\lambda \quad (2.1)$$

where q is the electronic charge, h the Planck constant, c the speed of light, $P_{AM1.5}(\lambda)$ the solar spectral irradiance (units $\text{Wm}^{-2}\text{nm}^{-1}$), $a(\lambda)$ the material absorption coefficient and n the number of electrons per Coulomb. This calculation assumes that each above-bandgap photon is converted into a single electron-hole (e-h) pair within the absorbing material. For the ideal InP nanowire array discussed above the maximum short circuit current density determined from equation (2.1) has a value of $\sim 286\text{mAcm}^{-2}$. The corresponding

value for a 392nm thick planar InP film without an antireflection coating is only $\sim 187 \text{mAcm}^{-2}$. Whilst antireflection coatings (ARCs) can significantly enhance optical coupling into a planar structure over a limited angular incidence range, it has been shown that absorption by a nanowire array is relatively insensitive to the angle of incidence even in the absence of an ARC¹⁶, which provides further motivation for their use in solar cells.

2.2.2 Lattice mismatched nanowire epitaxy

A further advantage unique to the nanowire geometry lies in epitaxy considerations. To obtain optimum material quality during planar epitaxy it is advisable to minimise strain between the epitaxial layer and the underlying substrate. Strain is the product of lattice mismatched epitaxy, thus limiting the material combinations which can be grown beyond a critical thickness¹⁷. Above the critical thickness, strain energy is relieved through the formation of defects such as dislocations which act as recombination centres for charge carriers¹⁸. This has a negative impact on device efficiency and should be avoided in solar cells. Whilst irrelevant in the case of homogeneous growth this limitation becomes important when multi-junction (tandem) solar cells are designed. A multi-junction solar cell is formed from epitaxially-layered active regions with different bandgaps, enabling the absorption characteristics of the final solar cell to be tuned to better match the solar spectrum. The strain limitation on planar epitaxial growth prevents simple integration of many of the material combinations which would be ideal for this task. This limitation is greatly relaxed in the case of heterogeneous nanowire epitaxy, where the strain may be accommodated in the region of the nanowire close to the hetero-interface¹¹. Strain relief may occur through nanowire expansion in the radial direction, which is prevented in the case of thick planar layers. It is therefore possible to conceive of a much wider range of

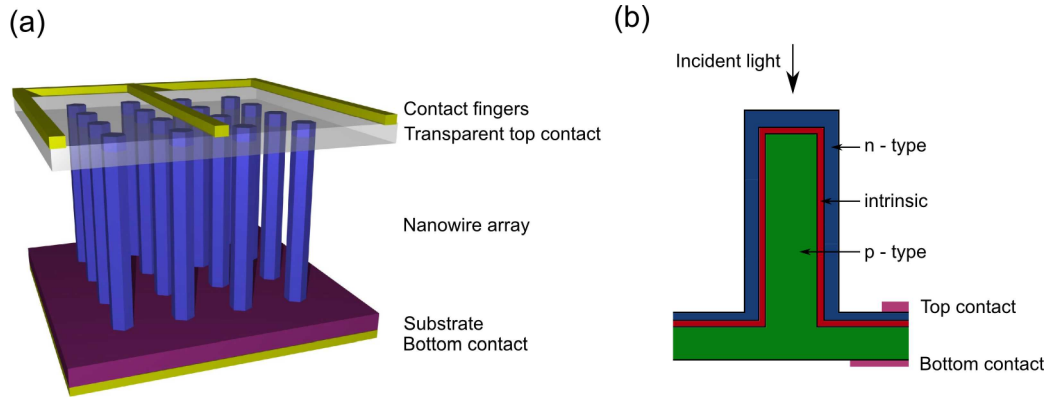


Figure 2.2. Leveraging the nanowire morphology for solar cell applications. (a) Schematic of a nanowire array solar cell with the potential for strongly lattice-mismatched nanowire growth; (b) Schematic cross-section of a single nanowire containing a radial p-n junction.

materials combinations utilising nanowire structures as absorbing elements of the solar cell. A schematic example of a solar cell formed from a nanowire array on a planar substrate is shown in Figure 2.2(a). This structure is investigated in more detail in section 2.4. In a similar manner, axially heterogeneous nanowires can be considered where the strain limitation is also relaxed.

2.2.3 Radial p-n junction in a nanowire

The unique columnar geometry presents the opportunity for realisation of a radial $p-n$ (or $p-i-n$) junction within a nanowire. This can be achieved by growth of a core-shell structure in which the core and shell are doped in a complementary manner, or by dopant diffusion as an *ex-situ* process. Radial growth of a nanowire shell can be undertaken by altering growth conditions such as temperature and adatom fluxes. The resulting structure is shown schematically in Figure 2.2(b). In a radial $p-i-n$ structure the light absorption pathway and the extraction of one carrier (electron or hole) can be made orthogonal

through correct contacting schemes. There is therefore the possibility for both enhanced light absorption and minimised recombination of one of the charge carriers, by increasing and decreasing the relevant path lengths respectively. The radial junction must be designed carefully however, as increasing the nanowire length may increase light absorption at the expense of a reduced operating voltage¹³.

2.3 Nanowire solar cells in the literature

The field of nanowire photovoltaics can be split into several distinct regimes. These include the use of single optoelectronically-active nanowires as nanoelectronic power sources; the employment of nanowire arrays as efficient antireflection coatings; and the application of nanowire arrays as functional elements of the solar cell. The latter is the most pertinent to the modelling discussed later in this chapter, and is discussed here in the most depth.

Single nanowires containing a p - n junction have the potential to supply power to nanoelectronic devices¹⁹. Typically, the nanowires are removed from the growth substrate and electrically contacted on a host substrate^{20,21}. The efficiency of the photovoltaic device in this case is usually calculated using the projected area of the nanowire, as the excitation source spot size is generally significantly larger than the nanowire itself, and the metal contacts reduce the absorption cross-section of the nanowire. This scheme and extensions thereof is the subject of a recent review article²². The current efficiency record for a single nanowire solar cell is 10.2% for a GaAsP nanowire²³. This measurement was undertaken with the nanowire lying horizontally on a host substrate hence the incident light was perpendicular to the nanowire growth axis. A particularly appealing aspect of single nanowire study is the possibility to carefully investigate fundamental nanowire

properties in the absence of ensemble averaging effects. However, whilst of interest as a nano-power source the resulting structure cannot harness several of the properties which make nanowire arrays so appealing for solar cell applications, for instance enhanced absorption through coupling to collective waveguide modes.

Coincident with the above, research was undertaken regarding arrays of vertical nanowires which were evaluated *in-situ* on a substrate. This was stimulated by early papers discussing the device physics of nanowire arrays for solar cells¹³ and demonstrating impressive antireflection properties of vertical silicon nanowire arrays²⁴. In the latter case a solar cell was formed from the array, although the antireflection properties did not translate at that time into enhanced device efficiency.

Many reports since have demonstrated the promising optical properties of nanowire arrays formed from a variety of semiconducting materials, for instance Si^{3,25}, InP²⁶ and GaP^{1,26}. Whilst these reports provided experimental evidence for antireflection by nanowire arrays, in many cases the nanowires were randomly located, complicating systematic study of the influence of physical parameters on optical properties. In contrast, such study is facilitated by growth of ordered arrays of nanowires, for instance by lithographic definition of the array. The optical properties of ordered arrays of nanowires have been evaluated theoretically^{10,27,28}. This revealed that antireflection and subsequent absorption of incident light is dependent on the modal properties of the array, in large part through the influence of two key optical modes as discussed in section 2.2.1.

A wide variety of columnar structures have been considered for photovoltaic devices, ranging from nanowires with diameter on the order of several nanometres²⁹ through to structures better described as micropillars^{30,31}. The quantum nature of semiconductor nanowires with diameter of a few nanometres was leveraged in the theoretical work of

Ref 29, namely by tuning the silicon nanowire absorption edge to better match the solar spectrum. However, extremely narrow nanowires suffer from poor optical absorption at long wavelengths which may be compensated only by increasing the nanowire length significantly, which may prove experimentally unfeasible. In contrast, micropillar structures with diameters ranging from $1.5\mu\text{m}$ to $50\mu\text{m}$ ³⁰⁻³² have been utilised with solar energy conversion in mind. Whilst micropillars may reduce the impact of surface recombination on device performance relative to the nanowire morphology, it is unlikely that they can match the impressive absorption characteristics of nanowire structures.

Variations on the theme include arrays containing varying diameter nanowires³³ and designs utilising tapered nanowires³⁴. The former was designed to maximise the *p-n* junction surface area by forming radial *p-n* junctions within microwires interspersed with nanowires to reduce overall reflection. The latter was designed to increase the effective refractive index of the array from top to bottom, thereby reducing reflection and enhancing the coupling of light into the array.

Although investigation into silicon nanowire arrays for solar cells has dominated the field to date (most likely due to the current dominant status of silicon in the photovoltaic market) the current record for a single junction nanowire array solar cell is held by the InP material system³⁵ and stands at 13.8%. Significant improvement upon this value may be possible. In Ref 10 the theoretical efficiency limits for an InP nanowire array solar cell were calculated in the radiative recombination limit. In the design space considered an upper limit of $\sim 30\%$ was determined for nanowires $2\mu\text{m}$ in length, with a diameter of 180nm and pitch of 360nm . This compares extremely favourably with the Shockley-Queisser limit of $\sim 33\%$ for a planar silicon solar cell, as the material requirement is reduced significantly.

Whilst the majority of research referred to previously concerned single junction solar cells, investigation into multi-junction nanowire solar cells has begun recently. One of the dominant loss mechanisms in the conversion of solar photons to electricity lies in the rapid thermalisation of carriers to the band edge within the absorbing material³⁶. The most common approach to this problem is to utilise multiple active regions within the solar cell, each with a different bandgap chosen such that the overall absorption of light is maximised. The resulting multi-junction solar cell holds the current efficiency record of 37.9% for single sun illumination³⁷. A multi-junction cell is also achievable utilising the nanowire architecture, for instance through growth of different material segments within the nanowires³⁸. The tunnel junctions required by such a design have been successfully realized within individual nanowires³⁹. Alternatively, an active growth substrate can be considered, such that a nanowire-planar tandem solar cell is formed. Limited theoretical descriptions of this structure have been presented in the literature to date. Two specific cases have been considered in which the fraction of light absorbed by the nanowire array was limited to the projected area of the array²⁹ or set to unity⁴⁰. In both cases a silicon substrate was assumed. From an experimental perspective, design guidelines for such a solar cell should ideally consider the full range of potential material combinations, and realistic absorption within the nanowire array. In the following, the theoretical efficiency limits for a nanowire-planar tandem solar cell are evaluated first for the case of a variable substrate and nanowire bandgap, and then with the substrate made from silicon. To account for the real world situation in which the nanowire array demonstrates imperfect absorption characteristics, an effective absorption fraction P_{eff} is introduced, and the efficiency limits are evaluated with regard to this parameter also. Note that some of these results have been published elsewhere⁴¹.

2.4 Modelling the nanowire-planar tandem solar cell

2.4.1 Theory

The ultimate radiative efficiency limit for a solar cell was first calculated for a planar device in 1961 by William Shockley and Hans Queisser⁴². A review of the model is first presented for the case of a single planar solar cell, before the model is adapted to consider the tandem nanowire-planar solar cell.

The principle of detailed balance is used to ensure particle conservation when the solar cell is in the quasi-equilibrium operational state. In the model, each incident solar photon with energy greater than the solar cell material bandgap is converted within the solar cell to a single e–h pair. The absorbed solar photon flux per unit area F_s is given by

$$F_s = \int_{E_g}^{E_{max}} \phi(E) dE \quad (2.2)$$

where $\phi(E)$ is the AM1.5 solar spectrum, E_g the bandgap of the solar cell and $E_{max}=4.14\text{eV}$ corresponds to the maximum photon energy of the AM1.5 spectrum. AM1.5 is commonly used as a benchmark for the determination of solar cell efficiencies, and corresponds to the solar flux received at ground level after traversing a path length equal to 1.5 times the height of the Earth’s atmosphere. For a solar cell to be used in space applications (e.g. on a satellite), the AM0 spectrum is more suitable.

Multi-exciton generation is only relevant when the incident photon energy is at the very least twice the bandgap energy (and is generally required to be greater to have a significant effect) and equation (2.2) is therefore an acceptable approximation for most solar cell materials (bandgap $\sim 1\text{eV}$). Photons with energy lower than the bandgap are

transmitted and may be ignored. Strictly speaking the absorption of thermal photons from the ambient should be included in the model, but the low temperature of the solar cell surroundings ($\sim 300\text{K}$) makes this effect a minor perturbation on the final results⁴³.

All e–h pairs are assumed to immediately thermalise to the conduction band minimum / valence band maximum and are separated by the inbuilt electric field of the p - n junction, after which the electron and hole populations can be described using respective quasi-Fermi levels. The presence of separated light-induced charge carriers forward biases the p - n junction, with the resulting current-voltage relationship under load determined by modelling the p - n junction solar cell as an ideal single diode.

$$I = I_L + I_0 \left[1 - \exp\left(\frac{qV}{k_B T_c}\right) \right] \quad (2.3)$$

where $I_L = q(F_s - F_0)$ is the short circuit current, $I_0 = qF_0$ is the reverse saturation current, V is the cell voltage, k_B is the Boltzmann constant and T_c is the cell temperature (taken as 300K). F_0 is determined in equation (2.4). Carrier thermalisation ensures that the open circuit voltage is limited to the bandgap equivalent voltage. Once an e–h pair is created and separated to either electrical contact, carrier extraction at the Ohmic contact occurs without loss.

Spontaneous radiative recombination is the only efficiency-limiting process acting on the device, limiting the number of carriers which arrive at the Ohmic contacts. The recombination rate F_0 is calculated by modelling the device as a blackbody, with recombination taking the form of the Planck blackbody photon flux for energies greater than the solar cell bandgap, with

$$F_0 = \int_{E_g}^{\infty} N(E, T_c) dE \quad (2.4)$$

where

$$N(E, T) = \frac{2\pi h^2}{c^2} \frac{E^2}{\exp\left(\frac{E}{k_B T}\right) - 1}. \quad (2.5)$$

The chemical potential of the device under illumination is non-zero due to the non-zero operating voltage V , and is defined as $\mu=qV$. This is accounted for in equation (2.3). The potential is considered to be constant throughout the solar cell. As the current increases the forward bias induced within the diode increases also, to the point where the dark current (derived from the Planck blackbody photon flux) equals the light-induced current, and the power produced by the device falls to zero. A final assumption of the model is that the absorptivity and emissivity of the semiconductor are equal to unity⁴⁴.

The detailed balance model described above is now adapted to consider a tandem nanowire-planar solar cell. In the case of a tandem solar cell, the upper integration limit in equation (2.2) is modified to account for absorption in any subcells above the one in question. For the top subcell the integration is undertaken from the bandgap energy to infinity, whilst for the lower subcells the upper integration limit is governed by the bandgap of the subcell immediately above. This assumes perfect absorption within the subcells. As a first approximation of the effect of an absorbing nanowire array forming the upper subcell of a two subcell device, an effective absorption fraction $P_{eff} \leq 1$ is introduced to account for imperfect absorption in the nanowire array. Absorption per unit area by the nanowire array is thus calculated to be

$$F_{s,array} = P_{eff} \int_{E_{g,NW}}^{E_{max}} \phi(E) dE. \quad (2.6)$$

Whilst a simple approximation of this kind is also valid in the case of an imperfectly absorbing thin film, a significant advantage arises in using nanowire arrays instead of thin planar films due to the relaxation of the lattice matching criterion for nanowire epitaxy discussed in section 2.2.2.

For the planar substrate of the two subcell device, absorption is now enhanced as the fraction $1 - P_{eff}$ of photons not absorbed by the nanowire array is assumed to be transmitted and can be absorbed within this subcell. This is a fair assumption given that adequate design of the nanowire array can result in significant suppression of reflected light – the majority of photons not absorbed by the array may be transmitted instead. Whilst in reality P_{eff} would be a function of energy, in the detailed balance limit only the absolute number of photons absorbed is relevant due to thermalisation of carriers to the band edge.

Absorption per unit area by the substrate is thus given by

$$F_{s,subs} = \int_{E_{g,subs}}^{E_{g,NW}} \phi(E) dE + (1 - P_{eff}) \int_{E_{g,subs}}^{E_{\infty}} \phi(E) dE. \quad (2.7)$$

Enhanced absorption by a nanowire array comes at the expense of enhancement of the spontaneous emission rate for an emitter within the array. In the strict detailed balance limit this needs to be accounted for. However, a calculation of the Purcell enhancement demands knowledge of the exact array structure under consideration, whereas the current aim is to provide design guidelines for a broad range of potential structures. Calculations of the Purcell effect for a dipole emitter within a nanowire array¹⁰ suggest that this does

not have a severe impact on the ultimate efficiency in the radiative detailed balance limit. As an approximation, the radiative recombination rate is assumed equal to that of a planar film. This may well overestimate the recombination rate and therefore reduce the calculated maximum efficiencies slightly. For the nanowire array, photons may be emitted from both the upper and lower surfaces of the array, hence the recombination rate per unit area $F_{0,NW}$ is given by

$$F_{0,NW} = 2 \int_{E_{g,NW}}^{\infty} N(E, T_c) dE. \quad (2.8)$$

In the case of the substrate a theoretical ideal reflector is placed at the underside of the subcell, and the recombination rate for this subcell is therefore given by

$$F_{0,subs} = \int_{E_{g,subs}}^{\infty} N(E, T_c) dE. \quad (2.9)$$

Absorption within the substrate of photons emitted by the nanowire (and vice versa) is excluded from the model, as it has been shown to have only a small effect on the resulting efficiencies⁴⁵.

To calculate the maximum efficiency limit for the tandem solar cell, a series constraint is applied such that the current flowing through each subcell is identical. The resulting power generated is given by

$$P = I [V_{NW}(I) + V_{subs}(I)] \quad (2.10)$$

and the current at the maximum power point is determined by

$$\frac{dP}{dI} = 0. \quad (2.11)$$

The limiting efficiency of the device is found by dividing the resulting maximum power by the total power per unit area contained within the AM1.5 solar spectrum. The final results are calculated assuming a subcell temperature of 300K.

In the code used to solve the above equations, the maximum power point was determined numerically as follows. Combining equations (2.3) and (2.10) gives

$$P = \frac{kT_c I}{q} \ln \left[\frac{I_{L1} + I_{01} - I}{I_{01}} \cdot \frac{I_{02}}{I_{L2} + I_{02} - I} \right]. \quad (2.12)$$

Recalling that $I_{Li} = q(F_{si} - F_{0i})$ and $I_{0i} = qF_{0i}$, this becomes

$$P = \frac{kT_c I}{q} \ln \left[\frac{qF_{s1} - I}{qF_{01}} \cdot \frac{qF_{02}}{qF_{s2} - I} \right]. \quad (2.13)$$

Ignoring the trivial case for which $P=I=0$ (which determines the open circuit voltage), zero power is generated when the argument of the logarithm is equal to unity. Solving for the short circuit current $I=I_{sc}$ gives

$$I_{sc} = \frac{q}{2} \left[(F_{s1} + F_{s2}) - \sqrt{(F_{s1} - F_{s2})^2 + 4F_{01}F_{02}} \right]. \quad (2.14)$$

Iterating the current in small negative steps from I_{sc} and evaluating equation (2.13) it is then possible to determine the maximum power point.

2.4.2 Results

Using the equations presented above for the case of a single planar solar cell with a rear reflector to minimise radiative recombination, a maximum efficiency of 33.4% was determined for a bandgap of 1.13eV. This is in agreement with other reports in the literature⁴⁶ (small differences can occur due to variation in the exact solar spectrum used within the calculations, and the use of assumptions regarding absorption of the ambient flux). By coincidence this is approximately the bandgap of silicon, currently the most ubiquitous solar cell material. This limit serves as the absolute minimum required efficiency for the tandem nanowire-planar solar cell, in which the aim is to overcome the Shockley-Queisser single cell limit.

The tandem nanowire-planar solar cell was first analysed in the regime in which both the substrate and nanowire bandgaps were freely varied. The efficiency limits in this situation are presented in Figure 2.3 as a function of the respective bandgaps, for two cases of medium ($P_{eff}=80\%$) and high ($P_{eff}=95\%$) absorption by the nanowire array. The contour plots highlight the range of bandgap choices which offer the greatest promise for high efficiency in the radiative limit. There is a band of maximum efficiency (the red region on each plot) which upon closer analysis reveals two maximum efficiency points with little difference in absolute limiting efficiency ($< 1\%$). These points are highlighted in Figure 2.3(a) and 2.3(b) with a square and a circle. The efficiency limits are investigated in more detail in Figure 2.3(c). It is interesting to note that the ideal substrate bandgap is largely independent of the effective packing fraction P_{eff} , and for one of the maxima this bandgap corresponds to that of silicon. As partial confirmation of the model accuracy, it can be seen that for $P_{eff}=1$ the ideal bandgap determined for a perfectly absorbing two subcell tandem solar cell is reproduced (1.7eV).

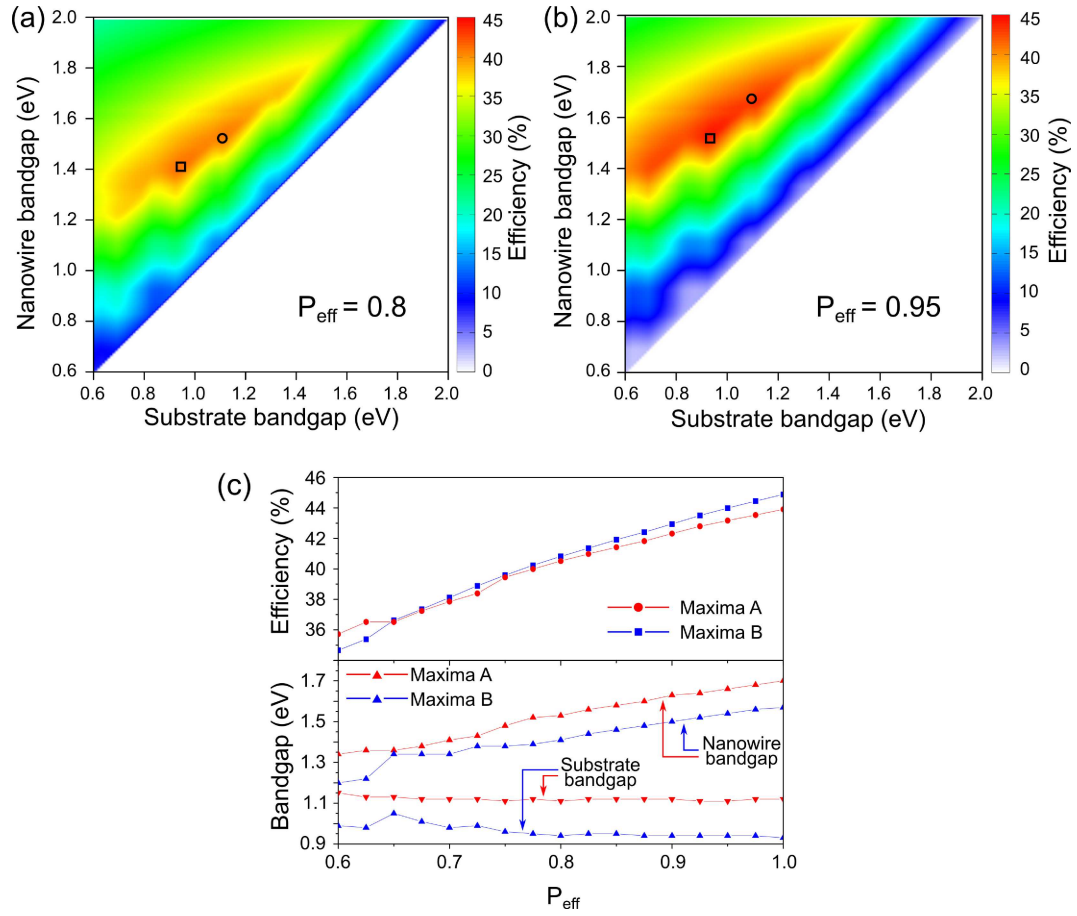


Figure 2.3. Efficiency limits for a tandem solar cell formed from a nanowire array grown on a planar substrate. Efficiency as a function of nanowire and substrate bandgaps for the case of (a) 80% and (b) 95% absorption of above-bandgap energy photons in the nanowire array; (c) Upper panel - Efficiency as a function of nanowire absorption fraction P_{eff} for the two maximal efficiency regions, A and B. Lower panel – nanowire and substrate bandgaps associated with maxima A and B. The maxima are highlighted in (a) and (b) as a circle (maxima A) and square (maxima B).

Given the extensive use of silicon within the solar cell industry and the maturity of silicon technology, the requirement in the radiative limit for a silicon substrate in this device is encouraging. Furthermore, heterogeneous growth of III-V nanowires on silicon substrates has already been demonstrated^{23,47–50}. Figure 2.4(a) shows the efficiency limits associated with the growth of variable bandgap nanowires on a silicon substrate ($E_g=1.12\text{eV}$) as a function of P_{eff} . The solid line traces the maximum efficiency as a function of P_{eff} .

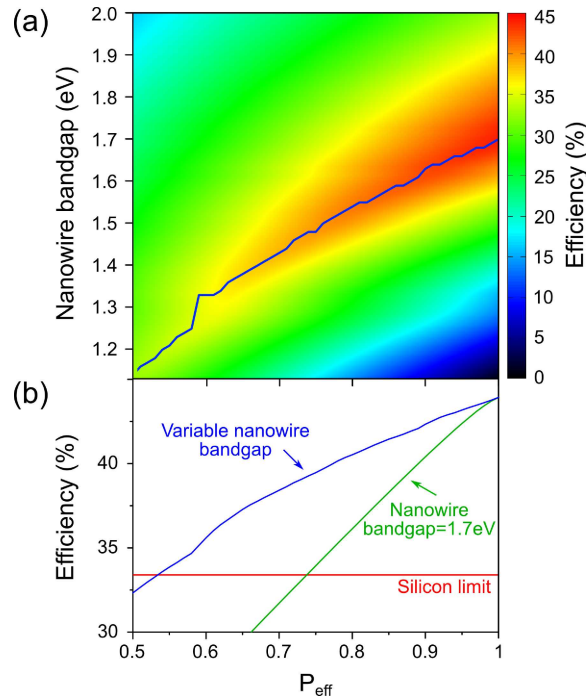


Figure 2.4. Efficiency limits for a nanowire array–silicon substrate tandem solar cell. (a) Efficiency limits as a function of nanowire bandgap and absorption fraction P_{eff} for an array grown on silicon ($E_g=1.12\text{eV}$). Solid line gives maximum efficiency for each value of P_{eff} . (b) Efficiency as a function of P_{eff} for the case of variable nanowire bandgap (blue line) and nanowire bandgap fixed at 1.7eV (green line). The efficiency limit for a single planar silicon solar cell is given for reference (red line).

As expected, it is clear that in the case of an imperfectly absorbing nanowire array the bandgap of the array must be reduced relative to the perfectly absorbing case, in order that maximum efficiency for the device can be obtained. To investigate this further, Figure 2.4(b) shows the efficiency limits extracted from Figure 2.4(a) for a nanowire array with ideal bandgap grown on a silicon substrate, and compares the limits to the case where the array has a fixed bandgap $E_g=1.7\text{eV}$, corresponding to the perfectly absorbing array ($P_{eff}=1$). The latter case was considered in one of the few papers to date investigating this problem⁴⁰. The plot also shows the range of P_{eff} for which the nanowire-planar tandem solar cell holds greater promise of high efficiency than an all silicon single

cell approach. It is clearly important that the nanowire bandgap is chosen to reflect the absorption properties of the array, and not simply chosen to be 1.7eV. For $P_{eff}=80\%$, the efficiency limit in the latter case is 36.3%, whilst this can be significantly increased to 40.8% by reducing the nanowire bandgap to 1.53eV. Whilst this is inferior to the optimum case (nanowire bandgap 1.57eV, substrate bandgap 0.93eV and efficiency limit of 45%) the real world advantage of using a silicon substrate is extremely important.

Figure 2.4(b) shows that below a certain value of P_{eff} both the case of variable nanowire bandgap and the case of fixed nanowire bandgap ($E_g=1.7\text{eV}$) result in an efficiency limit which lies below that of a single planar silicon solar cell. In the case of the fixed bandgap, this occurs below $P_{eff}=72\%$ when insufficient current is generated by the nanowire array compared with that produced by the substrate. The result is a drop in efficiency which cannot be compensated by using a large nanowire bandgap (and therefore a potentially higher working voltage and power). For the case of variable nanowire bandgap, the efficiency limit drops below that of silicon for $P_{eff} < 52\%$. Under these conditions both of the subcells generate approximately the same current (as the nanowire bandgap is very close to that of silicon). However, the presence of a $p-n$ junction in both of the subcells leads to an increase in radiative recombination, slightly reducing the efficiency and explaining why the condition is $P_{eff} < 52\%$ and not 50%. The above considerations show that in the case of variable nanowire bandgap there is a wider range of P_{eff} which results in higher-than-silicon efficiency than for a fixed bandgap of 1.7eV.

At this point it is instructive to consider the limitations of the current model and propose directions for future refinement of the approach presented here. The simplest, though most time consuming approach is to model a multitude of different nanowire array

structures using for instance the FDTD technique. The FDTD method would allow inclusion of reflection within the model, as well as considering more accurately the behaviour of photons below the nanowire bandgap as they traverse the nanowire array. For instance, a nanowire array designed to optimally absorb light is not necessarily designed for maximum transmission of below bandgap light through the array. This is evident from Figure 2.5, in which absorption in an InP nanowire array is shown to be high but transmission of below-bandgap photons to the underlying silicon substrate is relatively poor (although still an improvement on the case for planar silicon without antireflection coatings). The nanowire array considered here has the same dimensions as discussed in Figure 2.1. FDTD simulations in this vein have been reported recently^{51,52}.

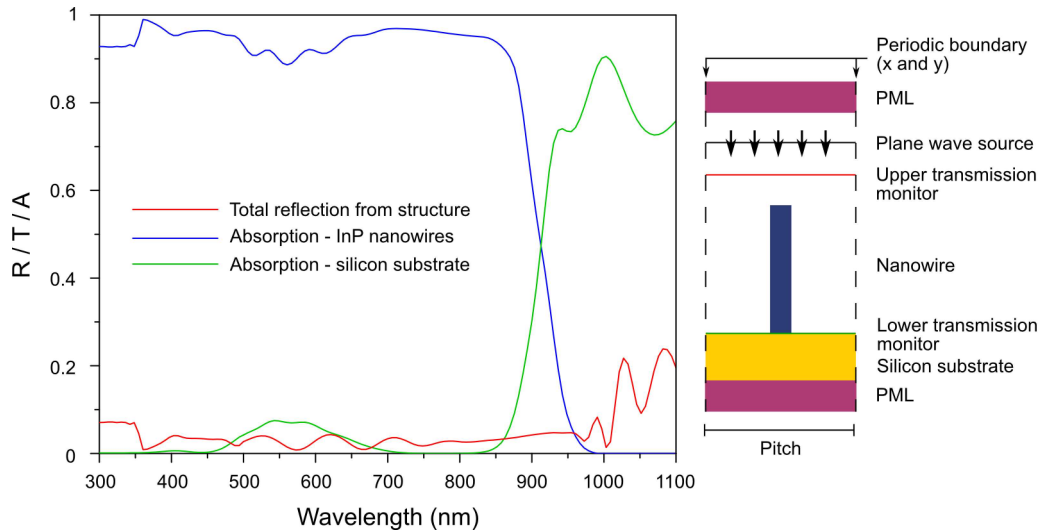


Figure 2.5. FDTD simulations of the optical properties of an InP nanowire array on a semi-infinite silicon substrate. The simulation domain is given in the right hand side schematic. The graph shows the absorption coefficients for the nanowire array and silicon substrate (blue and green lines respectively) alongside the reflection coefficient (red lines). The non-zero absorption coefficient for InP nanowires just below the InP bandgap (~925nm) arises from the refractive index fitting procedure.

The electronic properties of the solar cell, although not applicable within the ultimate radiative detailed balance limit, are equally important and a full model would include these as well. Limited work in this fashion has been undertaken for the nanowire-planar tandem solar cell, first in the case of perfect absorption within the nanowire array⁴⁰ and more recently for simulated absorption properties⁵¹.

2.5 Conclusion

An optical model for the nanowire-planar tandem solar cell has been developed within the framework of the principle of detailed balance. An effective packing fraction P_{eff} was introduced to account for imperfect absorption within the nanowire array. When both the nanowire bandgap and the substrate bandgap were freely varied to maximise the device efficiency, a device with a silicon substrate ($E_g=1.12\text{eV}$) was found to be close to optimum. For realistic P_{eff} values between 80% and 95% the optimum nanowire bandgap was determined to vary between 1.53eV and 1.66eV, with resulting efficiency limits between 40.8% and 43.3%. It is therefore important that the nanowire bandgap is chosen with the absorption properties of the array in mind, and not fixed to the optimum bandgap of 1.7eV for a perfectly absorbing upper subcell. The model provides design guidelines for the experimental realisation of the nanowire-planar tandem solar cell. Future work should investigate the influence of non-radiative recombination on the design guidelines, as this would be of particular relevance in a real world nanowire solar cell.

Bibliography

- (1) Diedenhofen, S. L.; Vecchi, G.; Algra, R. E.; Hartsuiker, A.; Muskens, O. L.; Immink, G.; Bakkers, E. P. A. M.; Vos, W. L.; Rivas, J. G. *Adv. Mater.* **2009**, *21*, 973–978.
- (2) Lee, Y.-J.; Ruby, D. S.; Peters, D. W.; McKenzie, B. B.; Hsu, J. W. P. *Nano Lett.* **2008**, *8*, 1501–5.
- (3) Srivastava, S. K.; Kumar, D.; Singh, P. K.; Kar, M.; Kumar, V.; Husain, M. *Sol. Energy Mater. Sol. Cells* **2010**, *94*, 1506–1511.
- (4) Tsakalacos, L.; Balch, J.; Fronheiser, J.; Korevaar, B. A.; Sulima, O.; Rand, J. *Appl. Phys. Lett.* **2007**, *91*, 233117.
- (5) Stelzner, T.; Pietsch, M.; Andrä, G.; Falk, F.; Ose, E.; Christiansen, S. *Nanotechnology* **2008**, *19*, 295203.
- (6) Garnett, E.; Yang, P. *Nano Lett.* **2010**, *10*, 1082–7.
- (7) Kelzenberg, M. D.; Boettcher, S. W.; Petykiewicz, J. A.; Turner-Evans, D. B.; Putnam, M. C.; Warren, E. L.; Spurgeon, J. M.; Briggs, R. M.; Lewis, N. S.; Atwater, H. A. *Nat. Mater.* **2010**, *9*, 239–44.
- (8) Kailuweit, P.; Peters, M.; Leene, J.; Mergenthaler, K.; Dimroth, F.; Bett, A. W. *Prog. Photovoltaics* **2011**, *20*, 945–953.
- (9) Mariani, G.; Wong, P.-S.; Katzenmeyer, A. M.; Léonard, F.; Shapiro, J.; Huffaker, D. L. *Nano Lett.* **2011**, *11*, 2490–4.
- (10) Kupec, J.; Stoop, R. L.; Witzigmann, B. *Opt. Express* **2010**, *18*, 27589–27605.
- (11) Ertekin, E.; Greaney, P. A.; Chrzan, D. C.; Sands, T. D. *J. Appl. Phys.* **2005**, *97*, 114325.
- (12) Spurgeon, J. M.; Plass, K. E.; Kayes, B. M.; Brunschwig, B. S.; Atwater, H. A.; Lewis, N. S. *Appl. Phys. Lett.* **2008**, *93*, 032112.
- (13) Kayes, B. M.; Atwater, H. A.; Lewis, N. S. *J. Appl. Phys.* **2005**, *97*, 114302.
- (14) Hu, L.; Chen, G. *Nano Lett.* **2007**, *7*, 3249–52.
- (15) Reference Solar Spectral Irradiance: Air Mass 1.5
<http://rredc.nrel.gov/solar/spectra/am1.5/>.

-
- (16) Sturmberg, B. C. P.; Dossou, K. B.; Botten, L. C.; Asatryan, A. A.; Poulton, C. G.; de Sterke, C. M.; McPhedran, R. C. *Opt. Express* **2011**, *19 Suppl 5*, A1067–81.
- (17) Pohl, U. W. *Epitaxy of Semiconductors: Introduction to Physical Principles; XIV.*; Springer, 2013.
- (18) Alberi, K.; Branz, H. M.; Guthrey, H.; Romero, M. J.; Martin, I. T.; Teplin, C. W.; Stradins, P.; Young, D. L. *Appl. Phys. Lett.* **2012**, *101*, 123510.
- (19) Tian, B.; Zheng, X.; Kempa, T. J.; Fang, Y.; Yu, N.; Yu, G.; Huang, J.; Lieber, C. M. *Nature* **2007**, *449*, 885–9.
- (20) Kelzenberg, M. D.; Turner-Evans, D. B.; Kayes, B. M.; Filler, M. A.; Putnam, M. C.; Lewis, N. S.; Atwater, H. A. *Nano Lett.* **2008**, *8*, 710–4.
- (21) Kempa, T. J.; Tian, B.; Kim, D. R.; Hu, J.; Zheng, X.; Lieber, C. M. *Nano Lett.* **2008**, *8*, 3456–60.
- (22) Kempa, T. J.; Day, R. W.; Kim, S.-K.; Park, H.-G.; Lieber, C. M. *Energy Environ. Sci.* **2013**, *6*, 719.
- (23) Holm, J. V.; Jorgensen, H. I.; Krogstrup, P.; Nygard, J.; Liu, H.; Aagesen, M. *Nat. Commun.* **2013**, *4*, 1498.
- (24) Peng, K.; Xu, Y.; Wu, Y.; Yan, Y.; Lee, S.-T.; Zhu, J. *Small* **2005**, *1*, 1062–7.
- (25) Tsakalacos, L. *J. Nanophotonics* **2007**, *1*, 013552.
- (26) Muskens, O. L.; Rivas, J. G.; Algra, R. E.; Bakkers, E. P. A. M.; Lagendijk, A. *Nano Lett.* **2008**, 2–6.
- (27) Kupec, J.; Witzigmann, B. *Opt. Express* **2009**, *17*, 10399–410.
- (28) Li, J.; Yu, H.; Wong, S. M.; Li, X.; Zhang, G.; Lo, P. G.-Q.; Kwong, D.-L. *Appl. Phys. Lett.* **2009**, *95*, 243113.
- (29) Kandala, A.; Betti, T.; Fontcuberta i Morral, A. *Phys. Status Solidi A* **2009**, *206*, 173–178.
- (30) Yoon, H. P.; Yuwen, Y. A.; Kendrick, C. E.; Barber, G. D.; Podraza, N. J.; Redwing, J. M.; Mallouk, T. E.; Wronski, C. R.; Mayer, T. S. *Appl. Phys. Lett.* **2010**, *96*, 213503.
- (31) Kayes, B. M.; Filler, M. A.; Henry, M. D.; Maiolo III, J. R.; Kelzenberg, M. D.; Putnam, M. C.; Spurgeon, J. M.; Plass, K. E.; Scherer, A.; Lewis, N. S.; Atwater, H. A. *2008 33rd IEEE Photovolt. Spec. Conf.* **2008**, 1–5.

-
- (32) Kayes, B. M.; Filler, M. A.; Putnam, M. C.; Kelzenberg, M. D.; Lewis, N. S.; Atwater, H. A. *Appl. Phys. Lett.* **2007**, *91*, 103110.
- (33) Jung, J.-Y.; Guo, Z.; Jee, S.-W.; Um, H.-D.; Park, K.-T.; Hyun, M. S.; Yang, J. M.; Lee, J.-H. *Nanotechnology* **2010**, *21*, 445303.
- (34) Fan, Z.; Kapadia, R.; Leu, P. W.; Zhang, X.; Chueh, Y.-L.; Takei, K.; Yu, K.; Jamshidi, A.; Rathore, A. A.; Ruebusch, D. J.; Wu, M.; Javey, A. *Nano Lett.* **2010**, *10*, 3823–7.
- (35) Wallentin, J.; Anttu, N.; Asoli, D.; Huffman, M.; Aberg, I.; Magnusson, M. H.; Siefert, G.; Fuss-Kailuweit, P.; Dimroth, F.; Witzigmann, B.; Xu, H. Q.; Samuelson, L.; Deppert, K.; Borgström, M. T. *Science*. **2013**, *339*, 1057–60.
- (36) Hirst, L. C.; Ekins-Daukes, N. J. *Prog. Photovoltaics* **2011**, 286–293.
- (37) Green, M. A.; Emery, K.; Hishikawa, Y.; Warta, W.; Dunlop, E. D. *Prog. Photovoltaics* **2013**, 827–837.
- (38) Heurlin, M.; Wickert, P.; Fält, S.; Borgström, M. T.; Deppert, K.; Samuelson, L.; Magnusson, M. H. *Nano Lett.* **2011**, *11*, 2028–31.
- (39) Wallentin, J.; Persson, J. M.; Wagner, J. B.; Samuelson, L.; Deppert, K.; Borgström, M. T. *Nano Lett.* **2010**, *10*, 974–9.
- (40) LaPierre, R. R. *J. Appl. Phys.* **2011**, *110*, 014310.
- (41) Foster, A. P.; Wilson, L. R. *Phys. Status Solidi (A)* **2013**, *210*, 425–429.
- (42) Shockley, W.; Queisser, H. J. *J. Appl. Phys.* **1961**, *32*, 510–519.
- (43) Henry, C. H. *J. Appl. Phys.* **1980**, *51*, 4494.
- (44) Araujo, G. L.; Marti, A. *Sol. Energy Mater. Sol. Cells* **1994**, *33*, 213–240.
- (45) De Vos, A. *J. Phys. D. Appl. Phys.* **1980**, *13*, 839–846.
- (46) Tiedje, T. O. M.; Yablonovitch, E. L. I.; Cody, G. D.; Brooks, B. G. *IEEE Trans. Electron Devices* **1984**, 711–716.
- (47) Couto, O. D. D.; Sercombe, D.; Puebla, J.; Otubo, L.; Luxmoore, I. J.; Sich, M.; Elliott, T. J.; Chekhovich, E. A.; Wilson, L. R.; Skolnick, M. S.; Liu, H. Y.; Tartakovskii, A. I. *Nano Lett.* **2012**, *12*, 5269–74.
- (48) Jabeen, F.; Grillo, V.; Rubini, S.; Martelli, F. *Nanotechnology* **2008**, *19*, 275711.

- (49) Mi, Z. *J. Nanophotonics* **2009**, *3*, 031602.
- (50) Yu, S.; Miao, G.; Jin, Y.; Zhang, L.; Song, H.; Jiang, H.; Li, Z.; Li, D.; Sun, X. *Phys. E Low-Dimensional Syst. Nanostructures* **2010**, *42*, 1540–1543.
- (51) Huang, N.; Lin, C.; Povinelli, M. L. *J. Appl. Phys.* **2012**, *112*, 064321.
- (52) Wen, L.; Li, X.; Zhao, Z.; Bu, S.; Zeng, X.; Huang, J.; Wang, Y. *Nanotechnology* **2012**, *23*, 505202.

3 Fabrication and growth of GaAs nanowire arrays

3.1 Introduction

Semiconductor nanowires are most commonly fabricated in a catalysed process, in which a nanoparticle such as gold is used to seed the nanowire growth¹. The catalyst is first deposited onto a suitable substrate, for instance a crystalline inorganic semiconductor. Gases or molecular beams containing the adatoms for growth are then passed over the surface of the heated substrate, incorporating within the molten catalyst and forming a supersaturated eutectic alloy. Crystalline semiconductor then precipitates out below the nanoparticle and a nanowire is formed. This process is known as the vapour-liquid-solid (VLS) growth mode, and is shown schematically in Figure 3.1(a). In a similar manner, self-catalysed growth has been developed, in which the catalyst droplet (typically a group-III element) is formed from a constituent element of the final nanowire².

An alternative nanowire growth technique is the catalyst-free method. Here, a small opening defined within a growth mask such as SiO₂ deposited on a semiconductor substrate is used to determine the nanowire nucleation site. Given the correct choice of growth substrate crystal orientation, vertical nanowires can be obtained due to the difference in growth rates on different crystal facets of the nanowire³. This is shown in Figure 3.1(b). Advantages of this method compared to the VLS technique include the prevention of impurity incorporation in the nanowire from the catalyst⁴ and the potential

for higher quality interfaces in nanowire heterostructures, as the VLS technique may be affected by a catalyst reservoir effect^{5,6}. Many such heterointerfaces have been realised to date, including axial quantum wells^{7,8} and quantum dots⁹ and radial core-shell structures¹⁰. Devices resulting from the catalyst-free growth of nanowires include light emitting diodes¹¹, solar cells¹² and lasers¹³. Heterogeneous growth via this technique has also been reported, for example InGaAs on InP^{14,15}.

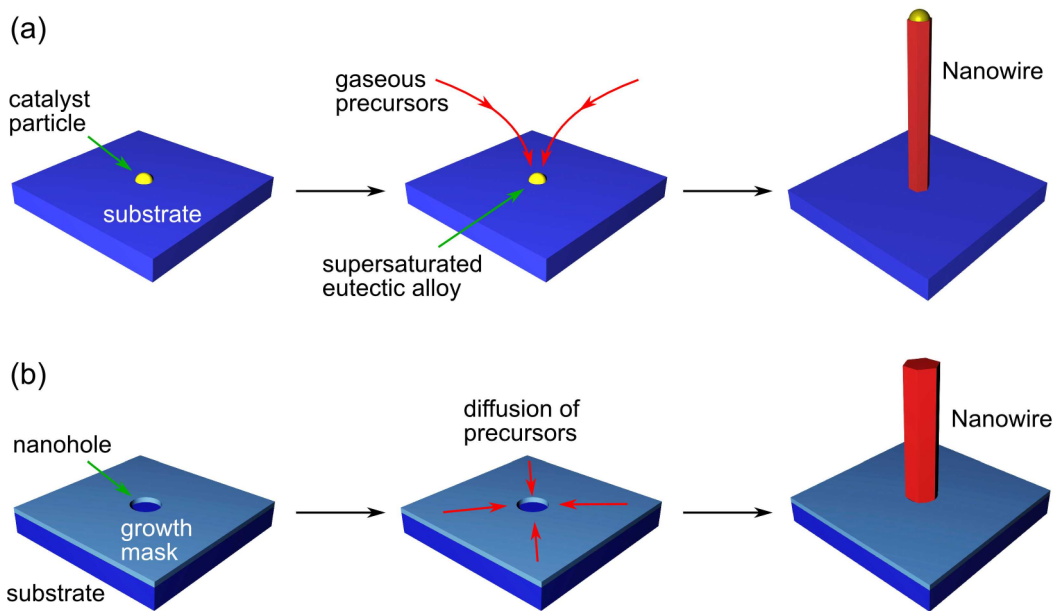


Figure 3.1. Overview of nanowire growth techniques. (a) Summary of the vapour-liquid-solid (VLS) growth procedure. (Left to right) A catalyst is deposited onto the substrate; Gaseous precursors containing the adatoms for growth incorporate within the molten catalyst at high temperature, forming a supersaturated eutectic alloy; Adatoms precipitate out at the catalyst-substrate interface, forming a crystalline nanowire; Note the metal catalyst remains at the top of the nanowire after growth has finished; (b) Summary of the catalyst-free growth process. (Left to right) An opening is formed within a thin dielectric growth mask on a crystalline substrate; Precursors containing the adatoms for growth diffuse across the growth mask and incorporate within the opening; a nanowire forms from within the opening. Both procedures rely on the correct choice of growth conditions.

This chapter describes in detail epitaxial growth studies implemented for GaAs nanowires using selective area (catalyst-free) metal organic chemical vapour deposition (MOCVD). Development of the growth of nanowires at Sheffield was necessary for the progress of this work, allowing for the novel developments in Chapters 3-5. An overview of the growth process is first presented in section 3.2, followed by details of the fabrication steps undertaken prior to growth in section 3.3. Nanowire growth studies are then discussed in section 3.4.

3.2 Overview of the growth technique

The GaAs nanowire samples produced in the course of this research were grown by a catalyst-free MOCVD technique. The nanowires were grown from nanoholes etched through a ~30nm thick SiO₂ dielectric film deposited on a semi-insulating (111)B orientated GaAs substrate. The nanoholes were produced in square arrays using a combination of electron beam lithography (EBL) and reactive ion etching (RIE). To moderate the nanowire growth rate, the SiO₂ film was patterned into squares with side length of 130µm. This allowed for planar growth to occur on the exposed GaAs substrate between SiO₂ squares simultaneously with nanowire growth.

In the following sections, a detailed description of the fabrication process prior to nanowire growth is presented. A schematic overview of the development process prior to loading the patterned substrate in the MOCVD reactor is shown in Figure 3.2 and may be referred to throughout section 3.3.

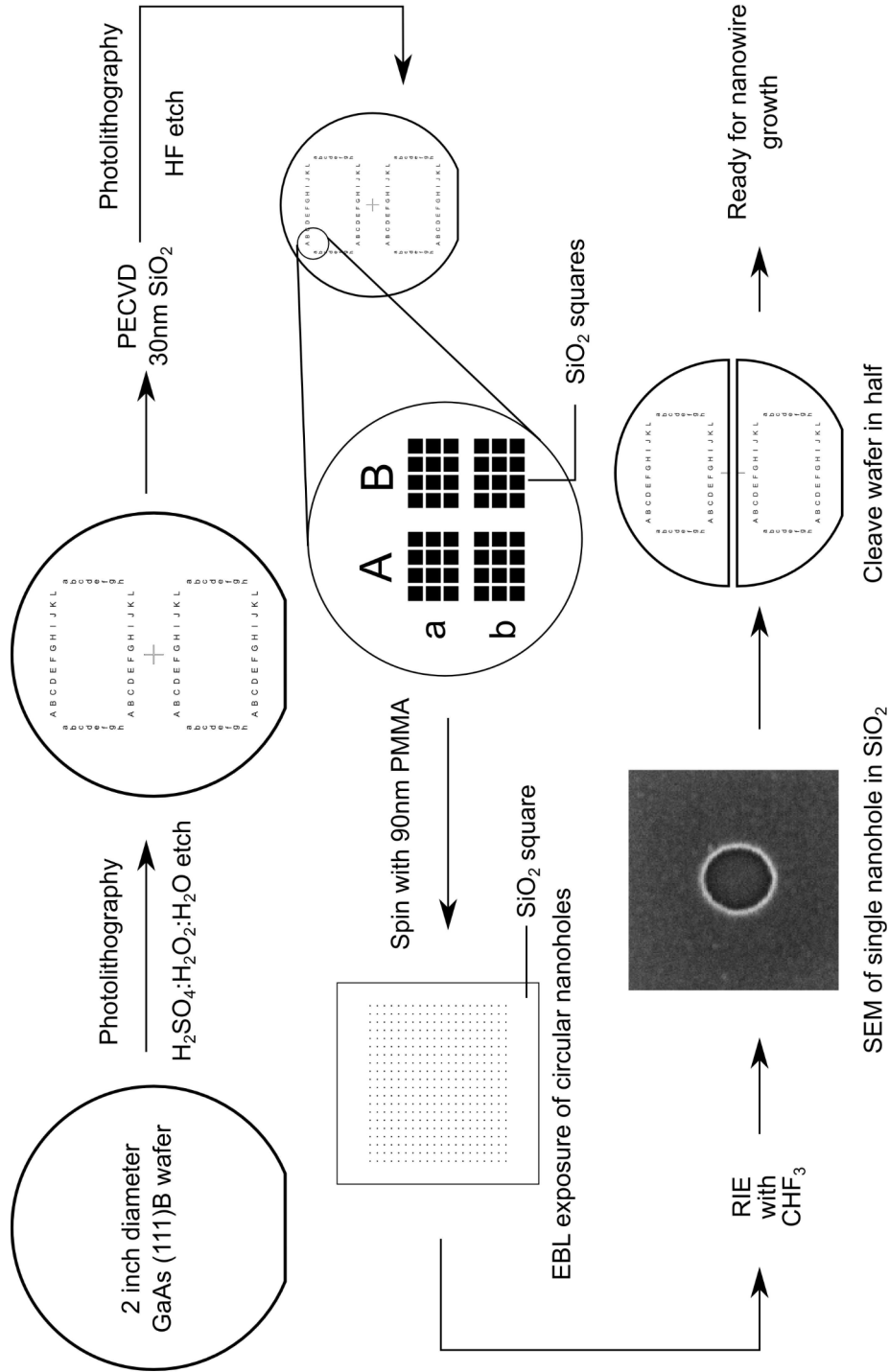


Figure 3.2. Overview of fabrication procedure prior to growth of GaAs nanowires. For full details see text. PECVD – plasma enhanced chemical vapour deposition; EBL – electron beam lithography; RIE – reactive ion etching; SEM – scanning electron microscopy.

3.3 Fabrication prior to MOCVD growth

3.3.1 Step 1: Marker development

The first fabrication step involved the patterning and etching of markers into a 2 inch diameter, (111)B orientated GaAs wafer. These markers enabled the accurate alignment of the wafer during electron beam lithography (EBL) in a later step.

The new wafer was first baked on a 100°C hotplate for 60s to evaporate any water on its surface. Then, BPRS100 optical resist was spun onto the wafer at 4000rpm for 30s, before the wafer was baked once more at 100°C for 60s to drive off the solvent within the resist. This gave a resist thickness of ~850-900nm. BPRS100 resist is sensitive to visible / UV light exposure and is commonly used during photolithography. The resist was exposed to either 300nm or 400nm wavelength light through an optical mask* for either 2s or 10s respectively. To improve the fidelity of the transferred pattern, the procedure could be undertaken using a vacuum between the lithography mask and the GaAs wafer. This decreased the spacing between the mask and wafer thereby reducing the impact of diffraction on feature edges (i.e. it produced sharper features). When this was the case, the exposure time was typically increased by a factor of ~50%.

The exposed wafer was then developed for 60s at room temperature in a 3:1 H₂O:PLSI solution before rinsing in deionised water (DIW) and drying with a nitrogen gun. After ashing the wafer in an oxygen plasma for 15s to remove any remaining resist in the exposed areas, the mask pattern was transferred into the GaAs substrate using a 1:8:80 H₂SO₄:H₂O₂:H₂O etch solution. The starting concentrations used were 30% (98%) H₂O₂ (H₂SO₄). The etch process was undertaken at room temperature for 60s leading to an

* "Nanowires-dark-field" mask, fabricated by Compugraphics

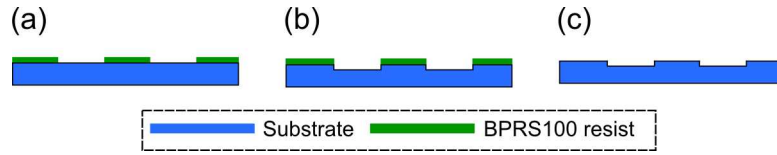


Figure 3.3. Process steps for etching markers into a GaAs substrate. (a) Pattern is developed in BPRS100 photoresist using optical lithography; (b) Pattern is transferred through to the substrate using an acid etchant; (c) BPRS100 resist is removed.

etched marker depth of $\sim 500\text{nm}$. The etch depth was confirmed by measuring the depth of an etched feature using a Dektak surface profilometer. Where necessary, an additional 30s etch was used to ensure the markers were of sufficient depth. The remaining BPRS100 was then removed using a warm organic solvent (EKC3830, Dow Chemical) followed by rinsing of the wafer under running DIW and drying with nitrogen. This process is described schematically in Figure 3.3.

3.3.2 Step 2: SiO_2 deposition

A $\sim 30\text{nm}$ thick SiO_2 dielectric film was then deposited on the GaAs substrate using plasma enhanced chemical vapour deposition (PECVD). This film acted as the growth mask to promote nanowire growth at the expense of planar growth as described in section 3.4. SiO_2 was deposited at 300°C using the gases silane (160 standard cubic centimetres per minute (sccm)) and nitrous oxide (900sccm) as sources, with nitrogen used as a ballast gas (240sccm). The RF power was 25W. To reduce the occurrence of pinholes within the dielectric, two layers of $\sim 15\text{nm}$ thickness were deposited in 15s stages, with the wafer rotated through 90° between each stage. This prevented the growth of nanowires in undesired locations by reducing the likelihood of pinhole formation within the SiO_2 film.

3.3.3 Step 3: SiO₂ square definition

Previous reports in the literature have stressed the need to reduce the coverage of the SiO₂ (or SiN_x) growth mask in order to allow better control over selective area growth by acting as a sink for adatoms¹⁶. With this in mind, the SiO₂ film was patterned into squares of side length 130µm using a combination of photolithography and wet chemical etching.

The lithography process followed a very similar procedure to that described in section 3.3.1. However, before spinning the wafer with BPRS100, an adhesion promoter, hexamethyldisilazane, was first spun on the wafer for 30s at 4000rpm. This enabled the BPRS100 to adhere to the SiO₂ film deposited in the previous step. Photolithography was then undertaken using a lithography mask[†] containing square arrays which were not exposed during the procedure (i.e. they were formed from chrome regions on the mask). To remove the SiO₂ exposed by this process, the wafer was placed in a 1% solution of hydrofluoric acid (HF) for 30s, followed by a thorough rinse in DIW and drying with nitrogen. The remaining BPRS100 was then removed using warm EKC830 followed by a DIW rinse and drying with nitrogen.

3.3.4 Step 4: Formation of nanohole arrays

Following this, after baking for 60s at 100°C, 1:2 anisole:poly(methyl methacrylate) (PMMA) electron-sensitive resist was spun onto the wafer for 30s at 4000rpm. This was followed with a post-bake at 180°C for 5 minutes to harden the resist, leading to a resist thickness of ~90nm. The wafer was then loaded into an EBL system (Raith 150). PMMA is termed a positive resist, meaning that when exposed to electrons its polymer chains are locally weakened, allowing it to be dissolved in a suitable solvent. Square arrays of

[†] “Nanowires-light-field” mask, fabricated by Compugraphics

nanoholes with a pitch of $4\mu\text{m}$ were patterned into the resist. A typical array consisted of 20 by 20 or 25 by 25 nanoholes. All nanoholes in a particular array were designed to have the same diameter, but between arrays the diameter was varied between 40nm and 250nm. This was achieved using an electron-accelerating voltage of 30kV and a $10\mu\text{m}$ aperture for the electron beam.

After EBL exposure the PMMA resist was developed in a 1:3 methyl isobutyl ketone: isopropyl alcohol solution for 30s at 23°C . This produced nanoholes within the resist in those areas previously exposed to the EBL electron beam. The wafer was then ashed in an oxygen plasma for 15s to remove any resist from the exposed areas. This time was kept deliberately short to prevent complete removal of the unexposed resist, and to ensure the patterned nanoholes did not increase significantly in diameter.

To transfer the nanoholes into the SiO_2 film, the RIE technique was employed. The wafer was dry etched at room temperature using a 40sccm flow of CHF_3 , RF power of 80W and chamber pressure of 25mT. The process time was 3 minutes 30 seconds. The remaining PMMA was removed from the wafer using warm EKC830 and DIW, following which the wafer was cleaved in half parallel to the major flat. Scanning electron microscope (SEM) imaging was used to ascertain that the nanoholes had etched through the SiO_2 film, and to measure their diameter. Whilst such imaging did not guarantee that the nanoholes had etched completely through to the GaAs substrate as required, it was generally observed that a clear contrast difference between the nanohole and the surrounding SiO_2 led to successful nanowire growth from that nanohole. An example SEM of a nanohole formed in this manner is shown in Figure 3.2. After a final cleaning step using EKC830, the wafer was loaded into the MOCVD reactor.

3.4 Growth of GaAs nanowires

GaAs nanowire growth was carried out using a horizontal flow MR350 MOCVD reactor in the EPSRC National Centre for III-V Technologies at the University of Sheffield[‡]. The reactor was used for a variety of other projects, both internal to the University and for external customers, and was therefore not dedicated solely to nanowire growth. The reactor was based on a tube furnace design, shown schematically in Figure 3.4.

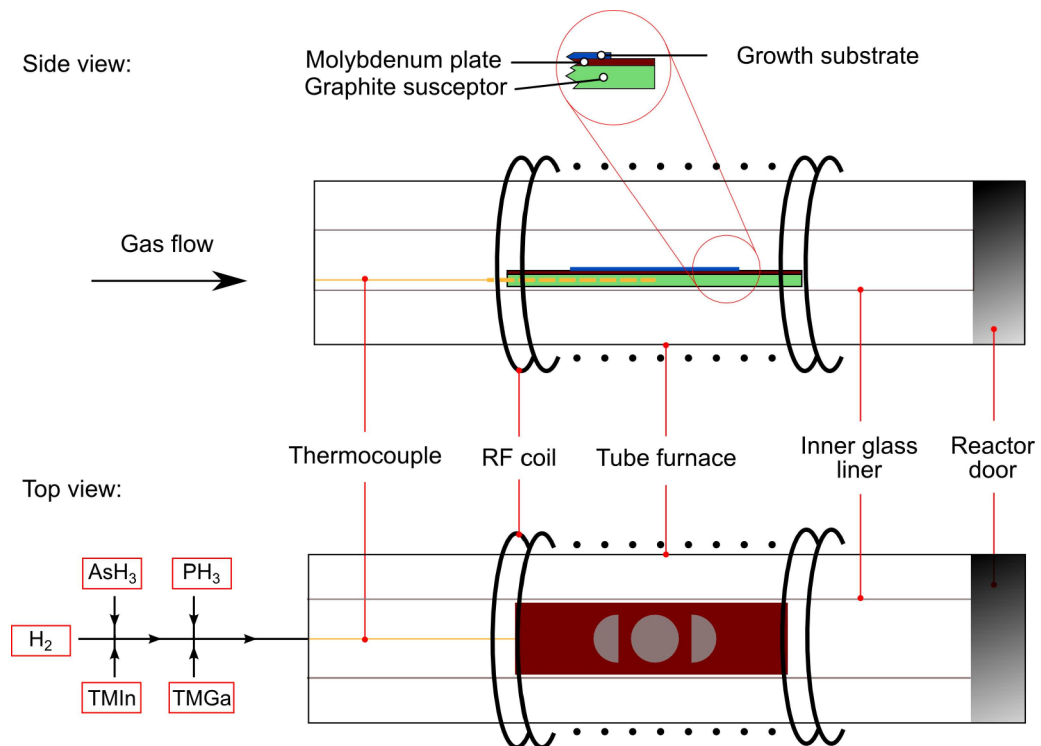


Figure 3.4. Schematic overview of MR350 MOCVD reactor. H₂ carrier gas flows from left to right. The reactor could accommodate up to four halves of a two inch substrate in locations shown in the ‘top view’ schematic.

[‡] Nanowire growth was undertaken by the author and Andrey Krysa

The substrate was placed on a molybdenum plate on top of a stationary graphite susceptor block, which was heated via an RF-generating coil. The temperature of the graphite susceptor was measured using a thermocouple inserted into the centre of the susceptor. It is therefore important to note that this only gave an estimate of the temperature at the substrate surface, as this was likely to be different to the thermocouple reading. The reactor used hydrogen (H_2) as its carrier gas. For the growth of nanowires, the reactor was equipped with trimethylgallium (TMGa), trimethylindium (TMIn), arsine (AsH_3) and phosphine (PH_3) sources. It should be noted that halfway through each growth run TMIn was introduced into the reactor for 2s, in an attempt to form a single quantum dot within each nanowire. The study of nanowire quantum dots is left to Chapters 3-5, and the growth is not thought to impact on the results presented in this Chapter, where the focus is on the GaAs nanowire growth itself.

When TMGa and AsH_3 were introduced into the reactor, each nanohole within the SiO_2 growth mask acted as a nucleation site for the deposition of adatoms, whilst growth on the SiO_2 mask was typically suppressed. The minimum diameter of a nanowire produced using this technique was approximately equal to (and never smaller than) the diameter of the nanohole from which it nucleated. This is in contrast to similar growth by MBE where the initial diameter of the nanowire may be smaller than the size of the nanohole¹⁷. After the initial formation of pyramidal islands¹⁸, nanowire growth proceeds due to the variable growth rates on different crystal facets. Given suitable precursor flows, substrate temperature and reactor pressure, growth on the six $\{110\}$ crystal planes orthogonal to the sample surface is inhibited, whilst growth on the (111)B plane is able to take place. The result is the formation of a pillar with a hexagonal cross-section and a (111)B growth front parallel to the substrate. An example SEM of a GaAs nanowire is shown in Figure

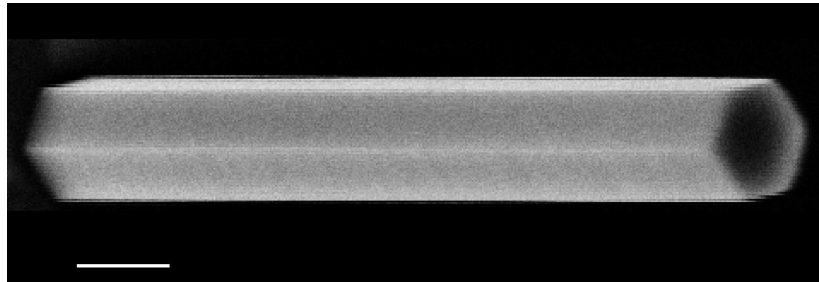


Figure 3.5. Scanning electron microscope image of a GaAs nanowire. Scale bar 200nm. Note the growth substrate is to the left of the image, orientated vertically.

3.5. In the case of GaAs, the substrate chosen is orientated in the (111)B direction, meaning the growth front of a fully formed nanowire is also a (111)B crystal plane. As will be discussed in Chapter 6, the preferential growth direction for nanowires in other material systems can be in other directions.

All growth discussed herein was undertaken at a pressure of 150 Torr. Prior to growth, the substrate was annealed by increasing the temperature from 20°C to 780°C over the course of 9 minutes. The intention of this process was to remove the native oxide from the substrate, as well as potentially remove any remaining carbon contamination introduced during the previous processing steps. During this time, an AsH₃ overpressure was maintained using a flow rate of 30 sccm, introduced along with the H₂ carrier gas (at 18,000sccm) to prevent desorption of arsenic from the substrate surface. The ramp time meant that the substrate experienced these conditions at 780°C for approximately 3 minutes. The temperature was then lowered to the desired growth temperature, whilst maintaining the AsH₃ overpressure. Typically this was 750°C.

Growth was undertaken using TMGa as the gallium source and AsH₃ as the arsenic source. The nanowires were nominally undoped, although low background carbon doping from the reactor was almost inevitable. From the literature, it was expected that nanowires with a hexagonal cross-section, and with an inverse relationship between diameter and height, would be grown, given optimised flow rates for TMGa and AsH₃. However, two different growth modes were actually observed, which were dependent on the treatment of the substrate in the fabrication steps described previously in this chapter. These are described separately in the following.

3.4.1 Nanowire growth in the presence of rough planar surface growth

This section details a growth study undertaken for GaAs nanowires. For each sample the growth on areas of the substrate not covered by the SiO₂ growth mask (excluding the patterned nanoholes) showed significant surface roughness, giving rise to a matte appearance of the wafer. A representative scanning electron microscope (SEM) image of such rough planar growth is shown in Figure 3.6. The rough planar growth had a noticeable effect on the nanowire growth characteristics as discussed later.

An overview of the samples grown in this study is given in Table 3.1. To investigate correct source flow rates, the first two samples (3A and 3B) were grown using TMGa and AsH₃ flows of 66 (33) and 30 (15) sccm respectively. Growth was undertaken at 750°C for 30 minutes. In an attempt to provide a degree of surface passivation of the nanowire sidewalls, a PH₃ flow of 300sccm was introduced at the end of the growth run as the sample was cooling down. Intermixing of arsenic and phosphorus atoms was expected to produce a thin GaAsP layer on the surface of the nanowire. A GaAsP capping layer has

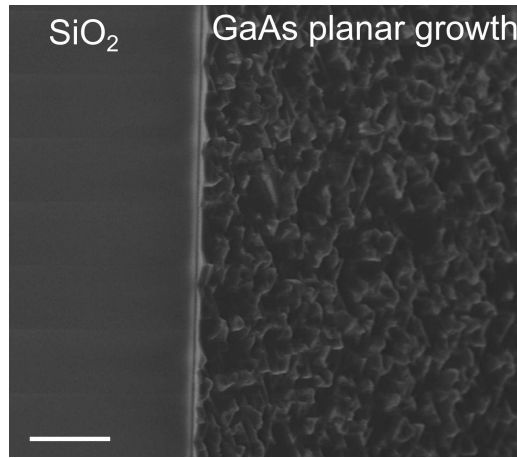


Figure 3.6. SEM image revealing rough planar growth on the exposed GaAs substrate (right hand side), whilst regions covered in SiO₂ show no GaAs overgrowth (left hand side). Scale bar 5 μ m.

Reference in text	Sample MR No.	NW core source flows (sccm)		NW core growth time (s)	NW shell source flows (sccm)			NW shell growth time (s)	Axial growth rate ($\text{\AA}/\text{s}$)
		TMGa	AsH ₃		TMGa	AsH ₃	PH ₃		
3A	3197	66	30	1800	-	-	300	-	6.56
3B	3199	33	15	1800	-	-	300	-	4.22
3C	3215	66	30	1980	33	150	300	30	6.87
3D	3216	33	15	1980	33	150	300	30	3.99
3E	3227	33	7.5	1980	-	-	300	-	4.34
3F	3261	33	7.5	3180	33	7.5	300	15	3.33

Table 3.1. Summary of growth conditions for Samples 3A–3F. All samples were first annealed for 9 minutes at 780°C under an AsH₃ overpressure. This includes the time taken to reach the annealing temperature from room temperature.

been shown to improve the optical properties of GaAs nanowires¹⁹. The growth runs were then repeated in an identical manner except for the attempted growth of a radial GaAsP shell around the GaAs nanowire core (Samples 3C and 3D). There are many reports in the literature on the formation of core-shell nanowire structures, where a nanowire of one material is grown and then clad in the radial direction with another material. Appealing

aspects of such a structure include superior passivation of the surface of the original (core) nanowire, and the potential for formation of nanowire lasers^{13,20}.

An SEM image of a single nanowire from Sample 3A is shown in Figure 3.7(a). This SEM was indicative of the nanowires on Sample 3B also. The nanowire is untapered and

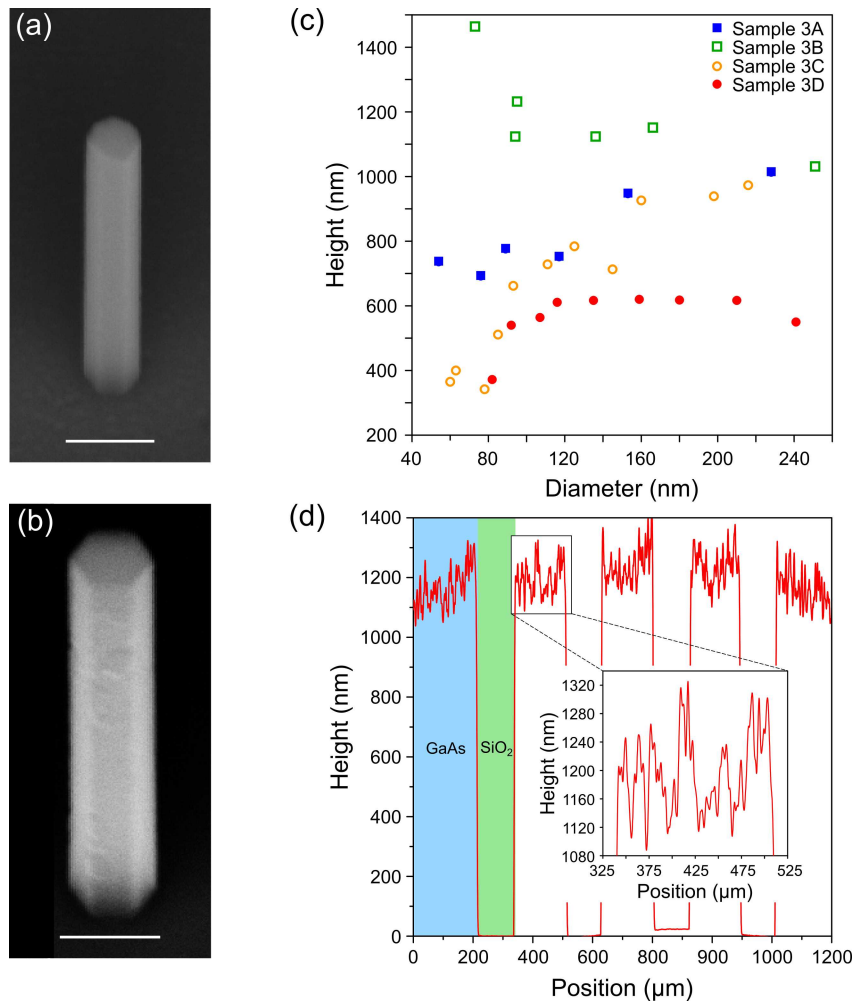


Figure 3.7. Characterisation of Samples 3A–3D. 45° tilted SEM image of a nanowire from (a) Sample 3A and (b) Sample 3C. Scale bars 200nm; (c) Height versus diameter for the nanowires on each sample; (d) Surface profile of GaAs wafer after growth. Blue area and equivalent areas to the right shows profile on the GaAs substrate. Green area and equivalent areas to the right shows profile on the SiO₂ growth mask. (Inset) Zoom in on surface profile on the GaAs substrate, showing the significant variation in planar growth thickness.

has a hexagonal cross-section, seen most clearly at the nanowire base. The growth conditions were such that radial growth was strongly suppressed. The diameter of the nanowire is $\sim 117\text{nm}$, whilst the initial nanohole in the SiO_2 growth mask was $\sim 108\text{nm}$ in diameter. However, unlike in previous reports in the literature, the height of the nanowires was seen to increase with the opening diameter of the nanohole in the growth mask (and therefore the nanowire diameter).

Figure 3.7(b) shows an SEM image of a nanowire from Sample 3C (also very similar to those from Sample 3D). Whereas the nanowire sidewalls were smooth for Samples 3A and 3B, some of the nanowires on Samples 3C and 3D exhibited roughened side facets. It is thought that this may have been due to lattice mismatch between the GaAs nanowire and the GaAsP that was intended to be overgrown in the radial direction, although the origin of variability between nanowires is unclear.

Figure 3.7(c) shows the height-diameter dependencies for Samples 3A–3D. Note that the radial capping layer effectively shifts the plots for Samples 3C and 3D slightly to the right by increasing the diameter. Given the similarity in growth conditions for Samples 3A and 3C, and Samples 3B and 3D, there were unexpected differences between the samples. Whilst the height was approximately proportional to the diameter for Samples 3A, 3C and 3D, there was an inverse relationship for Sample 3B. In fact, the latter is quite commonly observed for catalyst-free growth of GaAs nanowires²¹. For the nanowires without a GaAsP shell, reducing the source flow rates of TMGa and AsH_3 actually increased the vertical growth rate without having a noticeable influence on the radial growth. However in the case of the nanowires which did have a GaAsP shell, the opposite effect was seen on the nanowire height. Furthermore in the case of Sample 3D there was very little influence of the nanohole diameter on the resulting nanowire height.

The variation in nanowire height and diameter between samples was a cause for concern as it impacted on sample to sample uniformity. For all of the samples, planar growth away from the SiO₂ growth mask was seen to be extremely rough. High growth rates over 6.5Å/s and ~4Å/s were observed for the high source flow and low source flow samples respectively. The reduction in growth rate was expected as the source flow rates were reduced. Figure 3.7(d) shows Dektak surface profile measurements taken for Sample 3A, highlighting the significant variation observed in the planar growth thickness as a function of position on the substrate. The Dektak tip was moved in a straight line over the sample surface, during which it passed over four unpatterned SiO₂ squares. These are the regions with a height of ~0nm in Figure 3.7(d) (one of which is highlighted in green), whilst the large variation in height between these regions is due to GaAs surface growth. The variation resulted in a high planar growth rate which appeared to be responsible for the unusual height-diameter dependence of the nanowires. This becomes clear in section 3.4.3.

Finally, two samples were grown with the aim of increasing the nanowire height, particularly for narrow nanowires. The first sample was grown with the same conditions as Sample 3B but using half the AsH₃ flow rate (Sample 3E). This was motivated by the possible formation of stable arsenic trimers on the GaAs substrate surface in the presence of excess AsH₃. AsH₃ trimers have been suggested to result in slow nanowire seeding and growth²². The second sample (Sample 3F) was simply grown for a significantly longer time (53 minutes).

For Sample 3E, the influence on the nanowire height was not as anticipated, suggesting that AsH₃ trimer formation was not an issue under those growth conditions. Figure 3.8 shows the height-diameter dependence for this sample. Whilst the height of the largest

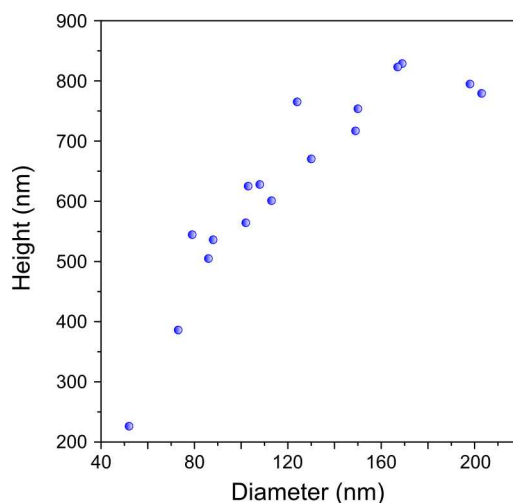


Figure 3.8. Height versus diameter for the nanowires grown on Sample 3E.

diameter nanowires was similar to those of Sample 3B, narrower diameter nanowires were once more shorter than larger diameter nanowires. The rough planar growth rate was similar however, at $4.34\text{\AA}/\text{s}$. It could be seen therefore that reducing the AsH_3 flow rate in this case simply acted to decrease the nanowire growth rate, with little influence on planar growth.

The results of the growth of Sample 3F provided the final motivation to address the issue of sample repeatability. The nanowires on this sample were extremely short and had not attained the expected hexagonal faceting, instead forming amorphous columns. The rough planar growth rate was significantly different to that for Sample 3E, at $3.33\text{\AA}/\text{s}$. The extremely low growth rate measured for Sample 3F could have been due to delayed seeding of the nanowires due to residual SiO_2 remaining within the nanoholes in the growth ask. This is addressed in Chapter 4. However, the general variability between samples was thought likely to be due to the roughness of the surface growth, with the

morphology of the resulting surface seen to vary from sample to sample. To improve the reproducibility of nanowire samples, significant efforts were first made to reduce the surface roughness of planar GaAs epitaxy.

3.4.2 Achieving low surface roughness planar epitaxy on (111)B GaAs

During the fabrication steps prior to growth, EKC830 photoresist stripper was found to be particularly efficacious in removing both optically active (BPRS100) and electron beam sensitive (PMMA) resists. This was therefore used extensively to ensure the cleanliness of the wafers prior to growth. After advice that this chemical was known to slowly etch GaAs, the fabrication procedure was altered as a roughened surface was the possible origin of rough planar growth. From this point on, all sample cleaning processes were undertaken for a maximum duration of 5 minutes. After each use of EKC830, the wafer was rinsed in streaming DIW for 5 minutes. A minimum cleaning time of ~3 minutes was found to be necessary to achieve sufficient sample cleanliness. By reducing the duration for which the substrate was exposed to an apparently slow etchant (EKC830), it was expected that the surface roughness prior to growth would be reduced.

Additional steps were undertaken to promote sample reproducibility. It was ensured that the glassware used in the MR350 reactor for nanowire growth was the same for all samples. This was to prevent possible variations in carrier gas flow between different sets of glassware. Prior to each growth run, the reactor was conditioned. This involved undertaking a short GaAs growth run without a substrate loaded into the reactor. This coated the walls of the liner with GaAs, thus presenting the same surface to the carrier gas for each growth run.

With the changes described above, a marked improvement was observed in the quality of

planar GaAs epitaxy, which translated into more consistent nanowire growth. GaAs nanowire growth proceeding from samples fabricated in this manner is the subject of the following section.

3.4.3 Nanowire growth in the presence of smooth planar surface growth

The growth conditions used for the samples in this section are shown in Table 3.2. The first sample grown after the alterations discussed in section 3.4.2 (Sample 3G) utilised the same growth conditions as for Sample 3F with the exception of a GaAsP shell.

The most significant outcome of this growth was the observation of planar GaAs growth away from the nanowires which exhibited low surface roughness. This is shown in Figure 3.9(a). The contrast with the rough planar growth seen previously and highlighted in Figure 3.6 is obvious. Indeed, every GaAs nanowire sample grown after the alterations to the fabrication procedure exhibited smooth surface growth. The change in morphology of the planar surface was accompanied by a ~50% reduction in the planar growth rate, as

Reference in text	Sample MR No.	NW core source flows (sccm)		NW core growth time (s)	NW shell source flows (sccm)			NW shell growth time (s)	Axial growth rate ($\text{\AA}/\text{s}$)
		TMGa	AsH ₃		TMGa	AsH ₃	PH ₃		
3G	3308	33	7.5	2940	-	-	300	-	2.07
3H	3329	33	30	600	33	150	300	10	1.08
3I	3352	33	15	600	33	150	300	10	1.67

Table 3.2. Summary of growth conditions for Samples 3G–3I. All samples were first annealed for 9 minutes at 780°C under an AsH₃ overpressure. This includes the time taken to reach the annealing temperature from room temperature.

shown in Table 3.2. It is hypothesized that the effective adatom flows for nanowire growth were thus higher in this case.

However, the nanowire growth itself on Sample 3G was less successful, as can be seen in a representative SEM in Figure 3.9(b). The nanowire axial growth rate was low at $\sim 0.75\text{nm/s}$, largely independent of the nanowire diameter (Figure 3.9(c)). It was observed that the nanowires, whilst hexagonal as before, had developed rough facets. It was unclear whether the surface roughness developed during the growth of the nanowires or if it was the result of decomposition of the surface during cooling of the sample under a PH_3 overpressure.

In order to deduce the possible influence of AsH_3 flow rate on the nanowire morphology, a second growth run was undertaken with a higher AsH_3 flow rate of 30sccm

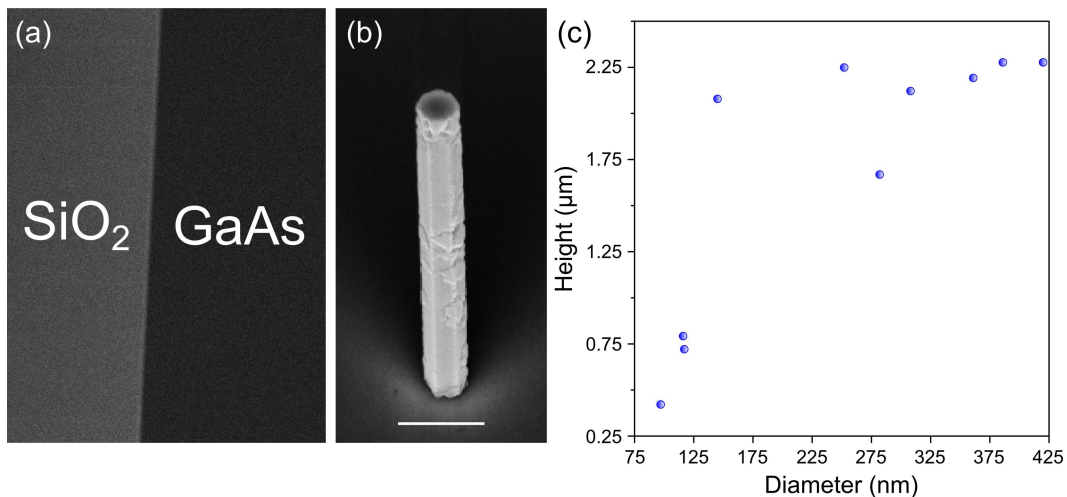


Figure 3.9. Characterisation of Sample 3G. (a) SEM image of substrate after growth showing the SiO_2 growth mask (left) and smooth GaAs planar growth (right); (b) Representative nanowire from the sample. Scale bar 500nm; (c) Height versus diameter for the nanowires grown on Sample 3G.

(Sample 3H). To counter a possible increase in growth rate, the growth time was reduced to 10 minutes. The resulting nanowires exhibited a uniform morphology and the planar surface growth was smooth once more. The nanowire height versus diameter showed an inverse trend as is often observed for catalyst-free growth of nanowires (Figure 3.10). The axial growth rate was much increased relative to Sample 3G, with a maximum of $\sim 9\text{nm/s}$ for $\sim 60\text{nm}$ diameter nanowires. However, a degree of radial growth was observed alongside the axial growth, also shown in Figure 3.10. The radial growth increased in a linear relationship with increasing nanowire diameter. In the literature, radial growth is often attributed to a high V/III ratio, suggesting the AsH_3 flow was too high to achieve purely axial growth. A third sample was thus grown using an intermediate AsH_3 flow rate of 15sccm (Sample 3I - all other conditions as for Sample 3H). Whilst this did indeed appear to reduce the extent of the radial growth, the analysis was complicated by an apparent delay in seeding of some of the nanowires, resulting in non-uniform heights

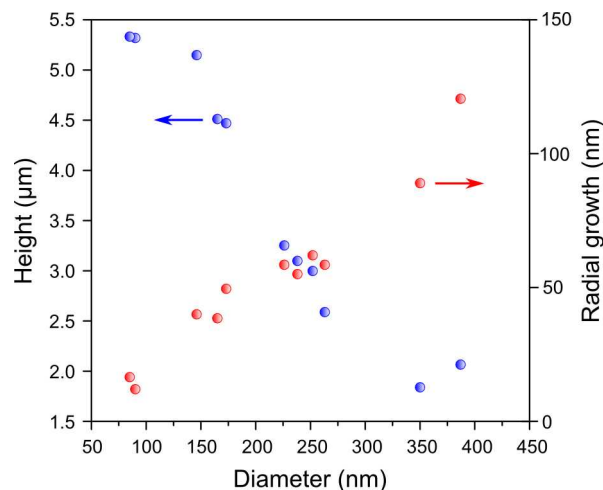


Figure 3.10. Height and radial growth versus diameter for the nanowires grown on Sample 3H.

across the array. This was later found to be the result of incomplete removal of the SiO_2 from within each nanohole, as discussed in Chapter 4. However, the range of AsH_3 flows which could be used to obtain vertical, untapered nanowires with smooth side facets had been deduced by this point. The growth was next extended to include an InGaAs nanowire quantum dot within each nanowire, the subject of the following chapter.

3.5 Conclusion

The fabrication and growth of GaAs nanowires has been described. Two growth modes were observed, dependent on the surface roughness of planar GaAs growth in regions not covered by the SiO_2 growth mask. In the case of rough planar growth, nanowires typically grew with a direct relationship between their diameter and height. This is in contrast to most reports in the literature. However, the planar growth rate was found to be variable and fairly high ($>3\text{\AA}/\text{s}$), influencing the nanowire growth rate and resulting in inconsistencies between samples. By making alterations to the fabrication and growth procedures, smooth planar growth with a lower growth rate ($< 2\text{\AA}/\text{s}$) was achieved. This resulted in nanowire growth with the expected height-diameter characteristics. Tailoring the AsH_3 flow rate was found to influence the nanowire morphology. High AsH_3 flow rates resulted in radial nanowire growth, whilst very low AsH_3 flow resulted in nanowires with a degraded appearance, possibly due to excess arsenic desorption during growth or cooling of the sample. Reducing the V/III ratio by choosing an AsH_3 flow rate lying between the cases discussed above resulted in reduced radial growth, as reported previously in the literature.

Bibliography

- (1) Wagner, R. S.; Ellis, W. C. *Appl. Phys. Lett.* **1964**, *4*, 89.
- (2) Plissard, S.; Larrieu, G.; Wallart, X.; Caroff, P. *Nanotechnology* **2011**, *22*, 275602.
- (3) Inari, M.; Takeda, J.; Motohisa, J.; Fukui, T. *Phys. E Low-dimensional Syst. Nanostructures* **2004**, *21*, 620–624.
- (4) Perea, D. E.; Allen, J. E.; May, S. J.; Wessels, B. W.; Seidman, D. N.; Lauhon, L. *J. Nano Lett.* **2006**, *6*, 181–5.
- (5) Paladugu, M.; Zou, J.; Guo, Y.-N.; Zhang, X.; Kim, Y.; Joyce, H. J.; Gao, Q.; Tan, H. H.; Jagadish, C. *Appl. Phys. Lett.* **2008**, *93*, 101911.
- (6) Dick, K. A.; Bolinsson, J.; Borg, B. M.; Johansson, J. *Nano Lett.* **2012**, *12*, 3200–3206.
- (7) Shapiro, J. N.; Lin, A.; Wong, P. S.; Scofield, A. C.; Tu, C.; Senanayake, P. N.; Mariani, G.; Liang, B. L.; Huffaker, D. L. *Appl. Phys. Lett.* **2010**, *97*, 243102.
- (8) Yang, L.; Motohisa, J.; Takeda, J.; Tomioka, K.; Fukui, T. *Appl. Phys. Lett.* **2006**, *89*, 203110.
- (9) Tatebayashi, J.; Ota, Y.; Ishida, S.; Nishioka, M.; Iwamoto, S.; Arakawa, Y. *Appl. Phys. Lett.* **2012**, *100*, 263101.
- (10) Noborisaka, J.; Motohisa, J.; Hara, S.; Fukui, T. *Appl. Phys. Lett.* **2005**, *87*, 093109.
- (11) Minot, E. D.; Kelkensberg, F.; van Kouwen, M.; van Dam, J. A.; Kouwenhoven, L. P.; Zwiller, V.; Borgström, M. T.; Wunnicke, O.; Verheijen, M. A.; Bakkers, E. P. A. M. *Nano Lett.* **2007**, *7*, 367–71.
- (12) Mariani, G.; Wong, P.-S.; Katzenmeyer, A. M.; Léonard, F.; Shapiro, J.; Huffaker, D. L. *Nano Lett.* **2011**, *11*, 2490–4.
- (13) Hua, B.; Motohisa, J.; Kobayashi, Y.; Hara, S.; Fukui, T. *Nano Lett.* **2009**, *9*, 1–5.
- (14) Akabori, M.; Takeda, J.; Motohisa, J.; Fukui, T. *Nanotechnology* **2003**, *14*, 1071–1074.
- (15) Sato, T.; Motohisa, J.; Noborisaka, J.; Hara, S.; Fukui, T. *J. Cryst. Growth* **2008**, *310*, 2359–2364.

-
- (16) Kumakura, K.; Nakakoshi, K.; Kishida, M.; Motohisa, J.; Fukui, T.; Hasegawa, H. *J. Cryst. Growth* **1994**, *145*, 308–313.
- (17) Hertenberg, S.; Rudolph, D.; Bichler, M.; Finley, J. J.; Abstreiter, G.; Koblmüller, G. *J. Appl. Phys.* **2010**, *108*, 114316.
- (18) Ikejiri, K.; Sato, T.; Yoshida, H.; Hiruma, K.; Motohisa, J.; Hara, S.; Fukui, T. *Nanotechnology* **2008**, *19*, 265604.
- (19) Couto, O. D. D.; Sercombe, D.; Puebla, J.; Otubo, L.; Luxmoore, I. J.; Sich, M.; Elliott, T. J.; Chekhovich, E. A.; Wilson, L. R.; Skolnick, M. S.; Liu, H. Y.; Tartakovskii, A. I. *Nano Lett.* **2012**, *12*, 5269–74.
- (20) Chen, R.; Tran, T. D.; Ng, K. W.; Ko, W. S.; Chuang, L. C.; Sedgwick, F. G.; Chang-Hasnain, C. *Nat. Photonics* **2011**, *5*, 170–175.
- (21) Noborisaka, J.; Motohisa, J.; Fukui, T. *Appl. Phys. Lett.* **2005**, *86*, 213102.
- (22) Ikejiri, K.; Noborisaka, J.; Hara, S.; Motohisa, J.; Fukui, T. *J. Cryst. Growth* **2007**, *298*, 616–619.

4 InGaAs nanowire quantum dots

4.1 Introduction

Many exciting developments in the field of solid state artificial atoms have been reported since the first demonstration of excitonic photon emission from a QD grown by the Stranski-Krastanow (SK) technique¹. These include the demonstration of single photon emission²; coherent control of single electron spins³; observation of electron spin resonance⁴; and quantum entanglement of emitted photons^{5,6}. QDs grown by the SK technique have been electrically contacted allowing for control of the charge state of the QD⁷ as well as electrical triggering of single photon emission⁸. Resonance fluorescence measurements on QDs have also been demonstrated⁹, with the potential for emission of single photons with long coherence times. Solid state cavity quantum electrodynamics measurements have been enabled through strong coupling of the QD exciton to the light field of a photonic crystal cavity¹⁰. Such coupling allows a strong Purcell effect to be observed.

As the field of solid state QD research has developed a major limitation of SK QD growth has become evident. Due to the random nature of the growth process, the resulting QDs have a random distribution in both size and location. For individual QD study this issue is often unimportant as a single QD can usually be isolated within a mesa structure, and a systematic search can be made for a QD with the desired characteristics for a particular measurement (exciton energy, intensity etc.). However, in many cases it would be advantageous to have precise control over both the location and energy states of the QD.

For instance, strong coupling between the QD energy states and photons in a photonic crystal cavity is dependent on precise positioning of the QD at an antinode of the cavity electric field, as well as spectral overlap of the ground state with a cavity mode¹¹. Presently such alignment is achieved in a random fashion by fabricating and measuring multiple devices to find one with the desired properties. Such an approach is incompatible with scale up, which is required for instance by solid state implementations of quantum information protocols¹². Given this challenge, much recent research has focussed on alternative QD growth techniques, in particular those offering the possibility of QD site control.

In section 4.2 research into site controlled growth of QDs is discussed, and nanowires are presented as a promising means to implement this. The growth of InGaAs nanowire quantum dots (NWQDs) in GaAs nanowires is described in section 4.3, whilst optical and structural characterisation of these structures is presented in section 4.4. Finally, future research directions are proposed in section 4.5. This work entails the first detailed study of arrays of InGaAs NWQDs grown by a catalyst-free technique.

4.2 Background

4.2.1 Position controlled quantum dots

QD growth by SK and other similar techniques has many appealing aspects. These include the ability to control (to a certain degree) the size, shape, density and composition of the QDs through tailoring of the growth conditions. SK growth has resulted in the formation of QDs with high quality optical properties¹³, making them ideally suited for individual study. However, many current and future applications would benefit significantly from the availability of multiple, physically homogeneous QDs with known

location. The former is often required for experiments leveraging optical interactions between spatially separate QDs (e.g. two photon interference¹⁴) whilst the latter would simplify post-growth fabrication schemes, for instance photonic crystal cavities containing strongly coupled QDs. SK and similar growth techniques provide no control over the location of the QDs. Furthermore, a single SK growth run typically results in a size distribution of QDs due to the random nature of QD nucleation. The resulting variation in the ground state energy level of a QD ensemble has a characteristic energy spread of $\sim 30\text{meV}$ ¹⁵. This inhomogeneity necessitates considerable time searching for similar QDs when inter-QD interactions are of interest, and presents an insurmountable barrier to significant scale-up. These challenges have motivated research into alternative growth techniques which allow for deterministic site control of QDs.

The intuitive approach to the site control problem involves lithographic definition to force QD nucleation in predefined locations. Typically a combination of lithography and etching is used to define the desired growth pattern, before overgrowth by either MBE or MOCVD. Etching can either be undertaken into the growth substrate itself, or through a growth mask deposited on the substrate surface. Alongside position control, such techniques have the potential to provide superior uniformity in the optical properties of the resulting QDs through greater morphology control. There have been many reports of site control of SK QDs utilising lithographic definition¹⁶⁻¹⁹. A particularly successful method in this vein is the growth of InGaAs QDs in pyramidal recesses etched into a GaAs (111)B substrate. This has resulted in QDs with an exciton ensemble broadening of as little as $\sim 1\text{meV}$, as well as exciton linewidths of $\sim 100\mu\text{eV}$ ¹⁵. A similar technique has led to the growth of ordered arrays of InGaAs QDs on GaAs (100) orientated substrates²⁰, with an average exciton linewidth of $132\mu\text{eV}$, although the QD homogeneity was not

discussed in this work. Further development of this technique resulted in InGaAs QDs with an encouragingly low ensemble broadening of 14.4meV allied with a mean linewidth of $213\mu\text{eV}^{21}$, and more recently a mean linewidth of $133\mu\text{eV}^{22}$.

A common problem in position control schemes lies in etch-induced damage of the substrate surface. Etch damage can produce a defective interface which acts as a trap for fluctuating charges²³. Due to the proximity of the overgrown QD, these fluctuating charges may result in a phenomenon known as spectral diffusion (also known as spectral wandering/meandering). This is the effect whereby the time-varying electric field induced across the QD by fluctuating charges leads to a time variation of the QD energy states through the Stark effect, and thus broadening of the QD energy levels when time-averaged measurements are undertaken^{24,25}. Spectral diffusion thus masks the intrinsic properties of the QD. One result of spectral diffusion is a reduction in the coherence time for photons emitted by the QD, which is of significance for example in quantum information applications. The influence of etch damage is usually addressed by growing a buffer layer between the etched surface and the QD²³, although maintaining the pattern fidelity is a challenge with thicker (and therefore more effective) buffer layers.

As an alternative to the growth of thick buffer layers, a technique involving thermal ejection of substrate material from nanoholes patterned into a growth mask has been recently demonstrated²⁶. The precise mechanism for the thermal ejection during the pre-growth annealing step (at 800°C) is unclear as it was undertaken under an arsine overpressure which would usually be expected to maintain the surface quality. Nevertheless, exciton linewidths down to $\sim 63\mu\text{eV}$ were observed after the growth of QDs.

Whilst the methods discussed above result in QDs formed in the plane of the substrate, a markedly different approach involves QD growth within nanowires. This is the subject of the remainder of this chapter.

4.2.2 Nanowire quantum dots

Nanowires have a number of appealing properties which make them of interest for position and size control of an integrated NWQD. Deterministic control of the nanowire location (and therefore that of the NWQD) may be enabled by lithographic definition of the nanowire growth location, as described for instance in Chapter 3. Control of the NWQD dimensions is provided in the radial direction by the nanowire diameter at the time of NWQD growth, and in the axial direction by the NWQD growth time. This is in contrast to the majority of self-assembled QDs grown on planar surfaces, where the control of the QD size is a significant challenge. NWQDs grow epitaxially in a layer by layer fashion meaning that lattice mismatch of the nanowire and NWQD compounds is not a prerequisite, unlike for SK QD growth which always produces a strained QD. The structure of the nanowire provides a simple route for the fabrication of linearly aligned NWQDs, which could for instance be coupled by the photonic modes of the nanowire, or be grown sufficiently close to observe resonant inter-NWQD effects. The columnar nanowire structure is also beneficial in enhancing photonic coupling to external optics. In contrast, extraction of photons from QDs grown within planar layers is negatively influenced by total internal reflection at the upper surface of the sample. Finally, it has been demonstrated that QDs grown in the (111) direction should have suppressed fine structure splitting²⁷. This is typically not the case for self-assembled QDs grown in the (100) direction. Elimination of the fine structure splitting allows entangled photons to be emitted by the QD through the biexciton-exciton cascade.

The great majority of nanowire quantum dots (NWQDs) are formed by growing a nanowire from one semiconductor, then briefly altering the growth sources to form a small region of a different, lower bandgap semiconductor, before continuing once more with the original growth conditions. This process is described schematically in Figure 4.1. As described in Chapter 3, the physical growth process for the nanowire itself is typically either catalysed (VLS growth) or uncatalysed. In order to realise a QD within the nanowire, the nanowire diameter at the time of NWQD growth must be sufficiently small such that carriers are confined radially within the NWQD. Axial confinement is achieved by ensuring the NWQD is of the order of $\sim 1\text{--}10\text{nm}$ in height.

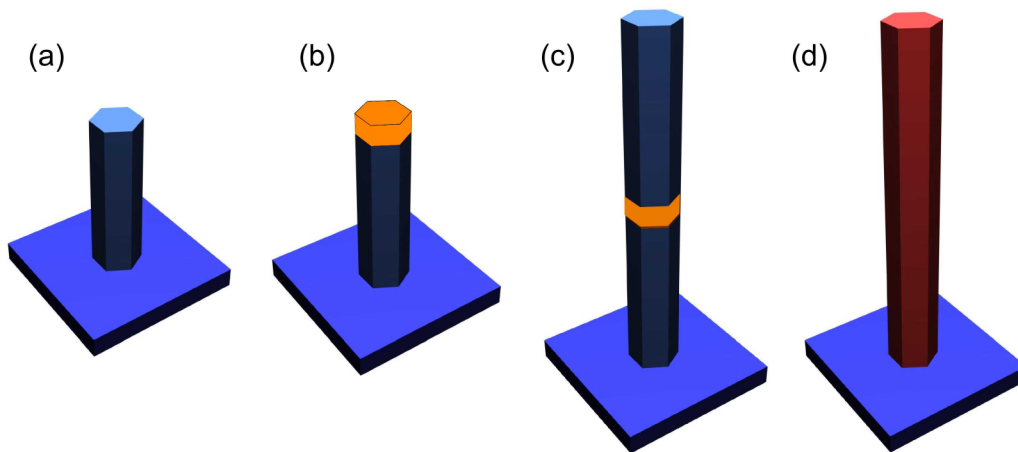


Figure 4.1. Schematic overview of the NWQD growth process. The process is largely independent of the growth technique used. (a) A nanowire is grown on a host substrate; (b) different elements are introduced into the reactor, such that a short region of the nanowire is formed from a different semiconductor to the base of the nanowire – this forms the NWQD; (c) growth of the original nanowire material is continued; (d) if desired, the nanowire may be radially capped to passivate surface states.

Growth of NWQDs has been reported in the InAsP/InP²⁸⁻³⁰, InGaAs/GaAs^{31,32}, AlGaAs/GaAs^{33,34}, GaAsP/GaP³⁵, CdSe/ZnSe³⁶ and GaN/AlN³⁷ materials systems. With regards to exciton coherence times the most promising results to date have been achieved in the InAsP/InP materials system, utilising the VLS growth mode, for which a 400ps coherence time has been measured, corresponding to an excitonic linewidth of $3\mu\text{eV}$ ³⁸. However, these reports typically focus on the properties of a few NWQDs, and often do not present data discussing the overall uniformity of the sample. They also typically consider NWQD growth in either random locations or in very close proximity³¹, with the notable exception of nanowires used by the Delft group³⁸. The former makes scale up challenging, whilst the latter leads to difficulties similar to those experienced when attempting to isolate single QDs grown by self-assembly.

Progress has been slower in regard to the growth of NWQDs in catalyst-free nanowires. Whilst axial quantum well^{39,40} heterostructures have been demonstrated, NWQD realisation has been limited to a single report in the InAsP/InP materials system²⁸ and another in the InGaAs/GaAs materials system³¹. The latter was published at the same time as this work, but does not include the detailed systematic study presented here. With respect to VLS growth, catalyst-free growth is appealing as it may lead to higher quality axial interfaces and therefore superior confinement of carriers within a NWQD. In contrast, the formation of sharp interfaces by VLS growth is often hindered by the catalyst reservoir effect. This occurs due to the time required to release adatoms from the molten catalyst (eutectic) to the growth front, and hence switching of sources to create a NWQD often leads to a graded interface^{41,42}. The notable exception to this is the InAsP/InP interface, which has been formed within NWQDs grown by the VLS technique with an abruptness on the order of a few nanometres or less⁴³. Catalyst-free growth is also inherently a position controlled growth technique unlike many reports of VLS growth, in

that a lithographical step is taken prior to growth to define locations for seeding of nanowires. This simplifies both the sample characterisation effort as well as future integration with photonic devices. It should be noted that techniques for the position control of VLS grown nanowires have also been reported, however^{30,44}. Finally, using a catalyst-free growth technique ensures that there can be no contamination of the nanowire which may result from the use of a catalyst and impact on the optoelectronic properties of the nanowire⁴⁵.

In the following sections, a detailed investigation into InGaAs NWQDs grown individually in GaAs nanowires is presented. The nanowires were grown by the catalyst-free technique, with a pitch of 4 microns allowing each NWQD to be individually addressed in a photoluminescence (PL) setup. This represents the first array-scale demonstration of a uniform sample of NWQDs, and is thus an important step towards the utilisation of NWQDs in systems requiring significant scale up. Note that some of the results presented in the following have been published elsewhere⁴⁶.

4.3 MOCVD growth of InGaAs NWQDs

The optical properties of two NWQD samples (referred to as Sample 4A and Sample 4B*) are discussed in this section. The growth procedure was identical for each sample, except for a final radial capping layer for Sample 4B which will be described below. The (111)B GaAs substrates were patterned with 130 μ m SiO₂ squares forming the growth mask, as described in Chapter 3. The SiO₂ squares were each patterned with an array of 25 by 25 nanoholes with a pitch of 4 microns. The nanoholes ranged in diameter from ~80nm to ~250nm. All the nanoholes in a single array were nominally of the same diameter.

* Sample 4A and Sample 4B correspond to MR2931 and MR2932 respectively.

As previously, nanowire growth was undertaken by low pressure MOCVD at 750°C. Flow rates of 33sccm for TMGa and 30sccm for AsH₃ were utilised. Unlike for the samples discussed in Chapter 3, a single dilution channel was used for AsH₃. However, this channel was controlled by a 500sccm mass flow controller. Accordingly, the accuracy of the measured flow rate is uncertain, and may account for the slight differences in resulting nanowire heights and diameters when compared with Sample 3I, which was grown with the same AsH₃ flow rate but using a more accurate double dilution channel.

The substrates were first annealed for 9 minutes under an AsH₃ overpressure, during which the temperature was increased to 780°C. The temperature was then lowered to the growth temperature of 750°C whilst maintaining the AsH₃ overpressure. After 5 minutes of GaAs growth, TMIn was introduced into the reactor for 2s to form an InGaAs NWQD. TMIn is a solid source, and unlike (ideal) liquid sources the concentration of indium for a given carrier gas flow rate may vary with time. The result is that to achieve a specific measured concentration of TMIn, the H₂ carrier gas flow through the TMIn source bubbler must be varied between growth runs. For these growth runs, the measured concentration of TMIn was 0.012% in a total H₂ flow of 500 sccm. This was estimated to produce an InGaAs NWQD with a ~15% indium fraction, based on growth outcomes for InGaAs QWs grown with the MR350 MOVPE reactor.

The nanowire core growth was completed by switching off the TMIn source and continuing the growth of GaAs for a further 5 minutes, using the same flow rates as for the first GaAs section of the nanowires. Finally, PH₃ was introduced into the reactor in an attempt to passivate the dangling bonds on the surface of the nanowire. For Sample 4A the sample was simply cooled under a PH₃ overpressure of 300sccm, with all other sources turned off. In so doing, it was hypothesized that a degree of arsenic/phosphorous

exchange would occur at the surface of the nanowire, leading to surface passivation. For Sample 4B, the formation of a radial GaAsP capping layer was attempted. A 10s growth interrupt allowed the AsH₃ flow to be increased from 30sccm to 150sccm. During this step the TMGA source was switched to vent (bypassing the substrate). Following this, PH₃ was introduced into the reactor for 10s at a flow rate of 300sccm, in combination with AsH₃ at 150sccm and TMGa at 33sccm. Finally, the sample was cooled under a PH₃ overpressure of 300sccm. Higher group V to group III ratios were typically observed to promote radial growth of GaAs and it was thought that this would be the same for GaAsP.

4.4 Results and discussion

The NWQDs were extensively characterised using a combination of structural and optical techniques. Structural characterisation provided the required information to enable a more complete understanding of the measured optical characteristics of the NWQDs, as becomes evident for instance in section 4.4.2.3.

4.4.1 Structural characterisation

4.4.1.1 Scanning electron microscopy

The nanowires were first characterised by SEM. A representative SEM image of a single array of nanowires from Sample 4A is shown in Figure 4.2(a). The success rate for narrow nanowire formation was as high as ~96%. Some variation in the height of the nanowires can be observed. It should be noted that the uniformity of following samples was improved significantly through the use of a pre-growth HF treatment step as described later. Figure 4.2(b) shows a higher magnification image of a single nanowire, revealing nanowires with a height of ~3.7 μ m and diameter of ~140nm. The nanowires

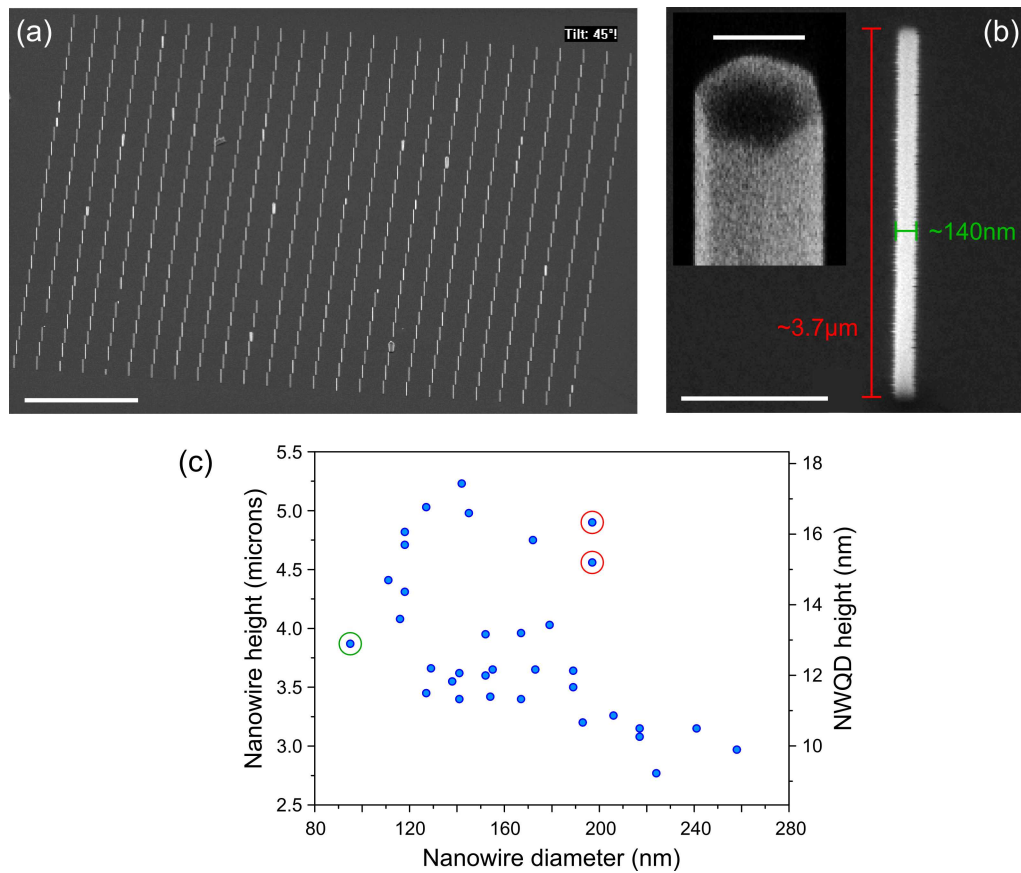


Figure 4.2. SEM analysis of the nanowires grown on Sample 4A. (a) 45° tilted overview of a single nanowire array. Scale bar 20 μm ; (b) SEM close up of the same array. Scale bar 1 μm . (Inset) Higher resolution 45° tilted SEM of a single nanowire, revealing hexagonal crystal facets. Scale bar 100nm; (c) Height versus diameter for nanowires (left y-axis) and NWQDs (right y-axis) from Sample 4A. For discussion of circled data points see main text.

grew vertically from the substrate, with no sign of tapering or bending. As discussed in Chapter 3, the nanowires had a hexagonal cross section, shown in the inset of Figure 4.2(b). Furthermore, the nanowires exhibited little radial growth. This suggested that the upper limit to the diameter of the NWQD was dictated by the diameter of the nanohole from which each nanowire grew. Any radial growth during the final GaAs growth step would have served to disguise the actual NWQD diameter.

Figure 4.2(c) summarises the height versus diameter dependence for nanowires from across the sample. As has been reported previously for catalyst-free growth of GaAs nanowires, an inverse relationship was observed between their height and diameter⁴⁷. The tallest nanowires on the sample were $\sim 5.25\mu\text{m}$ in height, with a diameter of $\sim 140\text{nm}$. Whilst the growth rate as a function of time was unknown, a linear approximation was used to estimate the height of the NWQD in the growth direction. The resulting height is plotted on the right hand axis in Figure 4.2(c).

Some deviation from the expected height–diameter dependence can be observed in Figure 4.2(c). The data points circled in red show that some nanowires had a larger height than expected. The reason for this is unclear. On the other hand, the data point circled in green is for a nanowire with a smaller height than expected. This was thought to be due to an increased seeding time for nanowires grown from smaller nanoholes within the SiO_2 growth mask. When the nanohole size was reduced below $\sim 80\text{nm}$ the nanowire heights on other similar samples were often less than expected (i.e. not following the trend observed for larger diameter nanowires, where the height increased with decreasing nanowire diameter). One possibility is that this was due to the presence of a thin layer of SiO_2 remaining within the growth mask nanohole from which this nanowire grew. This appears to be supported by the most recent growth runs (for instance the samples discussed in Chapter 5), for which exceptional nanowire uniformity was observed for arrays with nanohole sizes down to $\sim 65\text{nm}$ (the smallest patterned). This was achieved by dipping the substrate in 1% HF for $\sim 2\text{s}$ then rinsing in DIW prior to the final cleaning step before growth. The HF step appeared to remove the final remnants of SiO_2 from within the nanoholes, allowing for the immediate seeding of nanowires during growth.

An enhanced contrast between the nanohole and the SiO₂ growth mask was apparent during SEM imaging of such samples.

4.4.1.2 Transmission electron microscopy

To investigate their internal structure, transmission electron microscope (TEM) images were obtained for individual nanowires[†]. Several approaches may be considered for the isolation of individual nanowires for TEM analysis. Provided a sufficiently dense array of nanowires, the sample may be sonicated in a solvent such as isopropanol, with the resulting solution dispersed onto a standard copper TEM grid. The solvent evaporates, leaving behind a low density of nanowires which were broken from the substrate during sonication. Alternatively, a solvent allowed to flow across the surface of a nanowire sample held above and perpendicular to a horizontal TEM grid may pick up sufficient nanowires to deposit onto the grid. However, the low density of nanowires on Samples 4A and 4B, and the desire to select those with the smallest radial dimensions, made this challenging. Simply wiping the TEM grid over the surface of the nanowire sample was found to have a low success rate, with the majority of nanowires sticking to the copper grid rather than the intermediate carbon film. Eventually, some success was achieved by passing a medical scalpel across the surface of the sample which was held perpendicularly above a horizontal TEM grid.

TEM measurements were undertaken on those nanowires found at a sufficient distance from the copper supports of the TEM grid. This was required to prevent background signal from the copper affecting the image acquisition process. The TEM analysis is

[†] TEM measurements were undertaken by Dr Thomas Walther in the Department of Electronic and Electrical Engineering at the University of Sheffield.

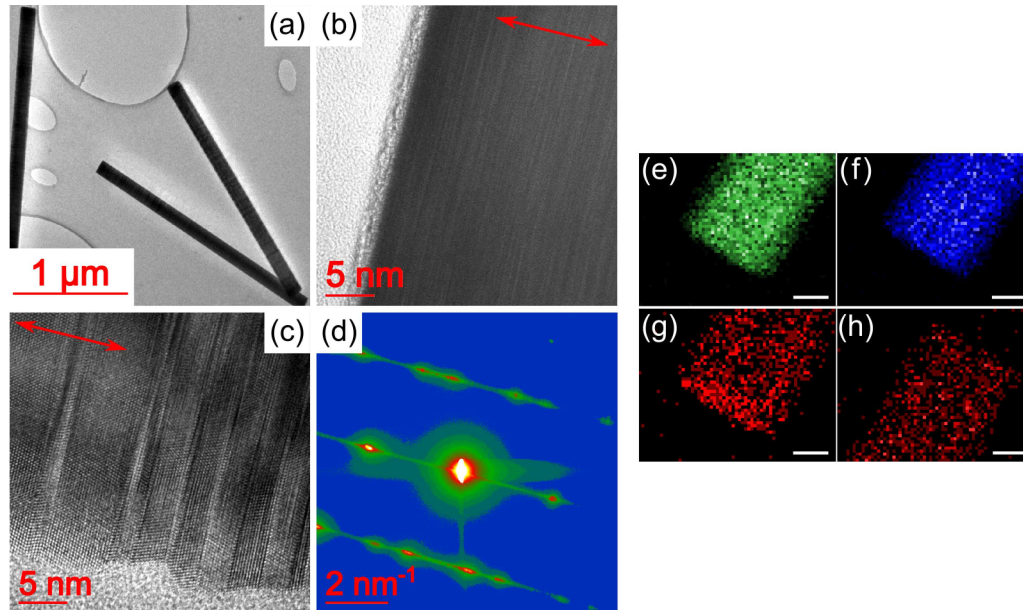


Figure 4.3. TEM analysis of nanowires containing NWQDs. (a) Low magnification bright field TEM image demonstrating the straight nature of the nanowires. The holey carbon TEM grid is visible below the nanowires; (b) Higher magnification bright field TEM image revealing the monotonically flat end facet of a nanowire, with a thin native oxide coating. The arrow shows the growth direction; (c) High magnification TEM of the sidewall of a nanowire, revealing rotational twinning perpendicular to the growth front, and associated staggered sidewall; (d) Electron diffraction pattern from a single nanowire, revealing zinc blende crystal structure with split intensity peaks due to quasi-periodic rotational twin formation; EDX spectroscopy intensity maps for the K-line X-ray of (e) gallium (f) arsenic (g-h) phosphorous at the end of a nanowire. A higher intensity signal is observed from the end of the nanowire in (g) than in (h) – this is thought to be the growth front.

summarised in Figure 4.3. The bright field overview TEM image of two nanowires in Figure 4.3(a) highlights the uniformity in diameter of the nanowires along their complete length. Figure 4.3(b) shows a higher magnification bright field image of one end of a nanowire, revealing an atomically flat end facet with a native oxide coating ~ 2.2 nm thick. It is unknown from this image whether this was the nanowire growth front, or the snapped end of the nanowire.

Figure 4.3(c) shows a high magnification TEM image revealing the internal crystal structure of a nanowire. Regions of alternating contrast can be observed perpendicular to the growth axis (given by the red arrow). At the radial edge of the nanowire, the interfaces between these regions are seen to coincide with a change in crystallographic orientation of the nanowire sidewall. Unlike in other reports concerning GaAs nanowires⁴⁸ the contrast was not due to zinc blende/wurtzite polytypism, but instead rotational twinning of a single crystalline phase perpendicular to the growth axis. Whilst the bulk zinc blende crystal usually exhibits ABCABC stacking order, at a rotational twin interface the stacking order inverts, e.g. ABCBACBA. This is due to one atomic plane of the crystal forming at 180 degrees to that of the underlying plane. The effect is to produce an interface with BCB stacking, in effect a monolayer of wurtzite crystal structure⁴⁹. Rotational twins were seen to occur with an average period of ~ 2.7 nm.

Proof that the nanowire had zinc blende crystal structure is seen in Figure 4.3(d). This electron diffraction pattern reveals intensity fringes at locations corresponding to the zinc blende crystal structure. Some of the fringes are split, and this is attributed to the quasi-periodic formation of rotational twins within the nanowire.

Ideally, TEM imaging would have been used to investigate the structure and possibly the composition of the NWQDs within the nanowires. However, this was not achieved for several reasons. The main difficulty stemmed from the low indium fraction within the NWQD. The high density of rotational twins relative to the expected axial size of the NWQD (~ 10 – 16 nm) meant that any contrast difference in conventional bright field TEM imaging due to the presence of InGaAs would be difficult to resolve as the contrast between successive rotational twins dominated the images. The low indium fraction also hindered identification of the location of the NWQD by strain resolved TEM. An indium

fraction of 15% corresponds to a lattice parameter for $\text{In}_{0.15}\text{Ga}_{0.85}\text{As}$ of $\sim 5.71\text{\AA}$, compared with 5.65\AA for GaAs (at 300K), giving a small lattice mismatch of $\sim 1.1\%$. The result is relatively little strain at the GaAs/InGaAs interface, making this much more difficult to identify in TEM images. Indeed, it has been reported elsewhere that low indium fraction InGaAs nanowire quantum wells grown in GaAs nanowires could not be observed by TEM⁴⁰. In contrast, an indium fraction of 30% within an InGaAs NWQD is sufficient to allow strain-resolved TEM imaging of the NWQD³¹.

Energy dispersive X-ray spectroscopy (EDX) was used to evaluate the outcome of the radial capping procedure for Sample 4B, in which a thin layer of GaAsP was grown on the vertical facets of the nanowire. An electron beam focussed to a diameter of $\sim 1\text{nm}$ was used to locally excite the nanowire in a raster pattern. This resulted in the emission of K-line X-rays from the constituent elements of the nanowire, which were subsequently detected. The energy of such X-rays is dependent on the element from which they originate, thus allowing for identification of the location of different elements within the nanowire.

The results of this procedure are summarised in Figure 4.3(e)-(h). As expected, gallium and arsenic atoms were seen to be dispersed uniformly throughout the nanowire (Figure 4.3(e) and Figure 4.3(f)). A weaker signal was observed from phosphorous atoms in the GaAsP capping layer, although it appeared that they did indeed cover the full extent of the nanowire, as expected from the growth procedure (Figure 4.3(g) and Figure 4.3(h)). Comparing Figure 4.3(g) and Figure 4.3(h), it was evident that at one end of the nanowire, there was a higher density of phosphorous atoms. This was therefore thought to be the growth front of the nanowire, indicating that some axial GaAsP growth occurred simultaneously with the radial growth of GaAsP. Ideally, EDX would have been used to

determine the phosphorous fraction within the GaAsP capping layer. This was not possible with the TEM software available, which could not accurately subtract the Bremsstrahlung background from the EDX measurements.

EDX spectroscopy was also used in an attempt to locate indium within the nanowire (and therefore locate the NWQD). However, the nanowires in question were several microns in length and it was not entirely clear *a priori* where (or even if) the NWQD had formed within a particular nanowire. Whilst the growth times for the lower and upper GaAs sections of the nanowire were identical, the growth rate was not necessarily linear. Furthermore, the process of transferring the nanowires to the TEM grid could in principle break the nanowires at a point above the nanowire base. To accurately survey an entire nanowire with sufficient resolution to locate a nanometre scale InGaAs NWQD would therefore have been a prohibitively lengthy process. A few shorter duration scans were attempted, but these did not identify the location of the NWQD.

4.4.2 Optical characterisation

The NWQDs were extensively optically characterised using a non-resonant micro-PL technique at a temperature of 4K. The sample was mounted on the piezo stages of a gas exchange cryostat, allowing complete motional control in three orthogonal spatial directions. An aspheric lens with a numerical aperture (NA) of 0.55 was used to focus a 650nm continuous wave diode laser onto the sample. This generated carriers within the NWQD both by direct excitation and carrier trapping from the surrounding GaAs nanowire. The photons emitted when the excited NWQD relaxed to the unoccupied state were collected by the same lens, and spectrally resolved using a single grating, 0.5m focal length spectrometer with a thermoelectrically cooled silicon charge-coupled device

(CCD) camera. The spectrometer had two gratings with 600 lines/mm and 1200 lines/mm respectively, the latter giving a spectral resolution of $\sim 130\mu\text{eV}$.

The majority of the PL analysis focussed on a single array on Sample 4B, for which the nanowire diameter was $\sim 120\text{-}140\text{nm}$. In the following this will be assumed unless otherwise stated.

4.4.2.1 Low power PL measurements

At low laser pump powers, typically on the order of $50\text{mW}/\text{cm}^2$ (based on a focussed laser spot $1.5\mu\text{m}$ in diameter), a single peak was observed in the PL spectra for a large fraction ($\sim 60\%$) of nanowires. The peak lay energetically between 1.40eV and 1.45eV . For comparison, at similar powers sharp PL emission lines related to recombination within the GaAs nanowire were observed at $\sim 1.49\text{eV}$. The implications of the GaAs nanowire PL will be discussed later. At higher pump powers the GaAs nanowire PL emission was overwhelmed by the substrate PL which consisted of two spectral features at 1.489eV and 1.515eV . (The lower energy peak is related to carbon impurity doping whilst the higher energy peak is due to bulk excitonic recombination in zinc blende GaAs⁵⁰). Some nanowires did not show any features above the background noise level even upon increasing the laser power (other than GaAs related PL), and were therefore assumed not to contain an optically active NWQD. Upon increasing the laser pump power slightly a second peak associated with the NWQD was sometimes observed in close energetic proximity to the first. An example of such spectra is given in Figure 4.4(a). The integrated intensity of the higher energy peak was determined to increase in an approximately linear fashion with laser pump power (actually ~ 1.29), whilst for the lower energy peak the intensity increased quadratically with the pump power (Figure

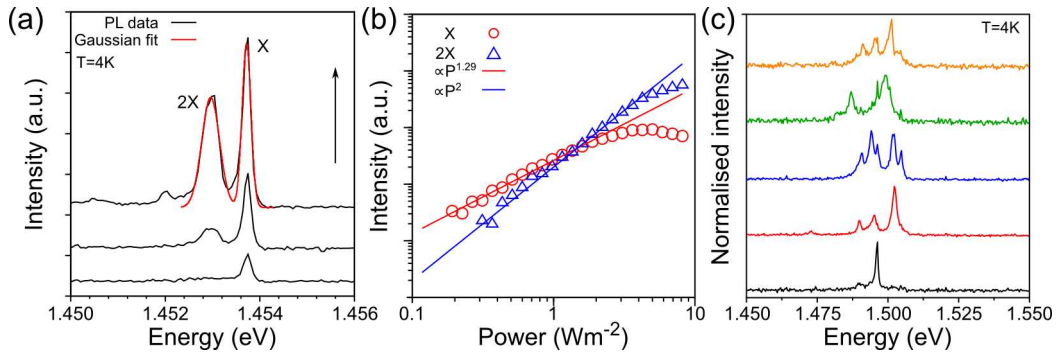


Figure 4.4. Low power PL measurements on single nanowires. (a) Low power PL spectra from a single NWQD showing exciton (X) and biexciton (2X) emission. The arrow denotes increasing laser pump power. Spectra offset in y for clarity; (b) Integrated PL intensity (log-log plot) for the exciton and biexciton as a function of laser pump power. The exciton intensity is seen to increase at a power of ~ 1.29 with laser pump power, the biexciton intensity as the square of the laser pump power; (c) Low power normalised PL spectra from single nanowires showing sharp line emission around the GaAs zinc blende bandgap.

4.4(b)). Such behaviour is typical for the exciton (X) and biexciton (2X) respectively in InGaAs QDs²⁰. The positive binding energy of the biexciton (leading to PL emission at lower energy than the exciton) for this NWQD was $\sim 760\mu\text{eV}$. Definite attribution of the two lines as the exciton and biexciton could be achieved by performing cross-correlation measurements between the two emission lines, in which one would expect to observe photon bunching due to the 2X-X cascade. This would rule out the small possibility that the exciton line as claimed here was not in fact a charged exciton. However, as described in section 4.4.2.5, such measurements were extremely difficult to undertake for these NWQDs.

Ignoring for the moment the exciton binding energy, quantum confinement effects and potential strain within the NWQD, an initial estimate for the indium fraction within the NWQD can be made. Including the bowing parameter for the bandgap of $\text{In}_x\text{Ga}_{(1-x)}\text{As}$ at

low temperature⁵¹, the indium fraction is estimated to be 4.4% – 7.7% (corresponding to energies between 1.40 and 1.45eV). Quantum confinement would increase the energy of the exciton and therefore this is most likely a lower limit to the indium fraction. In comparison, as mentioned previously for the growth conditions and MOCVD reactor used here the indium fraction had been estimated to be ~15% for planar InGaAs growth on (100) substrates.

The linewidth of QD exciton PL influences the coherence time for emitted photons, and has a minimum determined by the radiative lifetime of the exciton through the Heisenberg Uncertainty Principle. The radiatively limited linewidth for a SK QD is typically of the order of ~1 μ eV. For the NWQDs, low power exciton linewidths of 140 μ eV and greater were measured. Whilst for self-assembled QDs linewidths down to several microelectronvolts have been observed under resonant excitation⁹, larger linewidths such as those measured here are commonly observed for selective area growth techniques^{20,21,31}. Indeed, aside from linewidths of ~31 μ eV reported for InAsP NWQDs⁴³, all other NWQD linewidths reported to date are greater than 85 μ eV.

One possible exciton PL broadening mechanism is the fine structure splitting (FSS), which in the case of self-assembled QDs often arises due to the influence of shape anisotropy on electron-hole exchange interactions⁵². FSS acts to transform the circular basis of the bright excitons in the absence of QD asymmetry to a superposition of linear polarisation states. The influence of FSS can therefore be resolved using linearly polarized detection with the two bright excitons emitting photons with orthogonal polarization. However, FSS is usually measured to be on the order of a few to a few tens of microelectronvolts. Moreover, growth of QDs on (111)B oriented substrates has been shown both theoretically²⁷ and experimentally⁵³ to lead to very low values of the FSS.

A more likely explanation is that spectral diffusion is the cause of relatively broad exciton linewidths. In a NWQD, spectral diffusion is potentially a result of the close proximity of

the nanowire surface, which has unsatisfied dangling bonds acting as traps for charge carriers. Alternatively, carriers may be confined at the rotational twin interfaces, where a type-II band offset exists due to the different bandgaps of zinc blende and wurtzite crystal phases and their relative band alignment. Evidence for carrier localization in regions of the nanowire distinct from the NWQD came in two forms. Firstly, as previously mentioned the PL emission from the nanowire itself at the GaAs zinc blende bandgap exhibited several narrow peaks at low laser excitation power. The nanowire PL emission is shown in Figure 4.4(c). As reported elsewhere in the literature, this is evidence of rotational twin-induced confinement of carriers within the nanowire⁵⁴. There is however no evidence of state filling which is indicative of a weakly confined energy state, and at higher powers the PL emission simply broadens into the usual single peak representing the GaAs band edge. The characteristics of this PL emission are therefore significantly different to those of the NWQDs. Further evidence of carrier localization occurring within the nanowire is seen in long PL lifetimes, characteristic of spatially indirect carrier recombination. This will be discussed in section 4.4.2.5.

4.4.2.2 Evidence for a single NWQD in a single nanowire

At this point, it is instructive to demonstrate that the observed exciton emission was indeed the result of the growth of a single NWQD within the nanowire. Due to the band offset between zinc blende and wurtzite, it is possible to observe type-II confinement within a homogeneous nanowire (e.g. pure GaAs), resulting in sharp line PL emission from what has been referred to as ‘crystal phase’ quantum dots⁵⁵. However, it was clear for a number of reasons that the PL emission observed from the NWQDs discussed here was not a result of such polytypism. Firstly, the PL spectrum from a polytypic nanowire is typically quite convoluted, with many recombination energies possible due to the varying lengths of zinc blende and wurtzite segments, and hence varying carrier confinement energies (for an example of this for InP nanowires see Chapter 6). Such a

spectrum was never observed from the NWQDs considered here – a maximum of one exciton line was observed per nanowire below the zinc blende GaAs bandgap energy.

Figure 4.5 demonstrates the localized nature of the single low energy emitting region within a nanowire (i.e. the location of the NWQD). The data in this image was obtained from a nanowire which had been knocked over onto the substrate upon application of a lateral force via a solid immersion lens (SIL). A SIL is a hemisphere or supersphere with a high refractive index n_{sil} which is used to overcome the free space diffraction limit, thus enabling higher resolution imaging. The theoretical enhancement of the resolution is n_{sil} and n_{sil}^2 for the hemispherical and superspherical SIL respectively. The shape of the SIL also results in superior collection of PL from the sample by increasing the effective numerical aperture of the optical setup. In this case, a zirconium dioxide SIL with a refractive index of ~ 2.18 was used, giving a theoretical resolution of 170nm for a laser

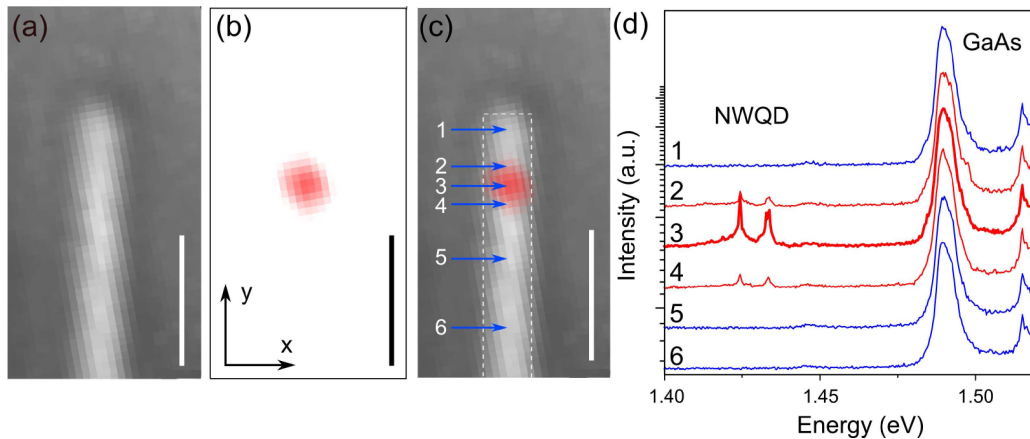


Figure 4.5. PL intensity map for a nanowire lying on the growth substrate. (a) Two dimensional x-y map showing integrated intensity of scattered laser light from a GaAs substrate on which a single nanowire is lying. The nanowire can be seen in the lighter region; (b) Two dimensional x-y map showing integrated PL intensity for the NWQD within the nanowire. Higher intensity shown in red; (c) Overlay of (a) and (b); (d) Sample PL spectra used to form the intensity maps in (a-c). Numbers correspond to the locations given in (c). Scale bars 2 microns.

wavelength of 808nm. To obtain the data in Figure 4.5, the laser was automatically raster scanned across a square region of the sample which contained nanowires. At each step, the PL signal was accumulated for 1s. To determine the location of the nanowire itself, the resulting PL spectra were integrated over the energies for which scattered laser light could be observed (energies greater than the GaAs emission energy, but less than the laser peak photon energy of 1.536eV). The integration was then repeated over the energy range for which only NWQD emission could be observed, in this case between 1.378eV and 1.476eV. The data was then plotted separately as two-dimensional intensity plots (Figure 4.5(a) and Figure 4.5(b)), then overlaid to form Figure 4.5(c). The use of quasi-resonant excitation ensured that the focal distance was approximately the same for both the laser scatter and the NWQD PL, preventing chromatic aberrations affecting the overlaid image. Figure 4.5(d) shows representative PL spectra obtained during this process. Several nanowires were measured in this way, and a maximum of one location per nanowire was observed to show PL emission below the GaAs bandgap. Such emission was therefore assigned to an InGaAs NWQD and the presence of crystal phase QDs was ruled out.

4.4.2.3 NWQD excited state observation and modelling

Increasing the laser pump power resulted in the clear observation of filling of the excited states of the NWQD. A representative power dependent PL spectrum is shown in Figure 4.6(a). Up to six excited states were observed, with the number varying between different NWQDs. The number of excited states that could be observed was limited by the finite potential barrier present in the nanowire growth axis. Typical state separations were of the order of 4-8meV for the NWQDs on this array. The atypical state separation shown in Figure 4.6(a) (~14meV) allows easier viewing of the excited states.

In order to understand the state separations observed, a simple model of the NWQD as a cylinder with a diameter of ~140nm (determined by the nanowire diameter) and a height

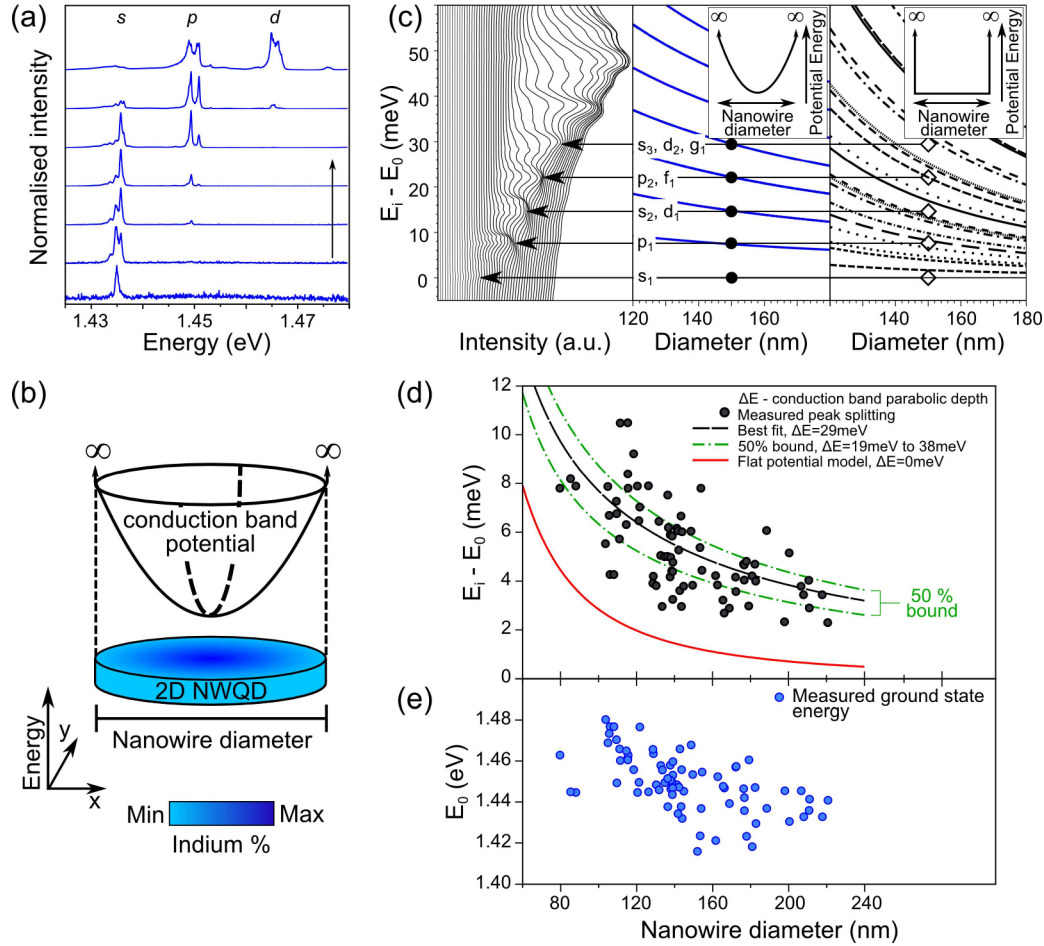


Figure 4.6. Modelling NWQD PL characteristics. (a) Normalised power dependent PL spectra from a single NWQD (increasing power denoted by arrow), showing emission from the ground state (*s*) and two excited states (*p* and *d*). Spectra are offset in *y* for clarity; (b) Parabolic radial conduction band model for the NWQD, caused by a variation in the indium fraction across the radial dimension of the NWQD; (c) Power dependent PL spectra from a single NWQD (left panel – spectra offset in *x* for clarity), with fit to energy states derived from parabolic potential model (centre panel) and failure of fit to energy states of a flat potential model (right panel). Insets show a schematic of the potential being considered; (d) First excited state to ground state energy splitting measured as a function of nanowire diameter. The red line shows the failure of the flat potential model to fit the data. The dashed black line gives the best fit to the data using the parabolic potential model, and the green dot-dash lines bound 50% of the data points about the best fit line; (e) Ground state energy for the NWQDs measured in (d).

of $\sim 16\text{nm}$ (from a linear growth rate approximation) was initially considered[‡]. In the radial direction the model considered the confining potential to be infinite (in actuality close to the electron affinity energy, neglecting the GaAsP capping layer in Sample 4B) whilst in the axial (growth) direction the confining potential was provided by the conduction band and valence band offsets at the GaAs/InGaAs interface. The indium fraction within the NWQD was taken to be 15% (estimated from the growth conditions) and assumed to be constant throughout the NWQD, therefore producing a flat, radially invariant potential. The total bandgap offset was split 60:40 between the conduction and valence bands, and the electron and hole effective masses were approximated as those for GaAs.

The model failed to adequately describe the observed state separations. Assuming a radially symmetric NWQD, two sets of excited states should exist, due respectively to radial and axial confinement. As a result of the shape anisotropy of the NWQD, confinement in the radial direction is much weaker than in the axial direction. The lowest energy excited states are therefore the result of radial confinement. The model predicted a first excited state lying at an energy $\sim 1\text{-}2\text{meV}$ higher than the ground state, with higher order radially confined states separated by increasing amounts energetically. However, the smallest first excited state to ground state transition energy observed was $\sim 4\text{meV}$. Furthermore, the excited states were approximately linearly spaced in energy.

Given these observations, a new model was proposed in which a harmonic potential was introduced in the radial direction of the NWQD. Such a potential leads to greater radial confinement of carriers and therefore higher energy levels. It also produces

[‡] Theoretical modelling of NWQDs was undertaken by Dr Thomas Grange at the Walter Schottky Institut, Centre for Nanotechnology and Nanomaterials, Technische Universität München, Germany

approximately equally spaced energy levels in the large NWQD radius limit, as observed experimentally. The presence of such a potential can be explained by assuming that a fraction of the indium incorporated near the edge of the NWQD desorbed during the growth of the upper GaAs section of the nanowire, thereby modifying the bandgap as a function of NWQD radius. It is thought to be unlikely that such a potential arose from a surface depletion layer and resulting surface band bending which has been observed previously for unpassivated GaAs nanowires⁵⁶, as a GaAsP capping layer was grown around the nanowires. The capping layer should suppress the formation of a surface depletion region.

The harmonic potential is described schematically in Figure 4.6(b). In Figure 4.6(c), the good agreement of this model with representative power dependent PL spectra from a single NWQD is demonstrated. The confined energy states are labelled l_α in terms of their azimuthal quantum number $l=s,p,d\dots$ and radial quantum number $\alpha=1,2,3\dots$. The flat potential model initially considered is also shown for comparison.

The energy difference between the exciton and the first excited state for 75 NWQDs with a range of diameters from 80nm to 220nm was determined from PL measurements. This data is plotted in Figure 4.6(d). From the data it is apparent that the energy splitting increased with decreasing nanowire diameter, and therefore decreasing NWQD diameter. In the absence of other effects (for instance strain) this is as expected, with the increased confinement provided in the radial direction leading to increased confinement energy for charge carriers, and therefore greater excited state splitting energies. From Figure 4.6(d) it is seen that 50% of the data values can be explained by a harmonic conduction band depth between 19meV and 38meV. Assuming once more a maximum of 15% indium fraction within the NWQD, these values correspond to a NWQD with 15% indium

fraction at the centre of the NWQD, decreasing to a value lying between 10.5% and 13% at the NWQD radial edge. By considering a hard wall (infinite potential) boundary condition at the radial edge of the NWQD, the absolute values of the energy states are not considered in this model. For small indium fractions the bandgap of $\text{In}_x\text{Ga}_{1-x}\text{As}$ varies in an approximately linear fashion with x . In this regime therefore the absolute percentage change in indium fraction between the centre and radial edge of the NWQD is independent of the absolute value of the indium fraction at the NWQD centre. The main constraint in the current model (which was satisfied for all NWQDs measured) is that the absolute percentage change must not be greater than the indium fraction at the centre of the NWQD. Were this to be the case, the harmonic potential would flatten near the radial edge of the NWQD (i.e. it would correspond to pure GaAs).

The analysis above disregards the influence of strain on the NWQD energy levels. Strain arises within the NWQD due to the lattice mismatch between InGaAs and GaAs, and in the case of Sample 6B from the compressive strain of the GaAsP capping layer acting on the entirety of the nanowire. In the case of the latter, the impact on the NWQD is thought to be negligible. GaAsP capping layers have been shown to blueshift considerably the PL emission energy of GaAs nanowires^{57,58} which was not observed for the nanowires of Samples 6A and 6B. For these samples the emission energy was $\sim 1.5\text{eV}$, as expected for zinc blende GaAs at 4K. This is thought to be due to low phosphorus content within the thin capping layer. On the other hand, the low strain energy due to axial lattice mismatch was evidenced by the inability to locate the NWQD using strain-resolved TEM. Incomplete knowledge of the compositional profile of the NWQD makes determining the impact of such strain difficult however, and this remains an open question.

It should be noted at this point that the exciton energy as a function of nanowire diameter showed the opposite dependence to that expected. Given that the axial NWQD dimension of $\sim 10\text{--}16\text{nm}$ was much smaller than the radial dimension, it was expected that axial confinement would be the chief determinant of the exciton energy. As the nanowire diameter decreased the height increased, and therefore the height of the NWQD increased also. The exciton energy should therefore increase with increasing nanowire diameter due to increased axial confinement. This would be opposed to a lesser degree by decreased confinement in the radial direction. The measured exciton energy as a function of nanowire diameter is shown in Figure 4.6(e). The opposite trend to that expected is clearly seen. One explanation for such a trend is that the indium fraction within the NWQD decreased with decreasing nanowire diameter. This is suggested by the observation during this work that NWQDs formed less successfully in narrower nanowires (less than $\sim 90\text{nm}$ diameter). Such an observation has been made previously for InGaAs axial heterostructures in GaAs nanowires⁴⁰. The energy state model discussed above still holds for this case as the energy levels in the model are independent of absolute indium fraction.

4.4.2.4 NWQD PL homogeneity

As previously discussed, there are two significant advantages of site-controlled QD growth techniques over their self-assembled equivalents. Whilst site control provides a route to easing future fabrication based on the controllable density and deterministic location of a QD, it also presents an opportunity for control of the QD dimensions. Site control is therefore an appealing technique for the development of more uniform QD distributions with regards to optical properties.

With this in mind, Figure 4.7(a) presents statistical data for the exciton emission energy of 42 NWQDs from the same array (and therefore nominally the same diameter, $\sim 140\text{nm}$). These were obtained by scanning three columns of nanowires (75 nanowires) and obtaining a low power PL measurement from every one which showed NWQD PL emission. To demonstrate the reproducibility of the NWQD PL emission, Figure 4.7(b) shows three PL spectra taken from three different NWQDs on the same column of the array at the same laser excitation power. The similarity in the emission energy and PL intensity is striking.

The full width half maximum (FWHM) of the emission energy data shown in Figure 4.7(a) was calculated using the raw energy values, whilst the data is binned in increments of 3.3meV . A FWHM of $15.0\text{meV} \pm 2.8\text{meV}$ was determined from the raw data values. This is approximately a factor of two better than standard growth by the SK technique¹⁵,

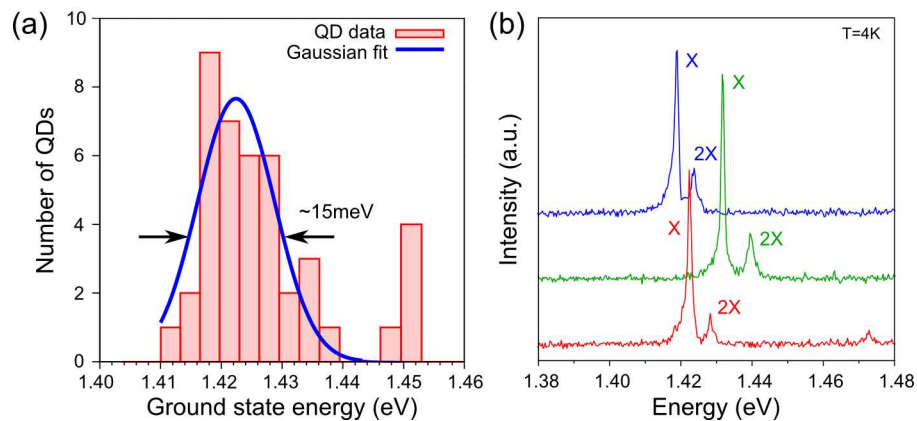


Figure 4.7. Ensemble PL statistics from an array of NWQDs. (a) Ground state energy for 42 NWQDs, with Gaussian fit to the data revealing an ensemble broadening of $\sim 15\text{meV}$; (b) Sample PL spectra from 3 NWQDs from one column of a nanowire array (25 nanowires), showing remarkable similarity in emission profile.

and compares favourably with other reports of site controlled InGaAs QD growth in the literature²¹. The FWHM of a QD ensemble is usually dependent on the confinement energy of the QDs. Smaller QDs providing greater carrier confinement and larger excited state splitting energies generally exhibit larger ensemble broadening⁵⁹. The improved FWHM observed for the NWQDs reported here should thus be considered simultaneously with the relatively weak confinement of the NWQDs. However, this still represents an encouraging first step towards formation of homogeneous NWQD arrays. Particularly notable is the realisation of uniform NWQD PL emission in this system even in the presence of rotational twins, which might be expected to influence the NWQD emission properties (as indeed is suggested by the results in section 4.4.2.5). The variation in the crystal structure in the vicinity of the NWQD appears to have no deleterious effects on the NWQD PL uniformity.

It is likely that the FWHM could be reduced further by careful tailoring of the fabrication process to ensure each nanohole in the growth mask has the same dimensions, and possibly by controlling the nanowire growth rate. In the case of the former, nanohole anisotropy can often occur due to slight misalignment of the electron beam during patterning. With regard to the nanowire growth rate, it has been observed during the course of this research that overly fast growth rates often result in a small variation in the resulting nanowire dimensions, including the formation of different length side facets (skewed hexagonal morphology). Reducing the growth rate was seen to act favourably to improve nanowire to nanowire uniformity.

4.4.2.5 NWQDs for quantum computing?

One possible application of position controlled QDs lies in linear quantum computation. Amongst the requirements for such an application are a high single photon emission rate, and a highly coherent source (indistinguishable photon emission)⁶⁰. A high emission rate increases the speed at which measurements can be taken, whilst the production of indistinguishable single photons is mandatory for interference measurements. The coherence of the NWQD emission is related to the PL linewidth as discussed previously, and approaches for reduction of the PL linewidth will be discussed in section 4.5.1. First, measurements of PL lifetimes are presented, followed by a demonstration of single photon emission from a NWQD.

The PL lifetime of a confined energy state reveals details of carrier dynamics within the semiconductor, for instance the presence of fast non-radiative recombination (resulting in a short PL lifetime) or spatially indirect recombination (long PL lifetimes). To measure the exciton PL lifetime of a single NWQD, a pulsed laser operating at 405nm was focussed onto a nanowire. The power was chosen such that only the excitonic transition was observed (typically ~1nW). The PL emission from the nanowire was then collected and focussed onto an avalanche photodiode (APD). The experimental setup is described schematically in Figure 4.8(a). As an APD does not discriminate between photons spectrally, a bandpass filter was placed in the collection path. The bandpass filters used had a transparency window of 10nm, and were chosen such that the central wavelength of the transparency region was coincident with the energy of the exciton. This process removed much of the background signal and thus enabled lifetime measurements to be taken more quickly. For comparison, a lifetime measurement was also undertaken using a filter with a bandpass region centred on the GaAs nanowire PL emission.

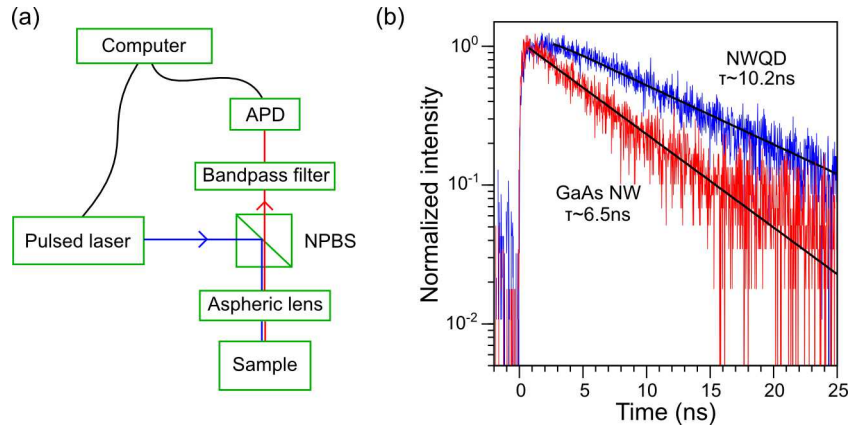


Figure 4.8. PL lifetime measurement for a single NWQD. (a) Schematic of the optical setup used to determine NWQD PL lifetimes. NPBS – non-polarizing beam splitter, APD – avalanche photo diode; (b) Normalized, time resolved PL intensity for a NWQD (blue trace) and the GaAs nanowire (red trace). The black lines are monoexponential fits to the data revealing lifetimes of ~ 10.2 ns and ~ 6.5 ns respectively.

The results of these measurements are shown in Figure 4.8(b). PL lifetimes observed for both the GaAs nanowire and the InGaAs NWQD were considerably longer than the typical PL lifetime of ~ 1 ns observed for SK InAs QDs⁶⁰. Mono-exponential fits to the data revealed a nanowire lifetime of ~ 6.5 ns and NWQD lifetime of ~ 10.2 ns. The long PL lifetimes could potentially be the result of spontaneous emission suppression as discussed in Ref 61. As the nanowire diameter is reduced the fundamental guided optical mode of the nanowire becomes less well confined and spontaneous emission from dipoles orientated perpendicularly to the nanowire axis is suppressed due to the reduction in the local optical density of states. Such an effect has indeed been observed for InAsP NWQDs⁴⁴. Confirmation that this is the case would require lengthy further PL lifetime measurements on NWQDs with varying diameters. However, the crystal structure of the nanowire in the vicinity of the NWQD must also be taken into account. As described previously, the nanowires contained a significant density of rotational twins, the twin

interface resulting in a monolayer of wurtzite crystal structure. Only a few successive rotational twins are required to spatially separate carriers in the resulting type-II bandstructure. This effect also leads to longer PL lifetimes due to the reduced overlap of the respective carrier wavefunctions⁵⁴. As the occurrence of rotational twins varies between nanowires, it is not easy to discriminate between the Purcell effect increasing the PL lifetime and the influence of rotational twins.

With regard to the requirements of quantum computation, the long lifetimes reported here are clearly undesirable as they lead to a low photon emission rate. The lifetime may be reduced by increasing the thickness of the radial capping layer so that the final nanowire diameter provides optimal coupling of the NWQD emission into the fundamental guided optical mode. Optimal coupling for an on-axis dipole in a GaAs nanowire occurs for a diameter of $\sim 0.23\lambda$, or $\sim 200\text{nm}$ ⁶¹. Addressing the impact of rotational twins on the PL lifetime is more challenging. To date, there have been no reports of successful control of rotational twin density in GaAs nanowires grown by the catalyst-free technique, although such control has been shown for VLS grown GaAs nanowires^{62,63}. However for integration with photonic crystals planar overgrowth of the nanowires may be required. This has already been demonstrated for GaAs^{64,65}. A particularly appealing aspect of this overgrowth was the reported elimination of rotational twins within the nanowires⁶⁵. Provided the optical properties of the NWQD do not degrade significantly during the overgrowth process, this may well result in shorter PL lifetimes through replacement of the type-II recombination pathway with a type-I pathway. Fabrication of a photonic crystal cavity with the NWQD at an electrical field antinode would also lead to an increased photon emission rate via the Purcell effect, further reducing the PL lifetime.

An extremely useful property of QDs is their ability to emit single photons. When a single exciton within a QD recombines to emit a photon, the QD is left unpopulated. It is therefore impossible for a further photon to be emitted immediately at the exciton energy i.e. the probability of simultaneous emission of two photons is zero. This leads to the temporal separation of the train of photons emitted by a QD which is continually pumped, a situation described as antibunching of the emitted photons and proof of the quantum nature of light. A common method for evaluating the photon statistics for a quantum emitter is to measure the second order intensity correlation function, $g^{(2)}(\tau)$ using a Hanbury Brown and Twiss (HBT) setup. The PL emission from a QD is split at a 50:50 non-polarising beamsplitter and the coincidence counts for the resulting outputs measured. For continuous wave excitation a dip in coincidences occurs at zero time delay (to zero ideally), rising to unity at times before and after zero time delay. The rise time for the dip is dependent on the excitation and relaxation times of the system⁶⁶.

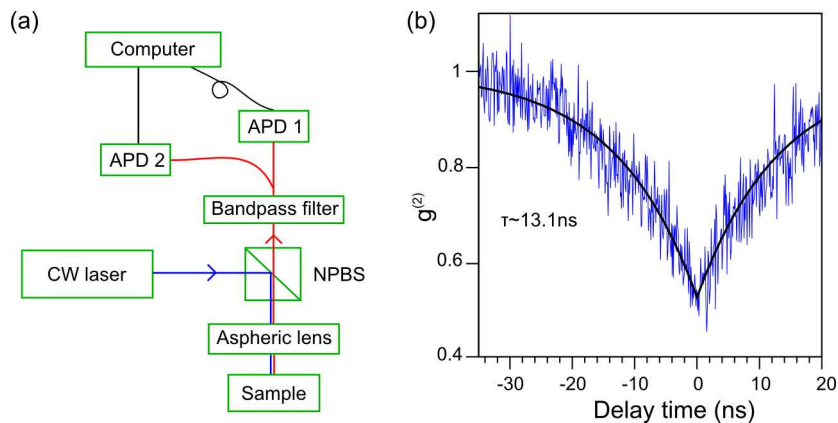


Figure 4.9. Second order autocorrelation measurement for exciton PL emission from a NWQD. (a) Schematic of Hanbury Brown and Twiss setup; (b) Second order autocorrelation data for a single NWQD, with a minimum of ~ 0.5 at $\tau=0$. The black line is a monoexponential fit to the data, revealing a lifetime of ~ 13.1 ns.

Single photon emission from the NWQDs was demonstrated using an HBT experimental setup, shown schematically in Figure 4.9(a). A single NWQD was excited using a non-resonant continuous wave diode laser operating at 650nm. PL emission from the excitonic line of the NWQD was filtered through a 10nm bandpass filter and passed through a 50:50 fibre beam-splitter. Due to the energetic proximity of the exciton and biexciton, the filter was unable to entirely eliminate the biexciton PL emission. The pump laser power was therefore reduced to decrease the biexciton PL emission intensity, although a compromise had to be reached to preserve the PL intensity of the exciton. Ideally the biexciton would have been filtered out completely, but a very narrow bandpass filter was unavailable, and filtering through a monochromator led to an unacceptable drop in count rate. The effect of the residual biexciton emission can be seen in the results described later.

The output from the fibres was focussed onto two separate free space APDs. The signal from the APDs was relayed to the timing module of a computer using cables of differing length, to provide a delay path between the two outputs. The shorter cable was connected to the APD which initialized timing by the computer upon detection of a photon. Timing stopped upon receipt of a signal from the second APD, indicating the arrival of a photon at this detector. The result was a histogram of two-photon coincidences as a function of time, binned in 100ps intervals. The results were normalized to the coincidence counts expected from a Poissonian source, $C_{Poisson} = N_1 \cdot N_2 \cdot w \cdot T$, where $N_{1,2}$ was the count rate on each APD, w the bin width and T the total accumulation time (62 hours). Further to this, a correction was made to the results as described in Ref 67. This took into account random coincidences in the data originating from the background signal. The adjusted autocorrelation function is $g^{(2)}(\tau) = [C_N(t) - (1 - \rho^2)] / \rho^2$ where $C_N(t)$ is the ratio of raw

coincidence counts to the coincidence counts of a Poissonian source and $\rho=S/(S+B)$, with S the emitter count rate and B the background count rate.

The results of the HBT measurement are shown in Figure 4.9(b). A dip can be seen in the results at zero time delay, corresponding to antibunching in the photon emission. The dip drops to $\sim 50\%$ of the maximum, which is the expected value for emission from a two photon emitter⁶⁸. However, given the presence of biexciton photons in the collected PL signal during this measurement, it is thought very likely that the true $g^{(2)}(0)$ is less than 50%, corresponding to single photon emission.

4.5 Further work

In the following section, three future directions for NWQD research are presented. First, initial efforts to improve the quality of NWQD PL emission through elimination of spectral diffusion are described. Next, the potential to tune the exciton emission energy through in-situ laser annealing is considered. Finally, two further samples are discussed. The first concerns an attempt at sequential growth of two NWQDs in the same nanowire, whilst the latter led to the observation of a blueshift in the power dependent PL from a NWQD.

4.5.1 Spectral diffusion measurements

As discussed previously, spectral diffusion may have a significant effect on QD PL linewidths, leading to broadening of the emission line relative to the radiatively limited linewidth. Negative effects of such broadening include the concomitant reduction in coherence length for photons emitted by the QD, and difficulty in achieving coherent optical control of single spin qubits. Typically the trapping processes which result in

spectral diffusion occur on an ultrafast timescale and therefore a time-averaged PL measurement taken on the second timescale gives an average measurement of the effect of spectral diffusion, resulting in linewidth broadening. Until recently, determination of the role played by spectral diffusion in linewidth broadening was limited to repeated collection of PL spectra on the shortest timescale possible. The timescale is governed for instance by the brightness of the photon source, and the response time of the CCD used. This usually limits the time resolution to the microsecond regime. In a recent development, photon correlation techniques have been reported with 90ps time resolution, allowing extraction of a characteristic spectral diffusion time. Coincidentally these measurements were undertaken on a NWQD^{69,70}.

Given the relatively low count rate observed from the NWQDs studied here employing the latter technique would have been impractical. As a first study of the influence of spectral wandering on NWQDs, the PL emission from the exciton of a single NWQD was measured continuously using an accumulation time of 10s over a period of one hour. A low excitation power was used to prevent possible power broadening of the exciton line. The resulting data was summed over 60s intervals to ensure a count rate sufficiently above the noise level for accurate peak fitting. The process was repeated for several NWQDs on the same array. Figure 4.10 shows the exciton energy and linewidth as a function of time for two different NWQDs. In the upper panel of each set of data, the y-axis gives the exciton energy relative to the lowest exciton energy measured for that NWQD. The exciton energy was seen to vary within an energy range of 60–180 μ eV, with the corresponding FWHM of the fitted Gaussian peaks showing a measurement to measurement variation in the range of 40–150 μ eV. As a comparison, a similar set of

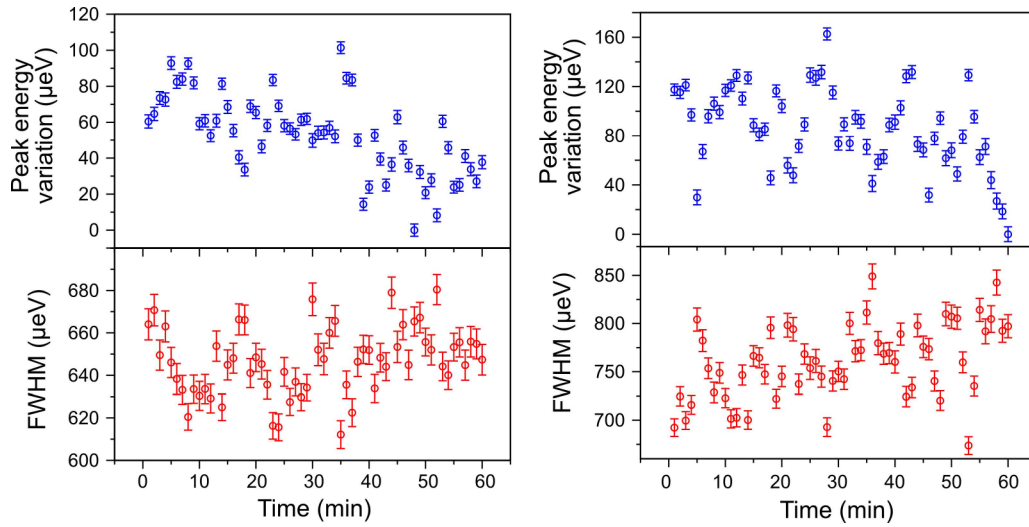


Figure 4.10. Low power PL measurements on individual NWQD excitons revealing spectral diffusion effects. In each figure, the top panel gives the variation of the exciton PL emission peak for the NWQD as a function of time. The data has been adjusted such that the lowest energy recorded is set to zero. The lower panel of each figure gives the full width half maximum (FWHM) of the PL emission as a function of time. Error bars are derived from the fitting procedure.

measurements taken for an SK QD revealed a variation of the exciton energy over time that was less than $2\mu\text{eV}$. This is unambiguous evidence that spectral diffusion processes had a significant effect on the linewidth of the NWQD exciton.

Spectral wandering of the NWQD exciton may have two origins unique to the nanowire structure. Temporary capture of carriers at rotational twin interfaces may be eliminated through careful control of the growth conditions to prevent rotational twin formation⁷¹. However, to date this has only been achieved for VLS grown nanowires and not for catalyst-free GaAs nanowires. A second contributory factor arises due to the large surface area presented by the nanowire surface in close proximity to the NWQD. The energy of the surface states may lie within the energy gap of the semiconductor, consequently acting as carrier traps⁷². The growth of the radial GaAsP capping layer on Sample 4B was

intended to reduce the impact of non-radiative recombination due to surface states. Some improvement in PL intensity was seen relative to uncapped nanowire samples, suggesting the capping layer did act as intended. However, it was possible that the as-grown capping layer was insufficiently thick to prevent spectral diffusion broadening of the exciton linewidth. In an attempt to elucidate which mechanism was dominant in the broadening of the exciton linewidth, several post-growth passivation procedures were undertaken.

For the first surface passivation procedure $\sim 100\text{nm}$ of SiO_2 was deposited conformally onto the nanowires using PECVD. This experiment was motivated by a report of SiO_2 capping of nanowires⁷³ after which the PL emission intensity was unaffected. The sample was first immersed for 30s in a 1:19 $\text{NH}_3:\text{H}_2\text{O}$ solution to remove the native surface oxide, followed by a 30s rinse in DIW and drying in N_2 . The sample was then transferred directly to the PECVD equipment which was immediately evacuated to prevent regrowth of the surface oxide. 100nm of SiO_2 was deposited onto the nanowires at a substrate temperature of 300°C using silane (160sccm flow rate) and N_2O (900sccm flow rate) as sources of silicon and oxygen. SEM analysis before and after the process confirmed that the deposition thickness was indeed $\sim 100\text{nm}$.

The capping process was found to strongly quench the NWQD emission. The success reported in Ref 73 suggests that this was not due to an intrinsic incompatibility between PECVD-deposited SiO_2 and the nanowires (although note that different semiconductors were used in each case). It is possible that the failure was due to the deposition conditions utilised or, more likely, regrowth of the surface oxide between the DIW rinse and evacuation of the PECVD chamber. A defective interface would then have existed between the nanowire and the conformal coating. The quenching of the PL emission

implies that the interface acted as a centre for enhanced non-radiative recombination processes.

Two other possible reasons for the apparent quenching of the PL are excluded as follows. Both thermal annealing and capping-induced strain may alter the emission energy of the NWQD. Thermal annealing is commonly undertaken to reduce the ensemble broadening of SK QDs, during which the ensemble PL emission is seen to blueshift⁷⁴. Capping-induced strain may also significantly alter the emission energy as described in Ref 73. In the case of the NWQDs considered here, which were weakly confined due to the growth conditions, there lay the possibility that the NWQD PL emission could effectively disappear due to these effects. However, the energy of the limited PL emission that was actually observed had not altered significantly. It was therefore more likely that the PL quenched due to enhanced non-radiative recombination processes. A more promising *ex-situ* surface passivation procedure involves the application of a sulphide coating to the nanowire surface, followed by deposition of a conformal capping layer to prevent degradation of the sulphide layer. A suitable sulphide-based compound for surface passivation of nanowires is $(\text{NH}_4)_2\text{S}_x$ ^{75,76}.

An obvious method to increase the separation between the NWQD and the nanowire surface is to increase the thickness of the radial capping layer. This has the further advantage that optimum coupling of the NWQD into the fundamental optical mode of the nanowire may be achieved simultaneously. In future, a thicker radial capping layer would most likely be grown *in-situ*, before the substrate was removed from the MOCVD reactor. However, as a demonstration that the capping layer could be grown with a greater

thickness than for Sample 4B, radial overgrowth was undertaken on a nanowire sample which had already been characterised by PL measurements.

The sample was first rinsed in 1:19 $\text{NH}_3:\text{H}_2\text{O}$ for 30s to remove the surface oxide, followed by a DIW rinse for 30s and drying in N_2 . It was then loaded immediately into the MOCVD reactor which was subsequently purged with hydrogen. Due to the restrictions imposed by the dimensions of the cryostat used during PL measurements the sample size was approximately 0.5cm by 0.5cm. Normally nanowire samples were grown on half of a two inch wafer, with a significantly larger growth surface. To prevent excessive growth on the smaller sample, half of an unprocessed two inch (111)B GaAs wafer was placed next to the sample in the reactor to act as a dummy substrate.

It is normal practice to thermally clean the substrate before growth using an elevated temperature under a group-V overpressure, as described previously. In order to reduce the possible impact of the annealing step on the NWQD embedded in each nanowire on the sample, a limited thermal anneal was undertaken at 750°C for 7 minutes under an AsH_3 overpressure. This included the time taken for the sample to be heated from 20°C. The sample was then overgrown with GaAs for 60s at 750°C using TMGa and AsH_3 sources, with flow rates of 40sccm and 150sccm respectively. The flow rates were chosen to maximise the radial growth rate and therefore minimize the duration for which the sample was held at an elevated temperature. The sample was cooled under an AsH_3 overpressure.

Figure 4.11 shows an SEM of a representative nanowire before the overgrowth procedure, alongside a nanowire from the same array (and therefore similar initial dimensions) after overgrowth. Note that the measurement was not taken on exactly the same nanowire, explaining the discrepancy in height between the two nanowires. From

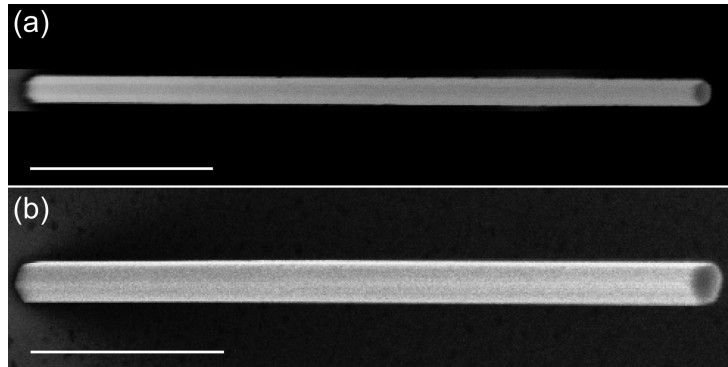


Figure 4.11. *Ex-situ* radial overgrowth of GaAs nanowires. 45° tilted SEM image of nanowires from the same array (a) before and (b) after radial overgrowth with GaAs. Scale bars 1 μm .

the SEM images it was estimated that $\sim 40\text{nm}$ of GaAs had been grown radially on the nanowires. PL measurements were then repeated on those NWQDs which had been previously characterised. It was found that the excitation power required to observe excited states had to be significantly increased compared with measurements taken before the radial capping procedure, and the NWQD PL signal saturated at a low count rate. A small reduction in the excited state separation was observed, whilst there was little change in the exciton energy. The reduction in PL intensity was therefore attributed once more to the presence of non-radiative recombination at the interface between the original nanowire and the capping layer. This may be improved by increasing the thermal annealing time prior to growth in order to fully remove the native surface oxide from the nanowires. However, it is more logical to form a thicker capping layer during the initial nanowire growth.

4.5.2 In-situ laser annealing of a NWQD

The lithographic definition of the NWQD location used in this work presents an encouraging route for the integration of position controlled QDs with photonic crystal cavities, as well as device scale up. As discussed in section 4.4.2.4 the homogeneity of the resulting NWQD ensemble emission is superior to that for SK QD growth. However, the ability to individually tune the emission energy of NWQDs would further simplify the search for multiple QDs with similar emission energies. To this end, *in-situ* laser annealing of a NWQD was attempted. By focussing a high power laser onto a single nanowire, tuning of the exciton energy through $\sim 1\text{meV}$ was demonstrated. Once the growth of NWQDs is sufficiently controlled such that narrow exciton linewidths are consistently observed, *in-situ* annealing presents a promising route for resonant tuning of separate NWQDs (in a manner similar to Ref 77).

Figure 4.12 shows low power PL emission from a single nanowire. The lower PL spectrum (blue line) shows the emission from the as-grown nanowire and the NWQD. Fine structure can be observed in the GaAs nanowire PL emission, which is attributed to carrier localization at rotational twin interfaces within the nanowire. The NWQD itself has an excitonic linewidth of $550\mu\text{eV}$. The middle trace (green line) shows the PL emission from the nanowire after exposure to a 632.8nm laser for 1s at 1mW . The NWQD PL intensity had decreased slightly, although the reason for this is unclear. The nanowire PL emission was significantly altered. It is possible that the high nanowire temperature induced by the laser led to structural modification of the nanowire itself, although this has yet to be investigated. The high temperature that can be reached by this technique was evidenced by nanowires melting under prolonged laser exposure.

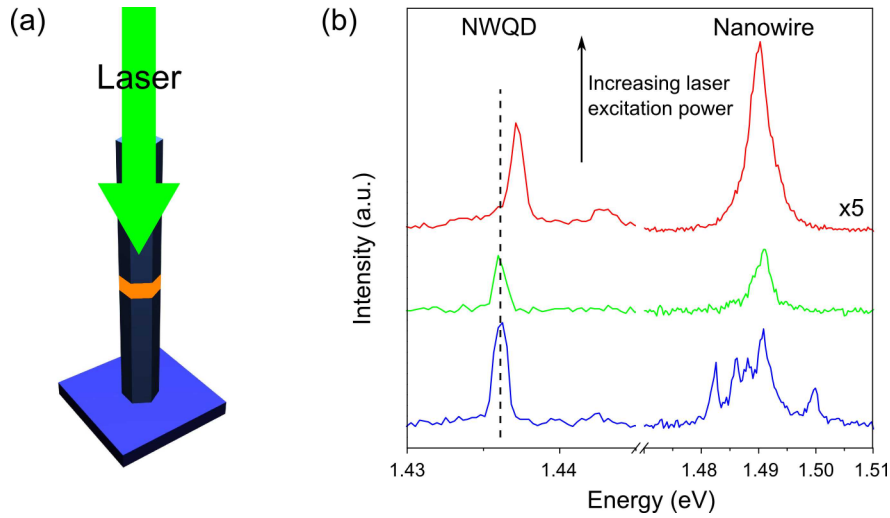


Figure 4.12. *In-situ* laser annealing of a single NWQD. (a) Schematic of the laser annealing process; (b) PL spectra taken after the laser annealing process, for an un-annealed nanowire (blue trace), annealing laser power 1mW for 1s (green trace) and 3.5mW for 300 seconds (red trace). Spectra offset in y for clarity.

The upper trace (red line) shows PL emission after exposure to the 632.8nm laser for 300s at 3.5mW. Note that the trace is scaled by a factor of five. It is clear that prolonged exposure to the annealing laser altered the excitonic emission energy of the NWQD. The exciton linewidth at this point was $590\mu\text{eV}$, which within the error of the fitting procedure is consistent with the original linewidth prior to laser annealing. However, the emission energy had increased by $\sim 1\text{meV}$. The fact that the exciton energy was seen to blueshift is consistent with reports in the literature concerning thermal annealing of QDs⁷⁴. The high temperature experienced by the NWQD during the annealing process allowed for intermixing of group-III atoms (indium and gallium), reducing the indium fraction within the NWQD and increasing the NWQD bandgap. The intermixing also effectively increased the NWQD size. The blueshift in energy observed for the NWQD was smaller than typical blueshift values reported for thermally annealed SK QDs. This

may be due to the weak initial confinement of the NWQD and potentially allows fine control of the NWQD emission energy. To enable greater tuning of the emission energy without causing structural damage to the nanowire, either the annealing laser power could be carefully controlled, or a pulsed annealing laser might be required. This may enable a constant temperature to be reached as in the standard thermal annealing process.

Whilst it is difficult to estimate the temperature reached by the NWQD during the annealing step, SEM analysis of the nanowires after annealing revealed structural changes for longer annealing times. The top section of a structurally-modified nanowire appeared to have melted, forming a sphere at the top of the nanowire. This suggests that significant thermal decomposition of the nanowire had occurred, which for the upper (111)B surface begins to occur at 630°C and increases rapidly with higher temperature⁷⁸. A finite element method numerical technique for semiconductor temperature determination under laser irradiation has been described elsewhere for quantum well laser annealing⁷⁹. A common technique to protect the surface of a sample during thermal annealing at high temperatures involves the application of a conformal SiO_x layer to the sample before the annealing step. The coating may then be removed using a fluoride based etch. It is likely that degradation of the nanowire surface was responsible for the decrease in PL intensity observed once the exciton energy had blueshifted, as the vacancies and defects created act as non-radiative recombination centres.

4.5.3 Further NWQD growth studies

In the following, two NWQD samples grown after Sample 4B are discussed. In Sample 4C, two NWQDs were grown sequentially during the same growth run, with the

fraction of indium varied between each NWQD[§]. PL measurements on these NWQDs acted as further proof that photon emission with energy below the GaAs bandgap was due to indium incorporation forming the NWQD. Sample 4D was a repeat of Sample 4B but grown some months later^{**}. The sample exhibited different growth characteristics, which led most notably to the observation of a power-dependent blueshift in PL emission from the NWQD.

4.5.3.1 Towards optically coupled NWQDs

The nanowire geometry presents an interesting opportunity for the growth of naturally aligned NWQDs which may be coupled by the optical mode(s) of the nanowire. Vertical alignment of this nature may be achieved for SK QDs, but without the optically-coupled aspect^{80,81}. The growth of multiple NWQDs within the same nanowire has also been suggested as a route to the realisation of an intermediate band solar cell⁷⁶. Additionally, the growth of multiple NWQDs in the same nanowire acts as further proof that the sharp line PL emission reported previously does indeed originate from an InGaAs NWQD. This is required as TEM imaging was unable to determine the location of the individual NWQD in the nanowires discussed earlier in this chapter. By growing two NWQDs in the same nanowire, the number of exciton lines observed in PL spectroscopy was seen to double.

Sample 4C consisted of nanowires containing two NWQDs grown sequentially. Growth was undertaken at 750°C following an annealing step at 780°C as described previously. Following 150s of GaAs growth, an InGaAs NWQD was grown for 2s. The two steps were then repeated, except the measured indium concentration was doubled the second

[§] Sample 4C corresponds to sample MR3068.

^{**} Sample 4D corresponds to sample MR3352.

time. Finally, 90s of GaAs growth was followed by 10s of GaAsP grown radially to cap the nanowire. The sample was cooled under a PH_3 overpressure. Flow rates of 33sccm and 30sccm for TMGa and AsH_3 respectively were used throughout except for the radial capping layer. The TMIn flow rates were 70sccm and 131sccm for the first and second NWQD respectively in a total flow of 250sccm. The TMIn flows gave measured concentrations of 0.012% and 0.025%. The increase in TMIn flow rate was intended to form a second NWQD with lower exciton energy than that of the first NWQD. For the GaAsP capping layer, the AsH_3 flow rate was increased to 150sccm, and PH_3 was added at 300sccm. A schematic of the nanowires can be seen in Figure 4.13(a). The growth of GaAs for 150s between the two NWQDs meant that they were both spatially and spectrally isolated from one another.

PL measurements were undertaken on the as-grown nanowires (vertical interrogation). In general interpreting the PL spectrum from nanowires containing two NWQDs was complicated due to overlap of the excited states of the different emitters. Figure 4.13(b) shows power dependent PL spectra from a single nanowire in which the NWQD emission was well resolved. Two exciton lines were observed, with associated excited states at higher pump power. From the growth conditions described above, the lower energy exciton was assigned to the NWQD which was grown with a higher TMIn flow. It was observed that despite the lower exciton energy NWQD being grown second (and therefore further up the nanowire), PL emission was first seen from the higher exciton energy NWQD. The mechanism behind this observation is unclear. The laser was focussed onto the substrate before moving onto each nanowire to take PL measurements. Given the small footprint of the nanowire relative to the laser spot size, it is possible that

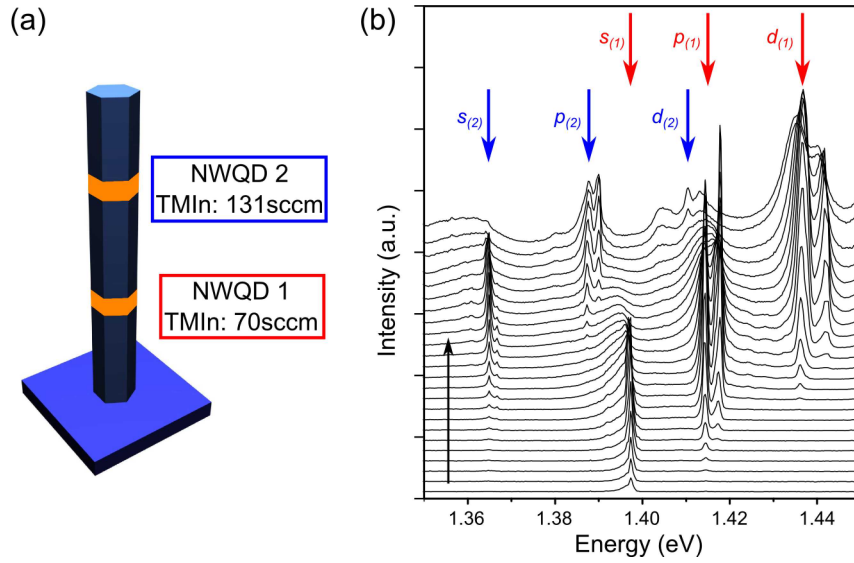


Figure 4.13. PL emission spectra from a nanowire containing two NWQDs. (a) Schematic of the nanowire, highlighting the relative position of the two NWQDs; (b) Power dependent PL spectra taken from a single nanowire. Spectra are offset in y for clarity. Two excitons can be observed (states $s_{(1)}$ and $s_{(2)}$), with associated excited states at higher laser pump power (states p and d). The black arrow denotes the direction of increasing laser power. Energy levels for each of the two NWQDs are separately labelled $l_{(i)}$, with $l=s,p,d$ and $i=1,2$ denoting the lower and upper NWQD respectively.

free carriers were created within the substrate and diffused to the lower NWQD more efficiently than the upper NWQD captured carriers from the surrounding nanowire. In future this could be investigated by knocking the nanowires over and taking PL measurements perpendicular to the growth axis, although this requires knowledge of the growth front end of the nanowire, as well as sufficient distance between the two NWQDs to allow for their optical resolution.

To develop optically coupled NWQDs in the same nanowire, it is necessary to control several aspects of the growth. Most importantly, the emission wavelength of each NWQD should be identical. This is a significant challenge, and is commonly addressed within SK QD samples simply by searching for QDs emitting at coincident energy. Whilst this is

more difficult when the QDs are formed within a single nanowire, varying the nanohole diameters across the sample would allow a range of NWQDs to be obtained in the same growth run, and therefore identifying similar NWQDs might be possible. Alternatively, a gate voltage could be applied to a single NWQD in the horizontal geometry, enabling tuning of the exciton energy. A further consideration is the distance between the NWQDs. For optical coupling this should be equal to $n\lambda_{\text{eff}}/2$ ($n=1,3,5\dots$) where λ_{eff} is the effective emission wavelength within the nanowire waveguide. This system could find application as a single photon switch, whereby the absorption in one NWQD is bleached by an external laser pulse allowing the passage of a photon from the other NWQD and detection at the nanowire end facet. In the absence of the external laser, the photon would instead be absorbed.

4.5.3.2 Blueshift of NWQD PL emission

In this section, the observation of a power dependent blueshift in the PL emission energy from InGaAs NWQDs is described. This behaviour was unusual in that it has been seen in only a single sample to date, despite the use of quite similar growth conditions for all samples. It is suggested that the blueshift was a result of the crystal structure of the particular nanowires under investigation.

Sample 4D was a repeat of Sample 4B, but grown some time later. Unlike for Sample 4B significant radial growth was observed, suggesting that as suspected the 500sccm AsH_3 single dilution channel mass flow controller was unable to consistently measure a 30sccm flow rate. Radial growth is often observed under higher V/III ratio growth conditions for catalyst-free nanowires, meaning the AsH_3 flow rate was most likely higher during this growth run than for Sample 4B. Due to radial growth the nanowires studied here had

diameters in the range 150–350nm, compared with the nanohole diameters of 66–172nm. Therefore the radial growth thickness was on the order of 40–90nm. The corresponding nanowire heights were 1.8–5.1 μ m. Using a linear growth rate approximation the height of the NWQDs therefore varied between 5.9nm and 16.7nm.

Power dependent PL measurements were undertaken with the sample installed in a helium flow cryostat. Individual nanowires were excited using a HeNe laser operating at 632.8nm. The laser was focussed onto the sample using a 50x objective lens with an NA of 0.42. The PL signal was collected using the same objective lens and passed to a 0.25m focal length spectrometer. The resulting PL intensity as a function of energy was recorded using a liquid nitrogen-cooled InGaAs CCD. Measurements were undertaken on the narrowest nanowires, namely those with 150nm diameter.

Low power PL measurements revealed broader exciton linewidths than for Samples 4A and 4B. This was most likely a result of the different radial growth rates observed for the respective samples, altering the conditions during NWQD formation. Typical linewidths greater than 1meV were observed. Furthermore, there was no evidence of biexciton emission. It is possible that this simply could not be resolved from the exciton emission.

At higher pump powers, several excited states were observed. For some nanowires, the excited states were seen to blueshift with increasing power, as shown in Figure 4.14. A blueshift of this type may be due either to the quantum confined Stark effect, or the formation of a type-II NWQD. In the former case, the strain-induced piezoelectric field in the (111)B direction of the GaAs/InGaAs/GaAs system results in band bending, decreasing the exciton energy at low excitation power^{82,83}. At higher excitation power the piezoelectric field would be screened by charge carriers, therefore increasing the exciton

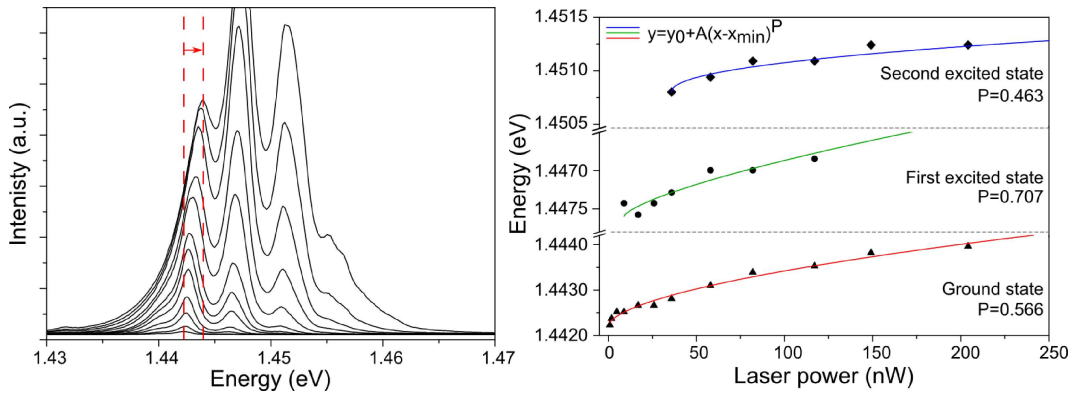


Figure 4.14. Observation of blueshift in power dependent PL measurements on NWQDs. (a) Power dependent PL spectra for a single NWQD. Red dashed lines highlight the change in energy of the ground state peak; (b) (Points) Energy versus pump power for the 3 lowest energy states of the NWQD in (a). Curves are power law fits to the data.

recombination energy by reducing the degree of band bending. An alternative explanation lies in the type-II bandstructure resulting from rotational twins within the nanowire. In previous samples the mean separation of rotational twins was ~ 2.7 nm. This meant that rotational twins may occur also within the NWQD, which has an axial length greater than 2.7 nm. The resulting spatial separation of the exciton hole and electron creates an electric field in the growth direction across the NWQD, leading to band bending. In this case band bending results in an increase of the exciton recombination energy, with further increases as the carrier population rises under increasing laser excitation.

The latter explanation is thought to be the more likely, given the previous observation of nanowire rotational twins and long PL lifetimes for the NWQD exciton, as well as the potential for strain relaxation in the nanowire geometry which may reduce any strain-induced electric fields. The variability in the degree of blueshift observed from nanowire to nanowire can be explained by the variability in the crystal structure in the vicinity of

the NWQD, whereas piezoelectric effects might be expected to be more uniform. Interestingly, the type-II structure found in polytypic nanowires provides confinement of both the electron and hole, unlike in common type-II QDs grown in a planar geometry, in which the Coulomb interaction may be dominant in localising the hole in the vicinity of the QD⁸⁴. It is unclear at this stage why a blueshift was only observed in a single sample given the expected presence of rotational twins in all the nanowire samples studied. Detailed TEM measurements might provide more insight in this regard.

The excitation power dependence of the PL emission energy from type-II QDs has been demonstrated in the literature to be of cube-root nature^{85,86}. Figure 4.14(a) shows a representative power dependent PL spectrum taken for a NWQD exhibiting a noticeable blueshift in energy levels. In Figure 4.14(b) the peak energies of the three lowest energy states of the NWQD are shown accompanied by a power law fit. Exponent values of 0.566, 0.707 and 0.463 were obtained for the ground state, first excited state and second excited state of the NWQD respectively. There is variation both within the exponents needed to fit the data, and also between the exponents and the value of 0.33 typically reported in the literature. The discrepancy may lie in the quite complicated bandstructure of the NWQD plus rotational twins system relative to the band alignment of more typical type-II QDs. Theoretical analysis of the power dependence would need to consider the multitude of potential bandstructure configurations for the NWQD.

4.6 Conclusion

The successful formation of InGaAs NWQDs in GaAs nanowires has been demonstrated. Extensive structural and optical characterisation of the NWQDs was undertaken, revealing properties consistent with the presence of a single NWQD within each GaAs nanowire. SEM and TEM analysis showed that the nanowires had a hexagonal cross-section and were uniform in diameter along their length. The nanowires grew with zinc blende crystal structure, containing rotational twins with a mean separation of 2.7nm. PL studies on an array of nominally identical nanowires revealed excitonic emission from individual NWQDs. The exciton emission had an ensemble broadening of $\sim 15\text{meV}$, comparing favourably with other reports of position controlled InGaAs QD growth within the literature. Exciton linewidths down to $140\mu\text{eV}$ have been measured, suggesting the presence of spectral diffusion effects, supported by repeated PL measurements on the same NWQD. Long PL lifetimes of $\sim 10.2\text{ns}$ and $\sim 6.5\text{ns}$ have been measured for the NWQD and the nanowire respectively. It is suggested that these were due either to the high density of rotational twins within the nanowires leading to type-II radiative recombination, or to suppression of NWQD PL emission due to the narrow nanowire diameter. The latter results in a weakly confined fundamental optical mode and therefore reduces the local density of optical states. Photon antibunching was observed within the emission from a single NWQD exciton, providing evidence for single photon emission from the NWQDs. At higher laser pump power discrete excited states were observed, and a model has been proposed to describe the observed state splitting. The combination of deterministic site control and PL emission homogeneity described provides a promising avenue for the growth of uniform, readily scalable single photon sources.

Bibliography

- (1) Marzin, J.-Y.; Gerard, J.-M.; Izrael, A.; Barrier, D.; Bastard, G. *Phys. Rev. Lett.* **1994**, *73*, 1–4.
- (2) Michler, P.; Kiraz, A.; Becher, C.; Schoenfeld, W. V.; Petroff, P. M.; Zhang, L.; Hu, E.; Imamoglu, A. *Science* **2000**, *290*, 2282–5.
- (3) Press, D.; Ladd, T. D.; Zhang, B.; Yamamoto, Y. *Nature* **2008**, *456*, 218–21.
- (4) Kroner, M.; Weiss, K.; Biedermann, B.; Seidl, S.; Manus, S.; Holleitner, A.; Badolato, A.; Petroff, P.; Gerardot, B.; Warburton, R.; Karrai, K. *Phys. Rev. Lett.* **2008**, *100*, 156803.
- (5) Young, R. J.; Stevenson, R. M.; Atkinson, P.; Cooper, K.; Ritchie, D. a; Shields, A. J. *New J. Phys.* **2006**, *8*, 29–29.
- (6) Akopian, N.; Lindner, N.; Poem, E.; Berlatzky, Y.; Avron, J.; Gershoni, D.; Gerardot, B.; Petroff, P. *Phys. Rev. Lett.* **2006**, *96*, 130501.
- (7) Ediger, M.; Dalgarno, P. A.; Smith, J. M.; Gerardot, B. D.; Warburton, R. J.; Karrai, K.; Petroff, P. M. *Appl. Phys. Lett.* **2005**, *86*, 211909.
- (8) Heindel, T.; Schneider, C.; Lermer, M.; Kwon, S. H.; Braun, T.; Reitzenstein, S.; Hoffling, S.; Kamp, M.; Forchel, A. *Appl. Phys. Lett.* **2010**, *96*, 011107.
- (9) Muller, A.; Flagg, E. B.; Bianucci, P.; Wang, X. Y.; Deppe, D. G.; Ma, W.; Zhang, J.; Salamo, G. J.; Xiao, M.; Shih, C. K. *Phys. Rev. Lett.* **2007**, *99*, 187402.
- (10) Yoshie, T.; Scherer, A.; Hendrickson, J.; Khitrova, G.; Gibbs, H. M.; Rupper, G.; Ell, C.; Shchekin, O. B.; Deppe, D. G. *Nature* **2004**, *432*, 9–12.
- (11) Khitrova, G.; Gibbs, H. M.; Kira, M.; Koch, S. W.; Scherer, A.; Marburg, D.-*Nat. Phys.* **2006**, *2*, 81–90.
- (12) Loss, D.; DiVincenzo, D. P. *Phys. Rev. A* **1998**, *57*, 120–126.
- (13) Bayer, M.; Forchel, A. *Phys. Rev. B* **2002**, *65*, 041308.
- (14) Flagg, E. B.; Muller, A.; Polyakov, S. V.; Ling, A.; Migdall, A.; Solomon, G. S. *Phys. Rev. Lett.* **2010**, *104*, 137401.
- (15) Mohan, A.; Gallo, P.; Felici, M.; Dwir, B.; Rudra, A.; Faist, J.; Kapon, E. *Small* **2010**, *6*, 1268–72.

-
- (16) Atkinson, P.; Kiravittaya, S.; Benyoucef, M.; Rastelli, A.; Schmidt, O. G. *Appl. Phys. Lett.* **2008**, *93*, 101908.
- (17) Song, H. Z.; Usuki, T.; Hirose, S.; Takemoto, K.; Nakata, Y.; Yokoyama, N.; Sakuma, Y. *Appl. Phys. Lett.* **2005**, *86*, 113118.
- (18) Hakkarainen, T. V.; Tommila, J.; Schramm, A.; Tukiainen, A.; Ahorinta, R.; Dumitrescu, M.; Guina, M. *Appl. Phys. Lett.* **2010**, *97*, 173107.
- (19) Dias, N. L.; Garg, A.; Reddy, U.; Young, J. D.; Verma, V. B.; Mirin, R. P.; Coleman, J. J. *Appl. Phys. Lett.* **2011**, *98*, 141112.
- (20) Skiba-Szymanska, J.; Jamil, A.; Farrer, I.; Ward, M. B.; Nicoll, C. A.; Ellis, D. J. P.; Griffiths, J. P.; Anderson, D.; Jones, G. a C.; Ritchie, D. A.; Shields, A. J. *Nanotechnology* **2011**, *22*, 065302.
- (21) Huggenberger, A.; Heckelmann, S.; Schneider, C.; Höfling, S.; Reitzenstein, S.; Worschech, L.; Kamp, M.; Forchel, A. *Appl. Phys. Lett.* **2011**, *98*, 131104.
- (22) Schneider, C.; Huggenberger, A.; Gschrey, M.; Gold, P.; Rodt, S.; Forchel, A.; Reitzenstein, S.; Höfling, S.; Kamp, M. *Phys. Status Solidi* **2012**, *209*, 2379–2386.
- (23) Pfau, T. J.; Gushterov, A.; Reithmaier, J. P.; Cestier, I.; Eisenstein, G.; Linder, E.; Gershoni, D. *Appl. Phys. Lett.* **2009**, *95*, 243106.
- (24) Abbarchi, M.; Troiani, F.; Mastrandrea, C.; Goldoni, G.; Kuroda, T.; Mano, T.; Sakoda, K.; Koguchi, N.; Sanguinetti, S.; Vinattieri, A.; Gurioli, M. *Appl. Phys. Lett.* **2008**, *93*, 162101.
- (25) Empedocles, S. A. *Science*. **1997**, *278*, 2114–2117.
- (26) Faure, S.; Nishioka, M.; Ishida, S.; Guimard, D.; Arakawa, Y. *Appl. Phys. Express* **2011**, *4*, 112001.
- (27) Singh, R.; Bester, G. *Phys. Rev. Lett.* **2009**, *103*, 063601.
- (28) Dorenbos, S. N.; Sasakura, H.; van Kouwen, M. P.; Akopian, N.; Adachi, S.; Namekata, N.; Jo, M.; Motohisa, J.; Kobayashi, Y.; Tomioka, K.; Fukui, T.; Inoue, S.; Kumano, H.; Natarajan, C. M.; Hadfield, R. H.; Zijlstra, T.; Klapwijk, T. M.; Zwiller, V.; Suemune, I. *Appl. Phys. Lett.* **2010**, *97*, 171106.
- (29) Minot, E. D.; Kelkensberg, F.; van Kouwen, M.; van Dam, J. A.; Kouwenhoven, L. P.; Zwiller, V.; Borgström, M. T.; Wunnicke, O.; Verheijen, M. A.; Bakkers, E. P. A. M. *Nano Lett.* **2007**, *7*, 367–71.

-
- (30) Dalacu, D.; Mnaymneh, K.; Wu, X.; Lapointe, J.; Aers, G. C.; Poole, P. J.; Williams, R. L. *Appl. Phys. Lett.* **2011**, *98*, 251101.
- (31) Tatebayashi, J.; Ota, Y.; Ishida, S.; Nishioka, M.; Iwamoto, S.; Arakawa, Y. *Appl. Phys. Lett.* **2012**, *100*, 263101.
- (32) Panev, N.; Persson, A. I.; Skold, N.; Samuelson, L. *Appl. Phys. Lett.* **2003**, *83*, 2238.
- (33) Kats, V. N.; Kochereshko, V. P.; Platonov, A. V.; Chizhova, T. V.; Cirlin, G. E.; Bouravleuv, A. D.; Samsonenko, Y. B.; Soshnikov, I. P.; Ubyivovk, E. V.; Bleuse, J.; Mariette, H. *Semicond. Sci. Technol.* **2012**, *27*, 015009.
- (34) Heinrich, J.; Huggenberger, A.; Heindel, T.; Reitzenstein, S.; Hofling, S.; Worschech, L.; Forchel, A. *Appl. Phys. Lett.* **2010**, *96*, 211117.
- (35) Borgström, M. T.; Zwiller, V.; Müller, E.; Imamoglu, A. *Nano Lett.* **2005**, *5*, 1439–43.
- (36) Bounouar, S.; Elouneq-Jamroz, M.; Hertog, M. Den; Morchutt, C.; Bellet-Amalric, E.; André, R.; Bougerol, C.; Genuist, Y.; Poizat, J.-P.; Tatarenko, S.; Kheng, K. *Nano Lett.* **2012**, *12*, 2977–81.
- (37) Renard, J.; Songmuang, R.; Tourbot, G.; Bougerol, C.; Daudin, B.; Gayral, B. *Phys. Rev. B* **2009**, *80*, 121305.
- (38) Reimer, M. E. Gaussian single photon emission from quantum dots in tapered nanowire waveguides. Presented at International Conference on One-Dimensional Nanomaterials, Annecy, France, 24th September **2013**.
- (39) Shapiro, J. N.; Lin, A.; Wong, P. S.; Scofield, A. C.; Tu, C.; Senanayake, P. N.; Mariani, G.; Liang, B. L.; Huffaker, D. L. *Appl. Phys. Lett.* **2010**, *97*, 243102.
- (40) Yang, L.; Motohisa, J.; Takeda, J.; Tomioka, K.; Fukui, T. *Appl. Phys. Lett.* **2006**, *89*, 203110.
- (41) Paladugu, M.; Zou, J.; Guo, Y.-N.; Zhang, X.; Kim, Y.; Joyce, H. J.; Gao, Q.; Tan, H. H.; Jagadish, C. *Appl. Phys. Lett.* **2008**, *93*, 101911.
- (42) Dick, K. A.; Bolinsson, J.; Borg, B. M.; Johansson, J. *Nano Lett.* **2012**, *12*, 3200–3206.
- (43) Dalacu, D.; Mnaymneh, K.; Lapointe, J.; Wu, X.; Poole, P. J.; Bulgarini, G.; Zwiller, V.; Reimer, M. E. *Nano Lett.* **2012**, *12*, 5919–23.
- (44) Bulgarini, G.; Reimer, M. E.; Zehender, T.; Hocevar, M.; Bakkers, E. P. A. M.; Kouwenhoven, L. P.; Zwiller, V. *Appl. Phys. Lett.* **2012**, *100*, 121106.

-
- (45) Perea, D. E.; Allen, J. E.; May, S. J.; Wessels, B. W.; Seidman, D. N.; Lauhon, L. J. *Nano Lett.* **2006**, *6*, 181–5.
- (46) Makhonin, M. N.; Foster, A. P.; Krysa, A. B.; Fry, P. W.; Davies, D. G.; Grange, T.; Walther, T.; Skolnick, M. S.; Wilson, L. R. *Nano Lett.* **2013**, *13*, 861–5.
- (47) Noborisaka, J.; Motohisa, J.; Fukui, T. *Appl. Phys. Lett.* **2005**, *86*, 213102.
- (48) Spirkoska, D.; Arbiol, J.; Gustafsson, A.; Conesa-Boj, S.; Glas, F.; Zardo, I.; Heigoldt, M.; Gass, M. H.; Bleloch, A. L.; Estrade, S.; Kaniber, M.; Rossler, J.; Peiro, F.; Morante, J. R.; Abstreiter, G.; Samuelson, L.; Fontcuberta i Morral, A. *Phys. Rev. B* **2009**, *80*, 245325.
- (49) Dick, K. A.; Caroff, P.; Bolinsson, J.; Messing, M. E.; Johansson, J.; Deppert, K.; Wallenberg, L. R.; Samuelson, L. *Semicond. Sci. Technol.* **2010**, *25*, 024009.
- (50) Novikov, B. V.; Serov, S. Y.; Filosofov, N. G.; Shtrom, I. V.; Talalaev, V. G.; Vyvenko, O. F.; Ubyivovk, E. V.; Samsonenko, Y. B.; Bouravleuv, A. D.; Soshnikov, I. P.; Sibirev, N. V.; Cirlin, G. E.; Dubrovskii, V. G. *Phys. Status Solidi - Rapid Res. Lett.* **2010**, *4*, 175–177.
- (51) IOFFE New Semiconductor Materials. Characteristics and Properties <http://www.ioffe.ru/SVA/NSM/> (accessed Jan 1, 2012).
- (52) Hafenbrak, R.; Ulrich, S. M.; Michler, P.; Wang, L.; Rastelli, A.; Schmidt, O. G. *New J. Phys.* **2007**, *9*, 315–315.
- (53) Treu, J.; Schneider, C.; Huggenberger, A.; Braun, T.; Reitzenstein, S.; Hofling, S.; Kamp, M. *Appl. Phys. Lett.* **2012**, *101*, 022102.
- (54) Heiss, M.; Conesa-Boj, S.; Ren, J.; Tseng, H.-H.; Gali, A.; Rudolph, A.; Uccelli, E.; Peiró, F.; Morante, J. R.; Schuh, D.; Reiger, E.; Kaxiras, E.; Arbiol, J.; Fontcuberta i Morral, A. *Phys. Rev. B* **2011**, *83*, 045303.
- (55) Akopian, N.; Patriarche, G.; Liu, L.; Harmand, J.-C.; Zwiller, V. *Nano Lett.* **2010**, *10*, 1198–201.
- (56) Demichel, O.; Heiss, M.; Bleuse, J.; Mariette, H.; Fontcuberta i Morral, A. *Appl. Phys. Lett.* **2010**, *97*, 201907.
- (57) Montazeri, M.; Fickenscher, M.; Smith, L. M.; Jackson, H. E.; Yarrison-rice, J.; Kang, J. H.; Gao, Q.; Tan, H. H.; Jagadish, C.; Guo, Y.; Zou, J.; Pistol, M.; Pryor, C. E. *Nano Lett.* **2010**, *10*, 880–886.
- (58) Hua, B.; Motohisa, J.; Kobayashi, Y.; Hara, S.; Fukui, T. *Nano Lett.* **2009**, *9*, 1–5.

-
- (59) Pelucchi, E.; Dimastrodonato, V.; Mereni, L. O.; Juska, G.; Gocalinska, A. *Curr. Opin. Solid State Mater. Sci.* **2012**, *16*, 45–51.
- (60) Shields, A. J. *Nat. Photonics* **2007**, *1*, 215–233.
- (61) Bleuse, J.; Claudon, J.; Creasey, M.; Malik, N. S.; Gérard, J.-M.; Maksymov, I.; Hugonin, J.-P.; Lalanne, P. *Phys. Rev. Lett.* **2011**, *106*, 103601.
- (62) Dubrovskii, V.; Sibirev, N.; Cirlin, G.; Bouravleuv, A.; Samsonenko, Y.; Dheeraj, D.; Zhou, H.; Sartel, C.; Harmand, J.; Patriarche, G.; Glas, F. *Phys. Rev. B* **2009**, *80*, 205305.
- (63) Kang, J. H.; Gao, Q.; Parkinson, P.; Joyce, H. J.; Tan, H. H.; Kim, Y.; Guo, Y.; Xu, H.; Zou, J.; Jagadish, C. *Nanotechnology* **2012**, *23*, 415702.
- (64) Ouattara, L.; Mikkelsen, A.; Sköld, N.; Eriksson, J.; Knaapen, T.; Cavar, E.; Seifert, W.; Samuelson, L.; Lundgren, E. *Nano Lett.* **2007**, *7*, 2859–64.
- (65) Patriarche, G.; Glas, F.; Tchernycheva, M.; Sartel, C.; Largeau, L.; Harmand, J.-C.; Cirlin, G. E. *Nano Lett.* **2008**, *8*, 1638–43.
- (66) Becher, C.; Kiraz, A.; Michler, P.; Imamoğlu, A.; Schoenfeld, W.; Petroff, P.; Zhang, L.; Hu, E. *Phys. Rev. B* **2001**, *63*, 121312.
- (67) Brouri, R.; Beveratos, A.; Poizat, J. P.; Grangier, P. *Opt. Lett.* **2000**, *25*, 1294–6.
- (68) Fox, M. *Quantum Optics: An Introduction*; Oxford University Press: Oxford.
- (69) Sallen, G.; Tribu, A.; Aichele, T.; Besombes, L.; Richard, M.; Tatarenko, S.; Kheng, K. *Phys. Rev. B* **2011**, *84*, 041405.
- (70) Sallen, G.; Tribu, A.; Aichele, T.; André, R.; Besombes, L.; Bougerol, C.; Richard, M.; Tatarenko, S.; Kheng, K.; Poizat, J.-P. *Nat. Photonics* **2010**, *4*, 696–699.
- (71) Joyce, H. J.; Gao, Q.; Tan, H. H.; Jagadish, C.; Kim, Y.; Zhang, X.; Guo, Y.; Zou, J. *Nano Lett.* **2007**, *7*, 921–6.
- (72) Alivisatos, A. P. *Science*. **1996**, *271*, 933–937.
- (73) Bouwes Bavinck, M.; Zieliński, M.; Witek, B. J.; Zehender, T.; Bakkers, E. P. a M.; Zwiller, V. *Nano Lett.* **2012**, *12*, 6206–11.
- (74) Malik, S.; Roberts, C.; Murray, R.; Pate, M. *Appl. Phys. Lett.* **1997**, *71*, 1987.

-
- (75) Mariani, G.; Wong, P.-S.; Katzenmeyer, A. M.; Léonard, F.; Shapiro, J.; Huffaker, D. L. *Nano Lett.* **2011**, *11*, 2490–4.
- (76) Tatebayashi, J.; Ota, Y.; Ishida, S.; Nishioka, M.; Iwamoto, S.; Arakawa, Y. *J. Cryst. Growth* **2013**, *370*, 299–302.
- (77) Rastelli, A.; Wang, L.; Kiravittaya, S.; Schmidt, O. *Int. Conf. Indium Phosphide Relat. Mater. (Conference Proceedings)* **2007**, 546–550.
- (78) Goldstein, B.; Szostak, D. J.; Ban, V. S. *Surf. Sci.* **1976**, *57*, 733–740.
- (79) Stanowski, R.; Dubowski, J. *J. Appl. Phys. A* **2008**, *94*, 667–674.
- (80) Zundel, M. K.; Specht, P.; Eberl, K.; Jin-Phillipp, N. Y.; Phillipp, F. *Appl. Phys. Lett.* **1997**, *71*, 2972.
- (81) Wasilewski, Z. R.; Fafard, S.; Mcca, J. P. *J. Cryst. Growth* **1999**, *202*, 1131–1135.
- (82) Chen, X.; Molloy, C. H.; Woolf, D. A.; Cooper, C.; Somerford, D. J.; Blood, P.; Shore, K. A.; Sarma, J. *Appl. Phys. Lett.* **1995**, *67*, 1393.
- (83) Smith, D. L. *Solid State Commun.* **1985**, *57*, 919–921.
- (84) Madureira, J. R.; de Godoy, M. P. F.; Brasil, M. J. S. P.; Iikawa, F. *Appl. Phys. Lett.* **2007**, *90*, 212105.
- (85) Alonso-Álvarez, D.; Alén, B.; García, J. M.; Ripalda, J. M. *Appl. Phys. Lett.* **2007**, *91*, 263103.
- (86) Kawazu, T.; Mano, T.; Noda, T.; Sakaki, H. *Appl. Phys. Lett.* **2009**, *94*, 081911.

5 Morphology control of GaAs nanowires

5.1 Introduction

GaAs nanowire structures offering new optical functionality have been developed by varying the EBL nanohole write patterns and MOCVD growth conditions for catalyst-free growth. By patterning arrays of nanohole pairs, nanoslots and extended groups of nanoholes, control of the resulting nanowire morphology has been achieved, including nanowire pairs separated by as little as $\sim 10\text{nm}$ and individual nanowires with elongated cross-section. InGaAs axial heterostructures grown within elongated nanowires were seen to emit strongly linearly-polarized light. This work presents a promising route for the investigation of optical coupling between NWQDs with tuned separation, and for the bottom-up growth of linearly polarized single photon sources. The latter is of particular interest for quantum information applications, reducing losses introduced by linear polarization optics. This work represents the first demonstration of bottom-up nanowire morphology control via the selective area growth technique.

In section 5.2 the EBL patterning and nanowire growth conditions used for the samples discussed in this chapter are presented. Morphological control of nanowires is the subject of section 5.3. One outcome of such control is the observation of linearly polarised light emission from the nanowire top facet, and future possibilities for formation of linearly polarised single photon emitters are evaluated.

5.2 Sample growth

In Chapters 3 and 4, nanowires were grown with a pitch of $4\mu\text{m}$, allowing for the optical interrogation of individual nanowires. In an extension of that EBL patterning scheme, square arrays of nanohole pairs were fabricated. Whilst the separation between each pair was maintained at $4\mu\text{m}$, the separation between the individual members of each pair was varied, from 0nm up to 200nm . This is shown schematically in Figure 5.1. Due to EBL patterning proximity effects, enlargement of the nanoholes was observed, which was particularly relevant for a nominal separation of zero as the resulting pair of holes then overlapped. For a nanohole nominally 100nm in diameter, a final nanohole diameter of $\sim 130\text{nm}$ was typically observed.

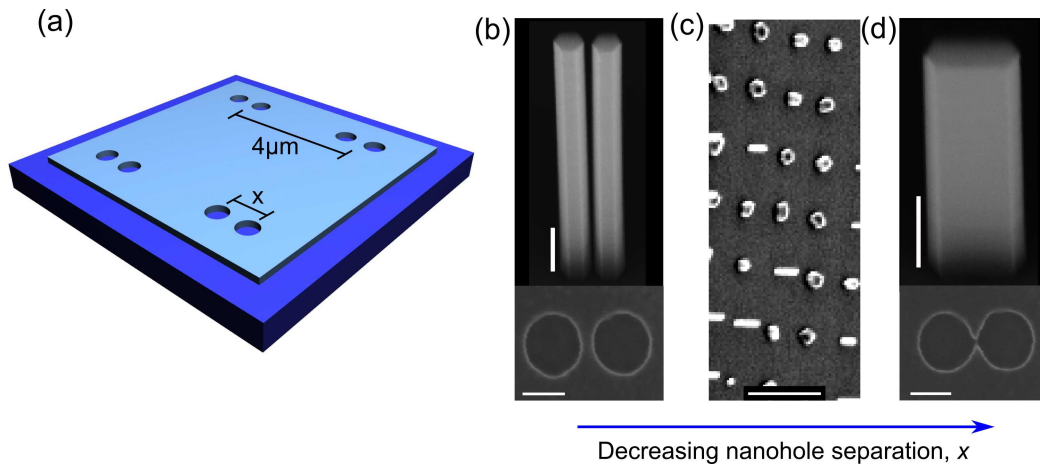


Figure 5.1. Investigation of growth from nanohole pairs. (a) Schematic of nanohole patterning scheme, $0\text{nm} < x < 200\text{nm}$; SEM images showing, in order of decreasing separation x , (b) paired nanowires, (c) unstructured nanowire growth and (d) a single nanowire with an elongated cross-section. (b), (d) (Lower panels) SEM images of the nanoholes from which the growth proceeded. Upper scale bars 200nm , lower scale bars 100nm . (c) Scale bar $5\mu\text{m}$.

Growth of Sample 5A* followed the scheme for Sample 4B discussed in Chapter 4, with the exception of the AsH₃ flow. A double dilution channel was used to allow an AsH₃ flow rate of 15sccm to be measured. This was intended to reduce the degree of radial growth relative to that seen for Sample 4C. It should be understood that the close proximity of the two nanowires altered the growth environment for each nanowire hence a comparison of individual and double nanowire heights and diameters is not strictly valid. The influence of proximity effects on catalyst-free nanowire growth is well known¹. Note that as for Sample 4B an InGaAs axial heterostructure was formed within the nanowires.

Using these growth conditions, under which radial nanowire growth was restricted (but not entirely eliminated), two different growth modes were observed. When the nanoholes constituting a pair were sufficiently far apart, a pair of nanowires was obtained, with separation down to ~10nm. This measurement was limited by the resolution of the SEM. A pair of nanowires grown in this manner is shown in Figure 5.1(b). The nanowires were ~2μm in height and ~190nm in diameter, corresponding to ~30nm of radial growth.

As the nanohole separation was decreased, the resulting growth initially became random, with a mixture of double nanowires and unstructured growth, as shown Figure 5.1(c). The latter was thought to occur when radial growth resulted in coalescence of the nanowire pair a significant time after the seeding of the nanowires.

Decreasing the nanohole separation further, however, lead to the suppression of individual nanowire growth. Instead the formation of single nanowires with an elongated cross-section was observed. An example of such a nanowire is shown in Figure 5.1(d).

* Sample 5A corresponds to Sample MR3352

An elongated nanowire was observed whenever the nanoholes overlapped on the growth mask, and also when they were just touching. In the latter case, it is thought that the initial pyramidal islands which formed within the nanoholes likely coalesced immediately upon development of the vertical nanowire facets, leading to a single nanowire rather than the random growth observed in Figure 5.1(c). The exact growth mechanism is the subject of on-going investigation within the research group. The elongated nanowires had a height of $\sim 1\mu\text{m}$. In the case of nanoholes orientated in the (011) direction (parallel to the major flat), the width of the nanowires in the direction orthogonal to a line through the nanohole pairs was governed by the nanohole diameter (plus radial growth), and was $\sim 180\text{nm}$. In the direction of elongation the width was a function of the nanohole separation, with a maximum of $\sim 300\text{nm}$. The volume of deposited material was therefore very similar for both a pair of nanowires in close proximity and a single elongated nanowire. Due to the development of $\{110\}$ facets during the growth, nanohole pairs orientated in the orthogonal direction had a smaller elongation ratio. This becomes clear in the following section.

5.3 Linearly polarized PL from an elongated nanowire

In this section, the polarization properties of photons emitted from InGaAs axial heterostructures formed in elongated cross-section nanowires are investigated. Photons are collected from the top facet of the nanowires. The results should therefore not be confused with the polarization anisotropy observed for emitted photons collected from the side facets of a nanowire².

5.3.1 Nanowire morphology control

There have been several reports to date concerning the *in-situ* control of nanowire morphology, for instance the formation of branched³ and ‘zigzag’ nanowire structures⁴. Suppression of natural tapering of VLS-grown InP nanowires has been demonstrated through the introduction of HCl into the reactor during growth⁵. More pertinently to the results discussed here, nanowire morphology control has been demonstrated through varying growth fluxes to achieve for instance quasi-rectangular nanowires^{6,7}. This was however dependent on the growth of a doped shell structure, in contrast to the growth technique developed here.

The earliest reports concerning catalyst-free nanowire growth discussed how the shape of the nanohole was seen to have no effect on the resulting nanowire morphology⁸. In that work, EBL patterning of the nanoholes using a hexagonal geometry resulted in circular nanoholes. This was due to a combination of EBL resolution limits and the etching process used to transfer the nanoholes from the EBL resist to the SiO₂ growth mask. However, the resulting nanowires were seen to have a hexagonal cross-section. This implied that given correct growth conditions, the nanowire cross-section was determined by the epitaxial and facet-led nature of the growth process, leading to defined hexagonal side facets. In the results reported here however, it is demonstrated that the initial nanohole geometry can in fact be used to influence the nanowire cross-section.

A competing approach to the fabrication of morphologically-variable nanowire-type structures involves top-down etching through a planar semiconductor wafer⁹⁻¹². A hard mask is patterned on the upper surface of the substrate, followed by the use of a strongly anisotropic etchant, resulting in pillar formation with cross-sectional geometry

determined by the initial mask dimensions. Potential pillar geometries are limited mainly by the mask and degree of etch anisotropy. A major downside of this process is the potential formation of etch damage on the pillar sidewalls, which may negatively influence the optical properties of the resulting structures through non-radiative recombination and spectral wandering effects.

Within the limits presented by the nanowire side facets, elliptical nanowires have been grown in this work. Figure 5.2 shows SEM images of two such nanowires, alongside schematics detailing the morphology of the constituent nanowires in each case. Due to the layer by layer nature of the growth process, the InGaAs axial heterostructure forms an elongated disk rather than the single point-like SK QDs used in Ref 13 and this could be expected to influence the optical properties of the emitter-nanowire system.

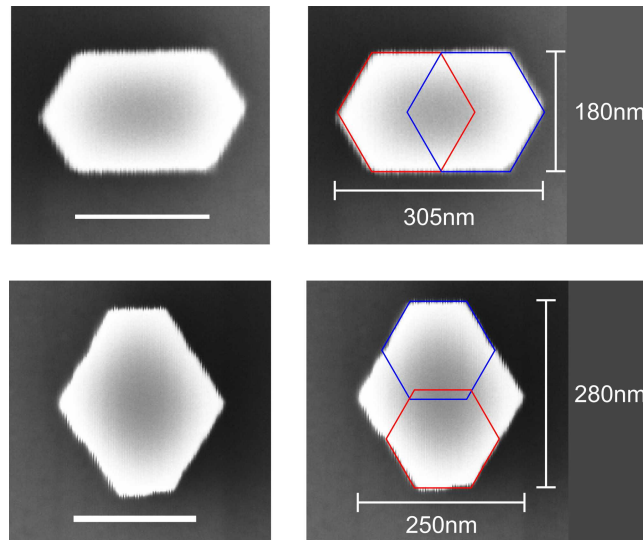


Figure 5.2. SEM images of elongated nanowires used for polarization measurements. Left hand panels show top down SEM images of the horizontally (top) and vertically (bottom) elongated nanowires. Right hand panels show the same SEM images overlaid with outlines of the two nanowires which would have formed had a single nanowire not been produced.

5.3.2 PL measurements

Polarization-dependent PL measurements were undertaken on a nanowire with normal hexagonal cross-section, and two nanowires with orthogonally elongated cross-sections (referred to here as NW: x and NW: y for the x and y elongated nanowires respectively). The dimensions of the nanowires are shown in Figure 5.2. The unpolarized low power PL emission from the InGaAs heterostructure grown within each nanowire is shown in the left hand panels of Figure 5.3(a) and Figure 5.3(b). In general the success rate for formation of an optically active InGaAs heterostructure was found to be low, suggesting the growth conditions should be changed in future. The ground state PL emission peaks from the elongated nanowires were relatively broad, on the order of several

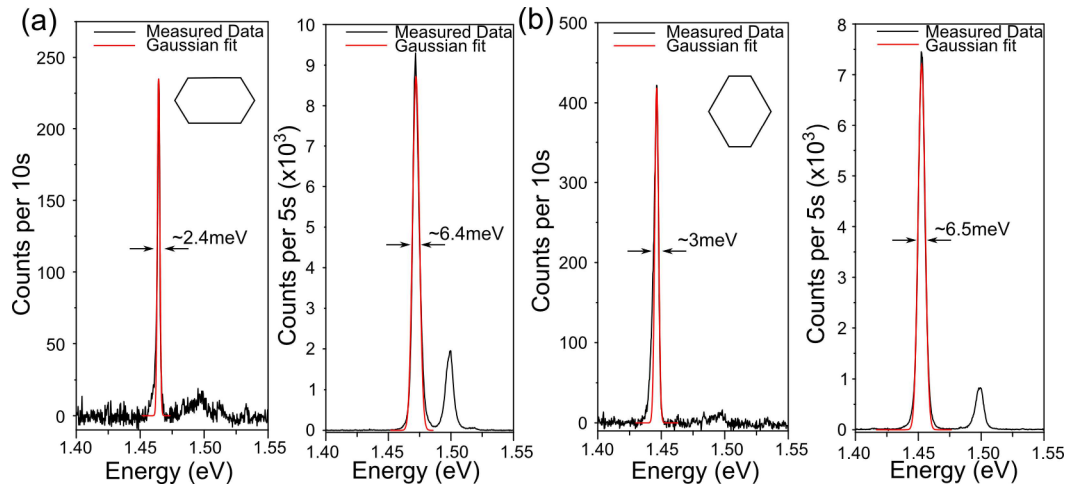


Figure 5.3. PL spectra from InGaAs heterostructures in elongated nanowires. (a) Unpolarized low power PL spectrum for a horizontally elongated nanowire (left hand panel) and higher power PL spectrum corresponding to the power used during polarization measurements; (b) As for (a) but for a vertically elongated nanowire.

millielectronvolts. This was potentially due to the radial dimensions of the nanowires, which made it more likely that a quantum well would be formed than a NWQD.

PL measurements were undertaken using HeNe laser excitation at 632.8nm, focussed onto a single nanowire in a helium flow cryostat through a microscope objective lens with an NA of 0.42. The PL signal was collected by the same objective lens and passed through a thin film linear polarizer before the signal was dispersed and accumulated using a combination of spectrometer and CCD. To account for any polarization sensitivity of the spectrometer, the polarized PL signal was rotated using a half-wave plate before the spectrometer to maximise the signal. To enable imaging of the sample surface and focussing of the laser on the sample, a fraction of the PL signal was usually directed to a camera via a beam splitter. The beam splitter was removed during the measurements as it was found to influence the measured PL polarization.

Linearly polarized PL spectra were obtained in 15 degree angular steps using a 5s accumulation time. At each angular step, the excitation laser spot was realigned onto the nanowire by maximising the signal on the CCD. This was necessitated by drift of the optical setup, and accounts for the scatter in the resulting data. Realignment of the laser on each nanowire was only possible at higher laser power (to obtain sufficient count rate in ~ 1 s) which resulted in additional broadening of each emission line. The broadened emission is shown in the right hand panels of Figure 5.3(a) and Figure 5.3(b). The resulting spectra were integrated over the range of wavelengths for which PL emission from the InGaAs region was observed, with the background count rate removed.

The polarization dependent intensity is plotted for the three different nanowire morphologies in Figure 5.4. It can be seen that emission from an InGaAs heterostructure

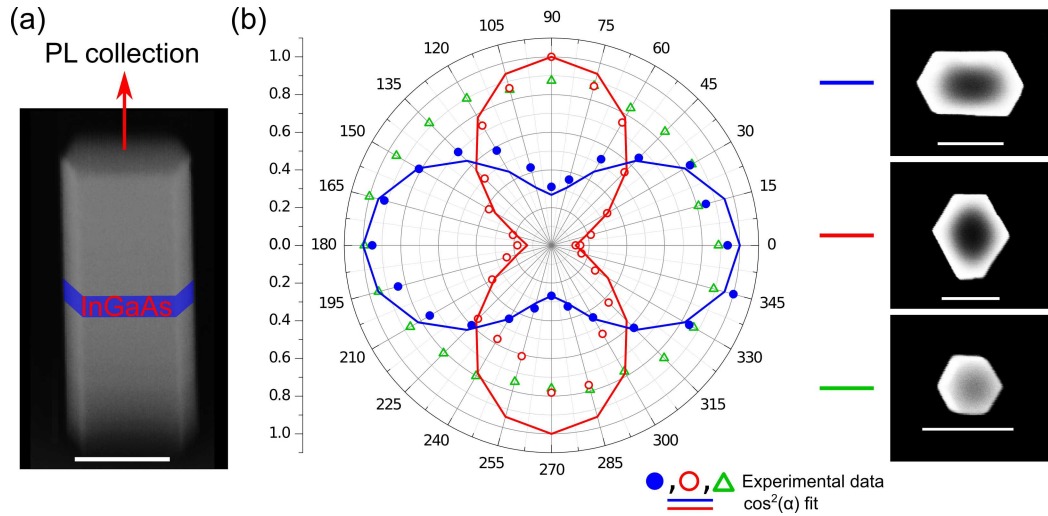


Figure 5.4. Polarization-dependent PL emission from InGaAs heterostructures in elongated nanowires. (a) Annotated SEM image showing the PL collection orientation. Scale bar 200nm; (b) Integrated PL intensity as a function of detection angle for horizontally (blue circles) and vertically (red circles) elongated nanowires, and a hexagonal cross-section nanowire (green triangles). Solid lines are $\cos^2(\alpha)$ fits to the data. Scale bars 200nm.

in a normal hexagonal nanowire was weakly polarized ($\sim 14\%$), whereas PL from the elongated nanowires was quite strongly linearly polarized. For the conventional hexagonal nanowire morphology the weak linear polarization was seen to vary from NWQD to NWQD. This has been observed previously in the case of InAsP NWQDs¹⁴. In the case of elongated nanowires, the axis of linear polarization was coincident with the elongation axis of the nanowire. The results are therefore in qualitative agreement with reports of polarization control in elliptical etched nanowires¹³, although as discussed later the origin of the polarization is uncertain. The degree of linear polarization can be characterised using the figure of merit $C_{||} = I_{max}/(I_{max} + I_{min})$, where I_{max} and I_{min} are the maximum and minimum integrated intensities, in this case observed at orthogonal polarization angles. For NW:x this ratio was 0.79 whilst for NW:y it was 0.89.

5.3.3 Origin of linear polarization

The optical modes supported by a waveguide can be described in terms of their dispersion, the deviation of the frequency-wavevector relationship from the linear relationship observed for light in a vacuum ($\omega = ck$, where ω is the angular frequency, c the speed of light and k the light wavevector). The dispersion is a result of the varying waveguide confinement experienced by different wavelengths of light. Each wavelength therefore experiences a different effective refractive index, resulting in differences in propagation velocity.

For a cylindrical GaAs nanowire in the single guided optical mode regime (diameter to wavelength ratio < 0.338 for an on-axis dipole) the fundamental guided mode of the nanowire is two-fold degenerate. The introduction of ellipticity in the cross-section of the nanowire lifts the fundamental mode degeneracy. Calculated fundamental mode dispersion relationships for an infinitely long cylindrical nanowire and elliptical nanowire are shown in Figure 5.5(a). The modes of the elliptical nanowire are x and y polarized, and were calculated using the MPB software¹⁵. Furthermore, a suitable choice of the semi-minor and semi-major axes of the elliptical nanowire may result in a significant difference in the relative confinement of the non-degenerate fundamental modes. By choosing a wavelength for which the mode polarized coincident with the elongation axis is well confined but the orthogonally polarized mode is excluded from the nanowire, preferential coupling of a dipole emitter into the former mode may be achieved. Modal electric field profiles for such a situation are shown in Figure 5.5(b) for a wavelength of 950nm. Enhancement of coupling into a single linearly polarized mode thus results in linearly polarized light emission from the end facet of the nanowire. The electric field

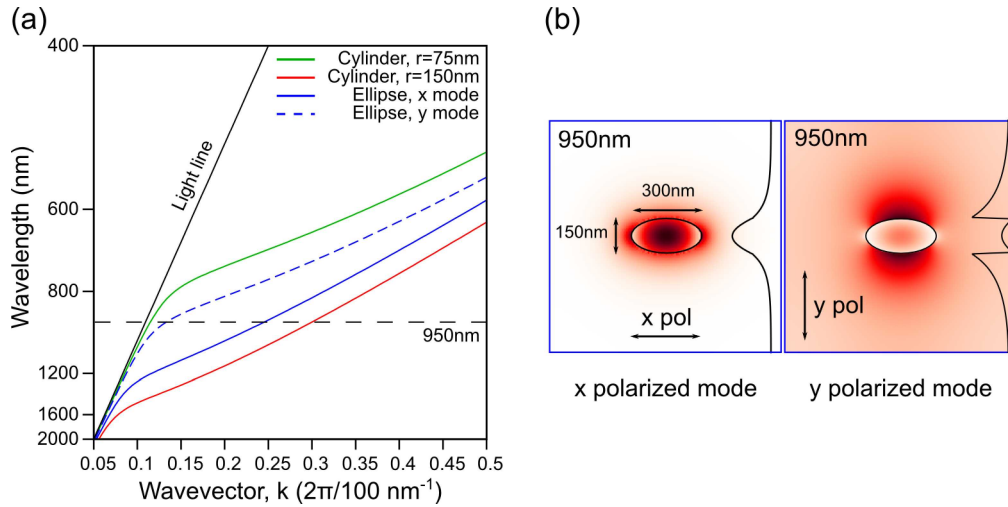


Figure 5.5. Fundamental mode analysis for circular and elliptical cross-section infinite waveguides. (a) Dispersion relation for waveguides with cylindrical cross-section (blue line, radius r and red line, radius $2r$) and elliptical cross-section with semi-minor axis of 75nm , semi-major axis of 150nm (x polarized mode blue line, y polarized mode blue dashed line); (b) Electric field cross-sections for the x and y polarized fundamental modes of the elliptical waveguide for $\lambda=950\text{nm}$. The fields are normalized such that $\int \epsilon |E_{x,y}|^2 = 1$, where the integral is taken over the infinite plane perpendicular to the nanowire axis and $\epsilon=11.9$ is the relative dielectric permittivity. The trace to the right of each plot gives the electric field through the centre of each ellipse in the y direction.

strength of the fundamental mode is greatest at the nanowire axis, and a quantum emitter placed at this location will couple most efficiently to the relevant mode.

As mentioned previously, the experimental realisation of linearly polarized single photon sources leveraging the physics described above has been reported for the case of etched nanowires¹³. By using a top-down approach the QDs could be grown by standard techniques (e.g. SK growth by MBE) resulting in high quality optical properties. The distance between the QD layer and the base of the resulting etched nanowires could also be tailored, allowing a distributed Bragg reflector or equivalent to be used to enhance

vertical PL emission from the nanowire (and hence measured count rates). However, the radial position of the QD within the nanowire is difficult to control, reducing the likelihood of efficient coupling to the fundamental optical mode. Surface damage induced by the etching process can also have a negative effect on the photon emission rate.

In contrast, bottom-up growth of NWQDs naturally leads to the formation of an on-axis emitter. The development of facets perpendicular to the substrate influences the achievable nanowire morphologies, and a cylindrical nanowire cannot be obtained. However, the hexagonal morphology of a nanowire lifts the degeneracy of the fundamental mode only slightly. This can be seen in the dispersion relation in Figure 5.6(a), which compares the modes for a hexagonal nanowire and the cylindrical approximation.

The upper panels in Figure 5.6(b) and Figure 5.6(c) show the corresponding dispersion relations for the optical modes of NW: x and NW: y , in which a larger splitting of the modes can be observed due to the increased shape anisotropy. Whilst the degeneracy is lifted, there is no optical bandgap, and an on-axis emitter at a suitable wavelength can couple to both modes, simply at a different momentum vector. Mode profiles for a dipole emission wavelength of $\sim 850\text{nm}$ are shown in Figure 5.6(b) for NW: x and Figure 5.6(c) for NW: y .

The measured polarization ratios are higher than might be expected if the observed polarization was due simply to the anisotropic cross-section of the nanowire, leading to preferential coupling of the PL emission to a single linearly-polarized optical mode. This is because the degree of shape anisotropy is fairly low for NW: x and NW: y . For the case of an elliptical cylinder with an elongation ratio of 2 (as reported in Ref 13) containing

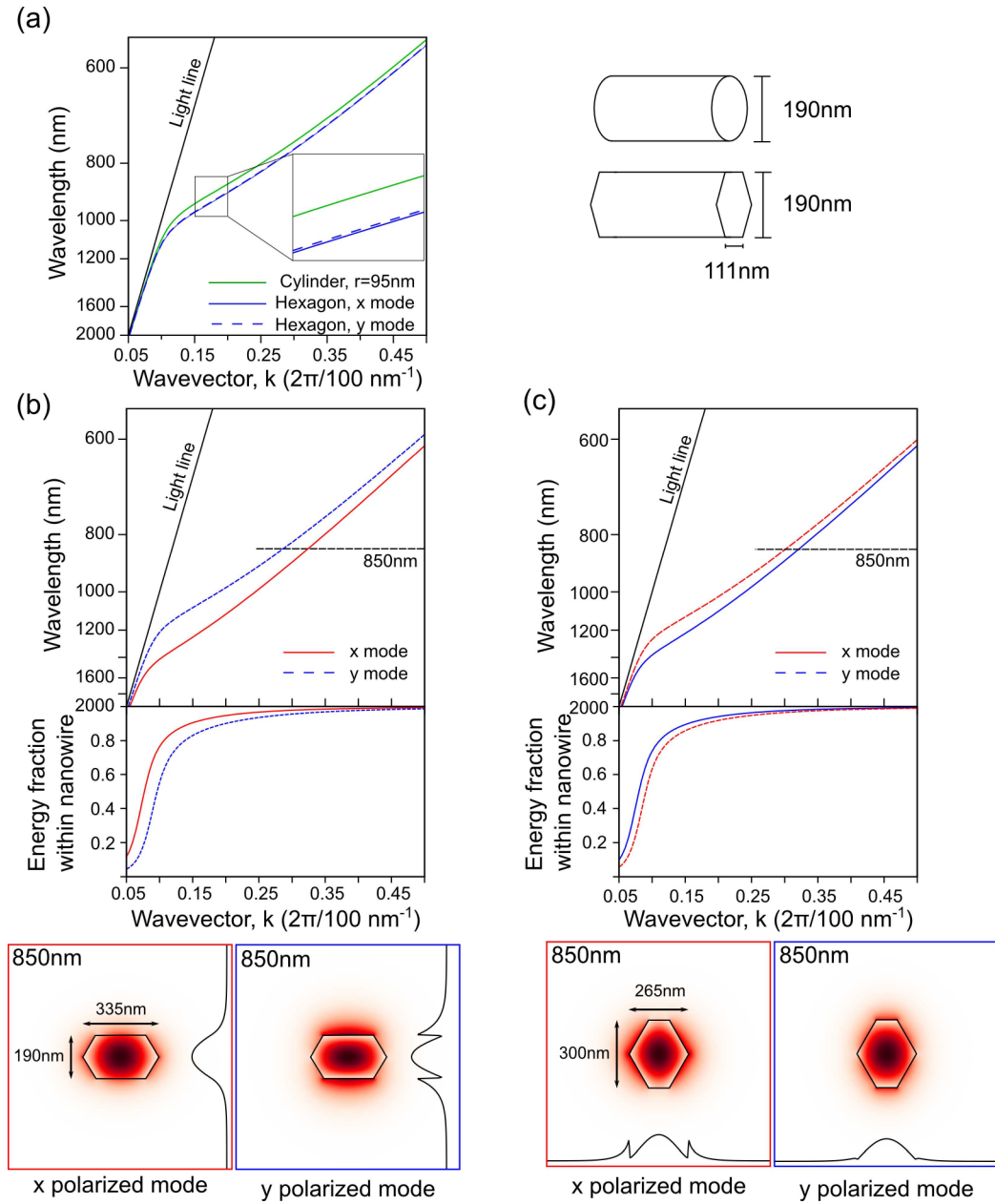


Figure 5.6. Nanowire optical mode analysis. (a) Dispersion relationships for the fundamental optical modes of hexagonal and cylindrical nanowires. Dimensions for the nanowire cross-sections are given to the right of the figure. (Inset) The fundamental mode is seen to be weakly non-degenerate in the hexagonal case; (b) (Upper panel) Dispersion relationship for the fundamental optical modes of the horizontally elongated nanowire measured in this work. (Middle panel) Mode energy confinement to the nanowire as a function of wavevector for the fundamental modes. (Lower panels) Normalized electric field intensity for each of the two linearly polarized fundamental modes at a wavelength of 850nm . A cross-section of the electric field through the centre of the nanowire is shown in on each plot; (c) As for (b) but for the vertically elongated nanowire.

QDs emitting at 950nm, there is a clear distinction between the electrical field strengths of the x and y polarized modes at the centre of the nanowire, as shown in Figure 5.5(b). In the case of the current work, the difference in the electrical field strengths is less evident. The modes are both well confined due to the larger dimension in the non-elongated direction, and the shorter operating wavelength. The fraction of the mode energy contained within the nanowire itself provides a measure of the confinement of the mode to the nanowire. This is shown in the lower panels of Figure 5.6(b) and Figure 5.6(c). At 850nm the confinement fractions are 0.98 and 0.95 for the x and y polarized modes of NW: x respectively. For NW: y the fractions are 0.98 and 0.96 for the y and x polarized modes respectively. In comparison, for elliptical nanowires with cross-section axis lengths of 300nm and 150nm, the difference in confinement of the two modes is much more pronounced at 950nm, being 0.95 and 0.47 for the x and y polarized modes (assuming elongation in the x direction). Whilst these values do not fully account for the relative coupling strength of an emitter to each mode, they demonstrate that the explanation for polarized PL emission presented in Ref 13 does not appear to quantitatively explain the results presented here.

In contrast to single mode coupling leading to linearly polarized PL emission, it is possible that the experimental observations reveal the intrinsic properties of the InGaAs heterostructures rather than a modification of these due to the surrounding environment. Linearly polarized PL emission has been observed previously in the case of quantum dashes, formed from elongated QDs¹⁶. In the current case, the InGaAs heterostructures are expected to be elongated, and this may influence their optical properties. However, the ability to control the polarization through the waveguide geometry is more appealing, and with this in mind the growth scheme was developed as discussed in the following section.

5.3.4 Extending the growth concept

In order to obtain a better understanding of the physical limits on formation of elongated nanowires, a further sample (Sample 5B[†]) was grown using a substrate which was patterned with more seeding geometries. As before pairs of nanoholes were formed in vertical and horizontal orientations, but also in a 60° line (due to the natural alignment of the hexagonal nanowires in this orientation). In addition, pairs of nanoholes were replaced with single elongated nanoslots, also with 0°, 60° and 90° orientations. In order to increase the height of the elongated nanowires compared to those of Sample 5B, the growth times were adjusted slightly. After annealing the sample at 780°C under an AsH₃ overpressure, 8 minutes of GaAs growth was followed by 3s of InGaAs and 7 minutes of GaAs growth. The TMGa flow was 33sccm and the AsH₃ flow was 30sccm throughout. A TMIn flow during NWQD growth of 40sccm in a total flow of 250sccm gave a measured concentration of 0.02%. The sample was cooled from the growth temperature of 750°C under a combined AsH₃ (30sccm) and PH₃ (300sccm) overpressure.

Representative SEM images for Sample 5B are shown in Figure 5.7. In the case of nanohole pairs, it can be seen that the 60° pairs did indeed lead to the formation of a single elongated nanowire. However, as previously the elongation ratio was limited by the maximum separation which produced a single nanowire rather than separate nanowires. On the other hand, it was found that nanoslots overcame this limitation, and the elongation ratio in this case was potentially much greater. Due to an issue with the reactor the actual realised TMIn flow rate during the NWQD growth was likely much lower than measured, and this was borne out by the lack of NWQD PL emission from this sample. The sample growth will be repeated in the future to evaluate the polarization properties of more strongly elongated nanowires.

[†] Sample 5B corresponds to Sample MR3436

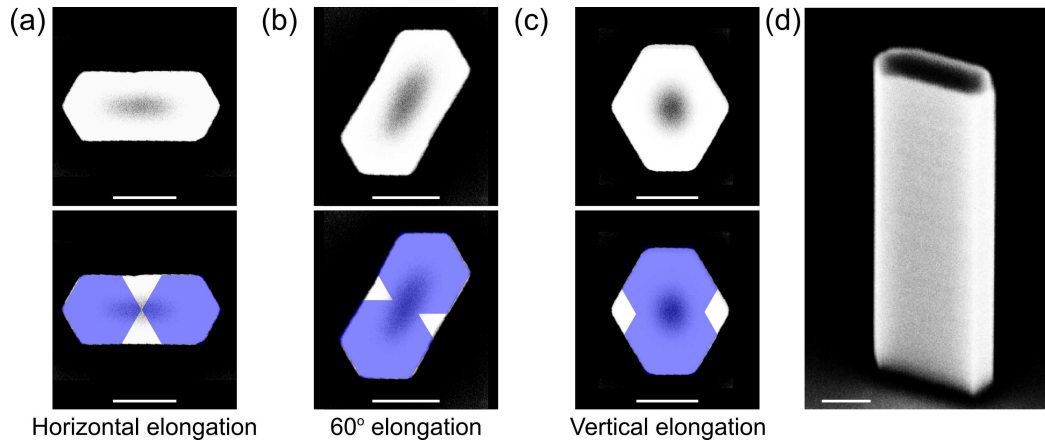


Figure 5.7. SEM images of elongated nanowires grown from nanoslots. (Top panels) Top down SEM images of (a) horizontally (b) 60° and (c) vertically elongated nanowires. (Bottom panels) SEM images overlaid with two hexagons highlighting regions of extra growth compared with separate nanowires; (d) 45° tilted SEM image of a horizontally elongated nanowire. Scale bars 200nm.

5.3.5 Limits on nanowire elongation for single mode coupling

In the case of linear polarization resulting from selective excitation of a linearly polarized waveguide mode, the QD grown within the nanowire should ideally be of limited radial extent. This would ensure both strong confinement of carriers within the NWQD and enhanced coupling of the emission into the optical mode. The radial dimensions of catalyst-free NWQDs have a minimum governed by growth considerations. To achieve linearly polarized emission at $\sim 900\text{nm}$, the final nanowire should have an elongated cross-section with a major axis of $\sim 300\text{nm}$ and minor axis of $\sim 150\text{nm}$ or smaller.

However, simply patterning the SiO_2 growth mask with holes 150nm in diameter and centre to centre separation of 150nm (or a slot of similar dimensions) would prevent realisation of a NWQD, as the length scales would be too great. This would instead be a

valid approach to the development of an axial quantum well with elongated cross-section. Considering a minimum realistic nanowire diameter of $\sim 30\text{nm}$, it is possible to form a nanowire containing a NWQD with dimensions of, for example, $\sim 30\text{nm}$ by $\sim 60\text{nm}$. However, radial growth of $\sim 240\text{nm}$ thickness to increase the largest dimension to $\sim 300\text{nm}$ would lead to a nanowire with narrowest dimension of $\sim 270\text{nm}$. This assumes that the radial growth rate is equal on all the side facets of the nanowire. The resulting nanowire cross-section would be insufficiently anisotropic to play a role in determining the PL polarization. This situation is shown schematically in Figure 5.8(a).

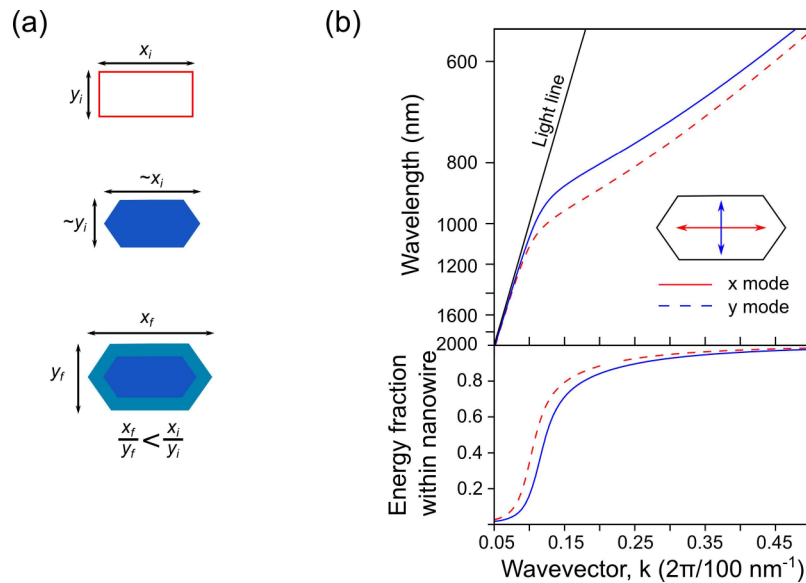


Figure 5.8. Growth considerations for nanowire morphology control. (a) Schematic representation of the limits on nanowire elongation possible when attempting to minimise the NWQD radial dimensions. The nanoslot dimensions (top) translate approximately to the nanowire core dimensions, and therefore the NWQD radial dimensions (middle). Isotropic radial overgrowth to strongly confine a single mode to the nanowire core reduces the elongation ratio (bottom); (b) (Top panel) Dispersion relationship for the fundamental optical modes of an elongated nanowire with radial dimensions 220nm by 150nm . This is a compromise between reducing the size of the NWQD and increasing the elongation ratio required to produce strongly linearly polarized PL emission. (Bottom panel) Fraction of mode energy confined to the nanowire as a function of wavevector.

A compromise would most likely involve patterning a slot with dimensions of $\sim 30\text{nm}$ by $\sim 100\text{nm}$ within the SiO_2 growth mask. From Chapter 4 it seems likely that a NWQD can be realised in a structure with these dimensions. By completing 120nm of radial growth a resulting elongation of 220nm by 150nm could be achieved. Figure 5.8(b) shows the resulting mode confinement for an emission wavelength of 900nm . The energy confinement of each mode to the nanowire is 86% and 60% for the x and y polarized modes respectively. The polarization ratio could therefore be expected to be similar to that achieved using elliptical etched nanowires. It would however be reduced somewhat due to the finite spatial extent of the InGaAs heterostructure.

An alternative approach would be to use a combination of catalysed and catalyst-free growth. Whilst this risks potential catalyst contamination of the NWQD, it provides a promising route to form a small, well confined NWQD followed by selective area catalyst-free growth of an elongated nanowire shell. The proposed growth method is shown schematically in Figure 5.9. Nanoslots are first patterned into the SiO_2 growth mask. A catalyst (for instance gold) is then deposited in the nanoslots. The challenge at this stage would be to place the catalyst at the centre of the nanoslots, so the resulting NWQD is on the final nanowire axis. Growth could then proceed using the VLS growth mode, forming a NWQD whose radial dimensions are governed by the catalyst particle diameter. By changing the growth conditions, the VLS growth mode can be replaced by the catalyst-free growth mode, allowing radial capping of the nanowire. It is posited that correct choice of growth conditions would allow the capping morphology to be determined by the nanoslot dimensions, and therefore the realization of an elongated nanowire containing a well-confined on-axis NWQD. A particularly appealing aspect of the proposed growth scheme is that elongation of the NWQD may be eliminated,

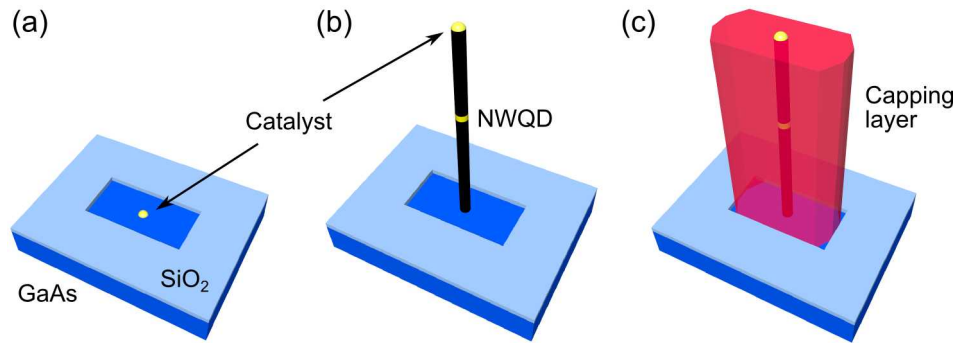


Figure 5.9. Schematic proposal for combined VLS and catalyst-free growth of elongated nanowires. (a) A catalyst particle is placed at the centre of a nanoslot within the SiO₂ growth mask; (b) A nanowire is grown using the VLS growth mode, containing a NWQD; (c) Using the catalyst-free growth mode, radial growth is promoted to form an elongated nanowire containing an on-axis NWQD.

maximising coupling of photon emission to the fundamental optical mode of the nanowire. Combined VLS/selective-area growth in this manner (without elongation) has been reported elsewhere¹⁷.

5.4 Conclusion

Nanowire morphology control has been demonstrated for the first time using the catalyst-free growth technique. By patterning two nanoholes in reducing proximity, the growth was seen to change from the formation of two separate nanowires to the development of single nanowires with an elongated cross-section, the elongation direction being determined by the orientation of the nanoholes. In the former growth regime, the nanowire separation could be finely controlled down to a separation of ~10nm (SEM resolution limited). In the elongated growth regime, nanowires were grown with elongations of 0°, 60° and 90° relative to the (011) direction. PL emission from an

InGaAs axial heterostructure within an elongated nanowire and collected from the nanowire top facet was shown to be linearly polarized. The axis of polarization was coincident with the axis of nanowire elongation. Preferential excitation of a single linearly polarized optical mode was investigated as the possible origin of the linearly polarized emission. This was found to provide a qualitative rather than quantitative explanation of the results. There remains the possibility that the PL polarization is an intrinsic property of the InGaAs heterostructure within these nanowires.

Bibliography

- (1) Noborisaka, J.; Motohisa, J.; Fukui, T. *Appl. Phys. Lett.* **2005**, *86*, 213102.
- (2) Wang, J.; Gudiksen, M. S.; Duan, X.; Cui, Y.; Lieber, C. M. *Science* **2001**, *293*, 1455–7.
- (3) Cheng, C.; Fan, H. J. *Nano Today* **2012**, *7*, 327–343.
- (4) Tian, B.; Xie, P.; Kempa, T. J.; Bell, D. C.; Lieber, C. M. *Nat. Nanotechnol.* **2009**, *4*, 824–9.
- (5) Borgström, M. T.; Wallentin, J.; Trägårdh, J.; Ramvall, P.; Ek, M.; Wallenberg, L. R.; Samuelson, L.; Deppert, K. *Nano Res.* **2010**, *3*, 264–270.
- (6) Kim, S.-K.; Day, R. W.; Cahoon, J. F.; Kempa, T. J.; Song, K.-D.; Park, H.-G.; Lieber, C. M. *Nano Lett.* **2012**, *12*, 4971–6.
- (7) Kempa, T. J.; Day, R. W.; Kim, S.-K.; Park, H.-G.; Lieber, C. M. *Energy Environ. Sci.* **2013**, *6*, 719.
- (8) Akabori, M.; Takeda, J.; Motohisa, J.; Fukui, T. *Nanotechnology* **2003**, *14*, 1071–1074.
- (9) Henry, M. D.; Walavalkar, S.; Homyk, A.; Scherer, A. *Nanotechnology* **2009**, *20*, 255305.
- (10) Chen, K.; He, J.-J.; Li, M.-Y.; Lapierre, R. *Chinese Phys. Lett.* **2012**, *29*, 036105.
- (11) Jalabert, L.; Dubreuil, P.; Carcenac, F.; Pinaud, S.; Salvagnac, L.; Granier, H.; Fontaine, C. *Microelectron. Eng.* **2008**, *85*, 1173–1178.
- (12) Varoutsis, S.; Laurent, S.; Sagnes, I.; Lemaître, a.; Ferlazzo, L.; Mériadec, C.; Patriarche, G.; Robert-Philip, I.; Abram, I. *J. Vac. Sci. Technol. B Microelectron. Nanom. Struct.* **2005**, *23*, 2499.
- (13) Munsch, M.; Claudon, J.; Bleuse, J.; Malik, N. S.; Dupuy, E.; Gérard, J.-M.; Chen, Y.; Gregersen, N.; Mørk, J. *Phys. Rev. Lett.* **2012**, *108*, 077405.
- (14) Van Weert, M. H. M.; Akopian, N.; Kelkensberg, F.; Perinetti, U.; van Kouwen, M. P.; Rivas, J. G.; Borgström, M. T.; Algra, R. E.; Verheijen, M. A.; Bakkers, E. P. A. M.; Kouwenhoven, L. P.; Zwiller, V. *Small* **2009**, *5*, 2134–8.
- (15) Johnson, S.; Joannopoulos, J. *Opt. Express* **2001**, *8*, 173.

- (16) Yuan, J.; Wang, H.; Veldhoven, R. P. J. Van; Wang, J.; Vries, T. De; Smalbrugge, B.; Jin, C. Y.; Nouwens, P.; Geluk, E. J.; Silov, A. Y. *Appl. Phys. Lett.* **2011**, *201904*, 2011–2014.

- (17) Dalacu, D.; Mnaymneh, K.; Wu, X.; Lapointe, J.; Aers, G. C.; Poole, P. J.; Williams, R. L. *Appl. Phys. Lett.* **2011**, *98*, 251101.

6 Growth and characterisation of InP nanowires

6.1 Introduction

InP has several potential advantages with respect to GaAs which make it appealing for use as the host for NWQDs. As discussed in Chapter 4, control of rotational twin formation in GaAs nanowires grown by the catalyst-free technique has yet to be demonstrated within the literature. Rotational twins negatively influence the optical properties of NWQDs¹ and should therefore be eliminated where possible. On the other hand, pure phase InP nanowires grown by the catalyst-free technique have already been reported², as well as a single report of InAsP NWQD formation³, although the two were not simultaneously realised. Using the VLS growth technique InAsP NWQDs in polytypic nanowires⁴ and pure phase nanowires¹ have been demonstrated. The latter led to ‘ultraclean’ photon emission with narrow PL linewidths of $\sim 30\mu\text{eV}$. Allied with the low surface recombination velocity (SRV) of InP nanowires⁵ which may reduce non-radiative surface recombination and therefore increase NWQD photon emission rates, there exists an opportunity to develop catalyst-free InAsP NWQDs with superior optical properties relative to the InGaAs material system. This would develop the field beyond the single report of catalyst-free InAsP NWQDs to date³, as there was no evidence of stacking fault control in that work. The low SRV for InP and the room temperature bandgap of $\sim 1.34\text{eV}$ also makes it well suited to the formation of nanowire solar cells

(see Chapter 2). Research into InP nanowire solar cells has already begun and has led to the most efficient nanowire solar cell (~13.8%) reported to date⁶.

With the above applications in mind, the growth and optical characterisation of InP nanowires has been initiated. In section 6.2 wafer preparation prior to growth is discussed. Section 6.3 covers the growth, electron microscopy and PL analysis of InP nanowires. Finally, conclusions and potential future directions are discussed in section 6.4.

6.2 Sample fabrication

InP substrates were prepared for nanowire growth in a very similar manner to that described in section 3.3 for GaAs substrates. To avoid repetition, only the notable differences in the fabrication route for InP will be described in the following.

Fabrication prior to growth of InP nanowires began with a 2 inch diameter (111)A n-type InP wafer. The choice of substrate orientation was motivated by a report in the literature regarding the vertical growth of InP catalyst-free nanowires⁷. In that work homogeneous growth of InP nanowires on (111)B substrates was found to form non-vertical structures orientated along the [111]A crystal directions, suggesting a preference for the latter orientation.

To aid later alignment in the EBL machine, markers were patterned on the wafer using photolithography as described in section 3.3.1. However, instead of etching the markers directly into the wafer (as undertaken on GaAs wafers), metal markers were deposited instead. This was due to difficulties encountered in determining a suitable etchant chemistry for (111)A InP. Given the distance on the wafer from the gold markers to areas

to be patterned for nanowire growth (at least 1mm and in general significantly more) the markers were considered unlikely to influence nanowire growth.

Photolithography followed by BPRS100 resist development for 60s in 3:1H₂O:PLSI led to the formation of the markers within the resist. The wafer was ashed in an oxygen plasma for 15s to remove residual resist from the exposed and developed areas, then loaded into a metal evaporator. Approximately 5nm of titanium was evaporated onto the wafer, followed by ~50nm of gold. Titanium was used to improve the adhesion of gold to the exposed InP surface. The deposited thicknesses were measured by monitoring the oscillation frequency of a quartz crystal placed alongside the InP wafer. After being unloaded from the evaporator, the substrate was placed in a beaker of warmed EKC830 until all photoresist was removed from the substrate surface. In so doing, any metal attached to the resist was also removed. The final result was that metal markers were left on the InP surface, their location defined by the photolithography mask. This process is described schematically in Figure 6.1.

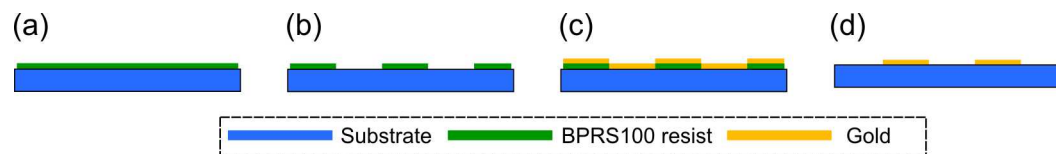


Figure 6.1. Definition of gold markers on an InP substrate. (a) BPRS100 resist is spun onto the substrate; (b) Photolithography is used to remove selected regions of resist from the substrate surface; (c) Titanium and gold are evaporated onto the surface; (d) The remaining resist is removed using EKC830, thus removing any gold attached to it and leaving behind gold in the regions exposed during photolithography.

Deposition of $\sim 30\text{nm}$ of SiO_2 by PECVD was then undertaken in the manner described in section 3.3.2. Due to earlier difficulties in obtaining reproducible growth of GaAs nanowires as a result of variable surface growth (see Chapter 3), it was decided to undertake growth with the substrate entirely covered by the SiO_2 growth mask to eliminate this risk. In this case, very little growth would be expected away from the nanoholes patterned within the growth mask, and growth was therefore expected to be more reproducible. The impact of this decision on growth rates is discussed in section 6.3. A second lithography step was therefore used simply to pattern markers into the SiO_2 layer which could be used to navigate the sample within the PL setup. The markers were transferred into the SiO_2 layer using a 30s etch in 1% HF solution, followed by a DIW rinse.

After spinning PMMA resist onto the sample development of nanohole arrays in the SiO_2 growth mask was undertaken as described in section 3.3.4, using a combination of EBL and RIE techniques. As this was the first attempt at growing InP nanowires in the MR350 reactor and growth conditions were unknown, nanohole arrays were patterned covering a wide range of pitches. Due to the use of a full coverage of SiO_2 , edge effects were anticipated, where nanowires at the side of an array grow faster due to lower competition for adatoms which diffuse inwards from the surrounding growth mask. To investigate these larger arrays were patterned than previously for GaAs. 100nm diameter nanoholes were patterned in arrays of side length $400\mu\text{m}$, for pitches of 1, 2, 3 and $4\mu\text{m}$. Nanoholes were also patterned with a pitch of $0.5\mu\text{m}$, the side length of the array in this case being $200\mu\text{m}$. After the etching process, the final nanoholes were typically seen to have a diameter of $\sim 130\text{nm}$.

6.3 Growth of InP nanowires

There were two aims for the growth of InP nanowires: to first grow pure phase, stacking fault-free nanowires and to then incorporate an InAsP NWQD within the nanowires. Due to time constraints an InAsP heterostructure (ideally a NWQD) was grown within every InP nanowire sample regardless of crystal structure, in order that both aims could be addressed simultaneously. To reduce the potential impact of the growth of a NWQD on the growth of the top part of the nanowire, the NWQD was inserted just one minute before the end of the growth.

Initial nanowire growth conditions were based on a report within the literature describing the transition from polytypic nanowires containing many stacking faults to pure phase InP nanowires with a very low stacking fault density². The transition was found to be a function both of growth temperature and V/III ratio. At a growth temperature of 600°C and V/III ratio of 55 polytypic nanowires were observed, whilst pure phase nanowires were obtained at 660°C and a V/III ratio of 18. Given the variability in growth between different MOCVD reactors it was unlikely that simply copying these conditions would result in identical growth. Furthermore, it was expected that utilising a growth mask which covered the entirety of the substrate surface would result in much faster nanowire growth rates due to the reduced surface area for adatom deposition. This is in contrast to the previous growth of GaAs nanowires (Chapters 3-5) and the growth of InP nanowires in Ref 2. Accordingly, the first growth conditions were chosen to cover a range of growth temperatures from 620°C to 680°C, therefore inclusive of 660°C. By investigating a broad range of growth conditions it was anticipated that both the axial and radial growth rates could be controlled to increase the potential for NWQD formation.

Reference in text	Sample MR No.	Anneal time (s)	Anneal Temp (°C)	Growth Temp (°C)	Source flows (sccm)			Growth time (s)		
					TMIn	PH ₃	AsH ₃	InP	InAsP	InP
6A	3336	540	670	650	0.3	60	12	600	5	60
6B	3337	540	670	650	0.125	60	12	600	5	60
6C	3388	540	670	620	0.125	60	12	600	5	60
6D	3389	540	680	680	0.125	60	12	600	5	60
6E	3413	540	680	680	0.063	60	12	240	1.5	60
6F	3428	540	680	680	0.13	50	12	240	1.5	60

Table 6.1. Summary of samples. The anneal time includes the time taken to reach the annealing temperature from 20°C. Note the growth times refer (from left to right) to the InP nanowire base, the InAsP NWQD and the top section of the InP nanowire.

The six InP samples grown to date are summarised in Table 6.1. All samples were first annealed for 9 minutes under a PH₃ overpressure to remove the native oxide from the substrate. This included the time required to reach the annealing temperature from room temperature. Nanowire growth was observed in the case of all four of the first growth runs, namely Samples 6A–6D. In the following analysis the structural and optical properties of the nanowires are discussed. Where possible the nanowire height was determined, although for the case of small nanowire pitch (in particular 500nm) this was not always achievable, and measurements taken at the sides of an array were distorted by edge effects on the growth rate.

6.3.1 SEM analysis

SEM images of the nanowires from Samples 6A and 6B are shown in Figure 6.2. These samples were grown under identical conditions except for the use of a lower TMIn flow rate for the latter. The nanowires were seen to be vertically orientated with hexagonal facets, although there are some deviations from the perfect hexagon. It is clear that the

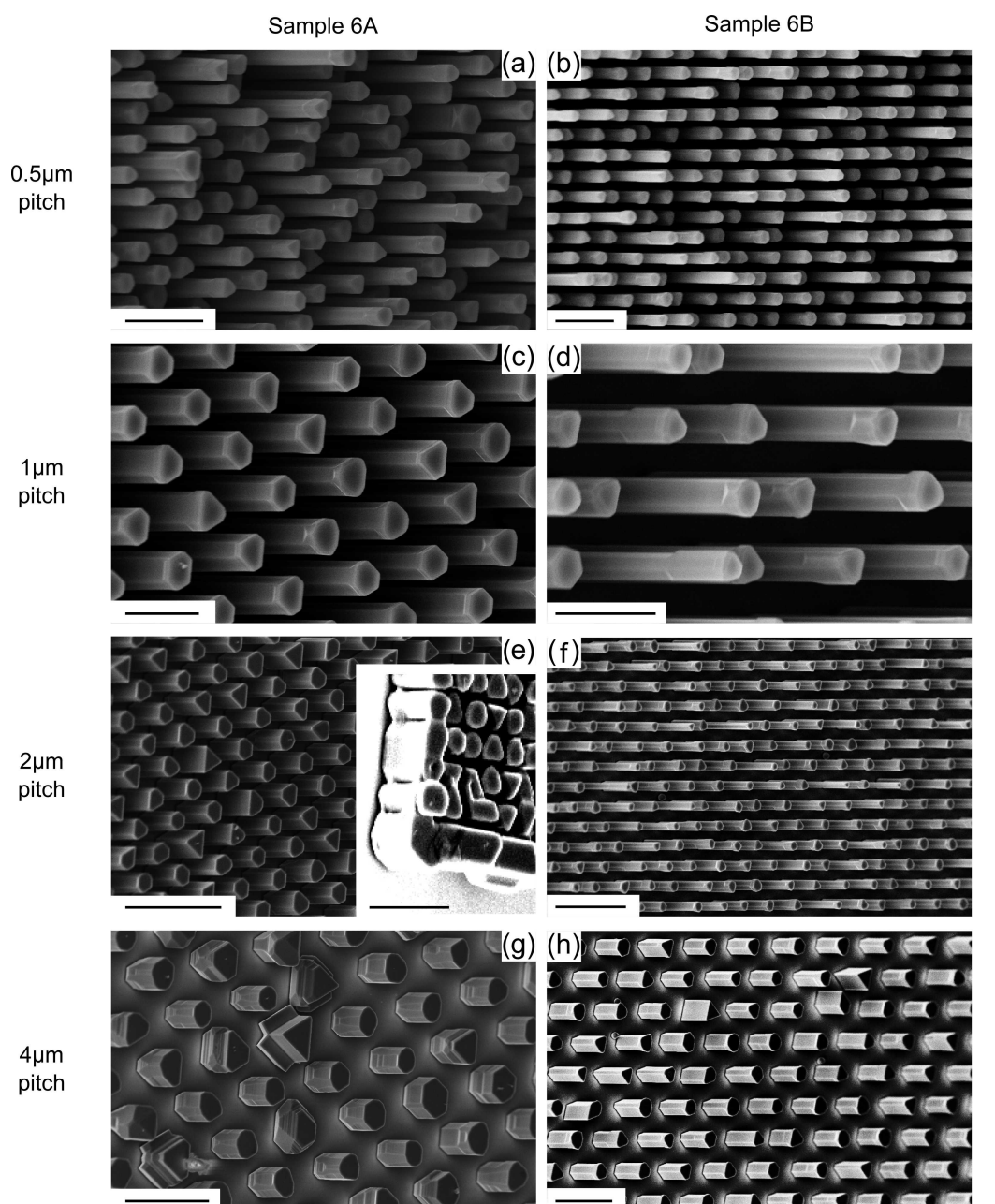


Figure 6.2. SEM images of Samples 6A and 6B. (a, c, e, g) 45° tilted SEM overview images for Sample 6A, for nanowire pitch of 500nm, 1 μm, 2 μm and 4 μm respectively; (e) (Inset) Edge of array showing anomalous growth; (b, d, f, h) Equivalent images for Sample 6B. (a-d) Scale bars 1 μm. (e-h) Scale bars 5 μm.

nanowire side lengths were often different, resulting in a variety of nanowire geometries. In the most extreme cases triangular cross-section nanowires were grown with growth on three of the side facets almost entirely suppressed. The origin for such variation is unknown, but previous experience suggests it may be the result of relatively high nanowire growth rates. In the case of Sample 6A, the nanowires of 4 μm pitch developed numerous additional facets, suggesting the growth conditions were far from ideal in this particular case. Neglecting the edges of the array, nanowire yield across all the arrays on the sample was very high, with few obvious defects. The anomalous growth commonly observed at the edge of each array can be seen in the inset in Figure 6.2(e).

It is apparent that the introduction of AsH_3 to form an InAsP NWQD within the nanowires altered the morphology of the following InP growth. This is particularly clear in Figure 6.2(a) and Figure 6.2(d). As well as increasing the nanowire diameter, in some cases the hexagon was seen to rotate through 90° and therefore the sidewall orientation changed from parallel to the $[110]$ direction to the $[\bar{2}11]$ direction of the InP (111)A substrate². The increase in nanowire diameter has been observed previously for the growth of InP following InAsP within a nanowire³, albeit utilising lower temperature growth of the InAsP NWQD. The origin of the increased radial growth and the potential need to control it to minimise the NWQD radial dimensions will be the subject of future work.

Figure 6.3 summarises the height and diameter of the nanowires as a function of nanowire pitch, alongside the radial and axial growth rates using a linear approximation. For Sample 6A, the nanowire axial growth rate was seen to be comparable to similar reports in the literature³. The nanowire height showed no clear dependence on the pitch for 2 μm

to 4 μm pitch nanowires, being $\sim 2.3 \mu\text{m}$ (linear growth rate 3.5 nm/s). Due to edge effects the height of the smaller pitch nanowires is unknown. However, it is clear that the 500 nm pitch nanowires showed considerable variation in height, whereas for pitches of 1–2 μm the nanowire height uniformity was very good. The radial growth rate showed an approximately linear relationship with the nanowire pitch, varying from $\sim 0.09 \text{ nm/s}$ to 1.32 nm/s for 500 nm to 4 μm pitch nanowires. To interrogate single NWQDs *in-situ* requires a minimum separation of $\sim 2 \mu\text{m}$ (\sim laser spot size), hence the radial growth (which prevents NWQD formation) is problematic in this regard.

The lower TMIn flow rate used for Sample 6B was found to slightly reduce the nanowire radial growth, with a minimum radial thickness of $\sim 35 \text{ nm}$ observed for a nanowire pitch

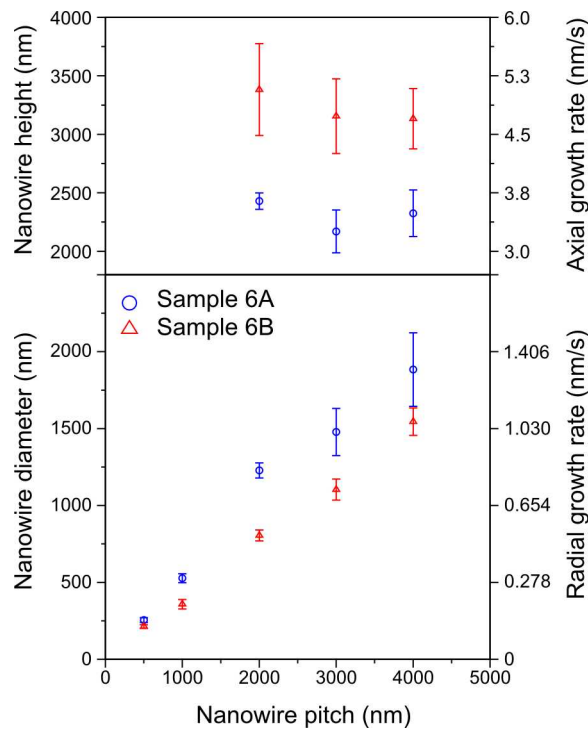


Figure 6.3. Nanowire height and diameter versus pitch for Samples 6A and 6B. (Upper panel) Height and linear axial growth rate versus nanowire pitch. (Lower panel) Diameter and radial growth rate versus nanowire pitch. Note that the right hand axis is nonlinear. Error bars correspond to one standard deviation.

of 500nm, corresponding to a linear growth rate of 0.05nm/s. The radial growth was once more seen to increase in a linear fashion with the nanowire pitch. The axial growth rate however was found to have increased, to ~5nm/s for 2 μ m to 4 μ m pitch nanowires. This suggested that adatoms incorporated preferentially on the (111)A facet under these growth conditions. Similarly to Sample 6A, little dependence on the nanowire pitch was observed. As reducing the TMIn flow rate effectively increased the V/III ratio for precursors, this suggested that the growth regime was different to that used for GaAs nanowires. In that case, an increase in V/III ratio had the opposite effect on the growth rates for the nanowire top and side facets. Similarly to Sample 6A, the nanowires with 500nm pitch showed significant variation in height. Larger values for the pitch produced nanowires with a narrow height distribution. Few defects were observed within the arrays and the yield of nanowires was very high.

To investigate further the reduced radial growth seen in Sample 6B, Samples 6C and 6D were grown using the same precursor flows and growth times but different temperatures, 620°C and 680°C respectively. Figure 6.4 shows representative SEM images of the nanowires grown on these samples. For 500nm pitch nanowires on Sample 6C there was a considerable degree of height variability, which is absent for 1-2 μ m pitch nanowires. There were also signs of tapering towards the tip of the nanowire, although this also seemed to vary from nanowire to nanowire. The 1 μ m pitch nanowires showed the greatest uniformity, although some defects were still evident. As the pitch increased however the number of defects and the general variation in the nanowire morphology increased. For Sample 6D, the nanowire height showed good uniformity for all pitches, and the nanowire diameter was seen to be the narrowest out of Samples 6A–6D. However the defect density was highest on this sample.

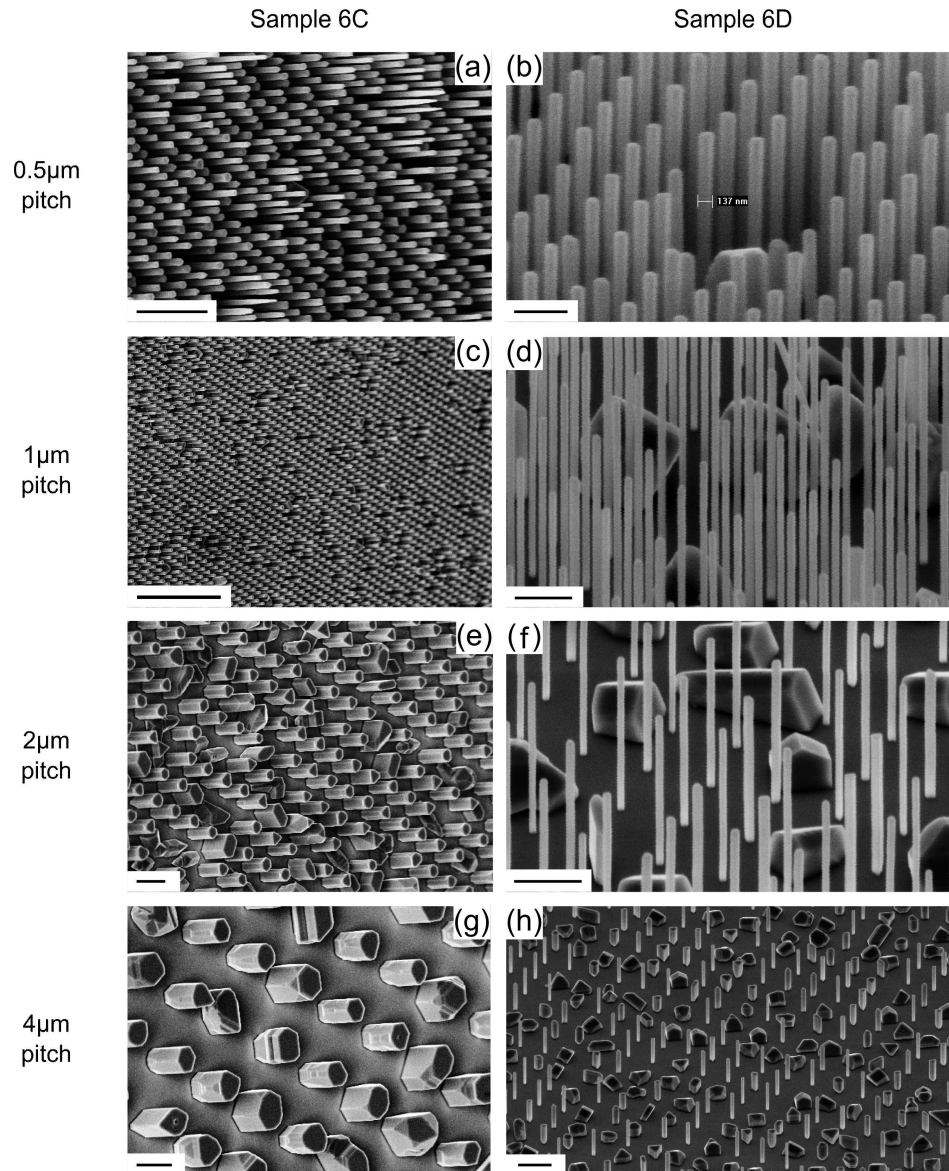


Figure 6.4. SEM images of Samples 6C and 6D. (a, c, e, g) 45° tilted SEM overview images for Sample 6C, for nanowire pitch of 500nm, 1 μm, 2 μm and 4 μm respectively. (b, d, f, h) Equivalent images for Sample 6D. Scale bars (a, e-g) 2 μm (b) 500nm (c) 10 μm (d) 1 μm (h) 5 μm.

Figure 6.5 summarises the height and diameter of the nanowires on Samples 6C and 6D as a function of nanowire pitch. The diameter of the nanowires in Sample 6C was very similar to that of Sample 6B, whilst the axial growth rate was reduced by $\sim 50\%$. There was once more little dependence of the height on the nanowire pitch. For Sample 6D the situation was quite different. The dependence of the diameter on the nanowire pitch was no longer linear, although more data points would be needed to determine the exact relationship. There was also a weak dependence of the nanowire height on the pitch, with the height increasing with decreasing nanowire pitch. Whilst the diameter dependence shows promise for the realisation of individually addressable NWQDs (pitch $\sim 2\mu\text{m}$ or greater) the axial growth rate was much faster in this case, at $\sim 7\text{-}9\text{nm/s}$. This could be

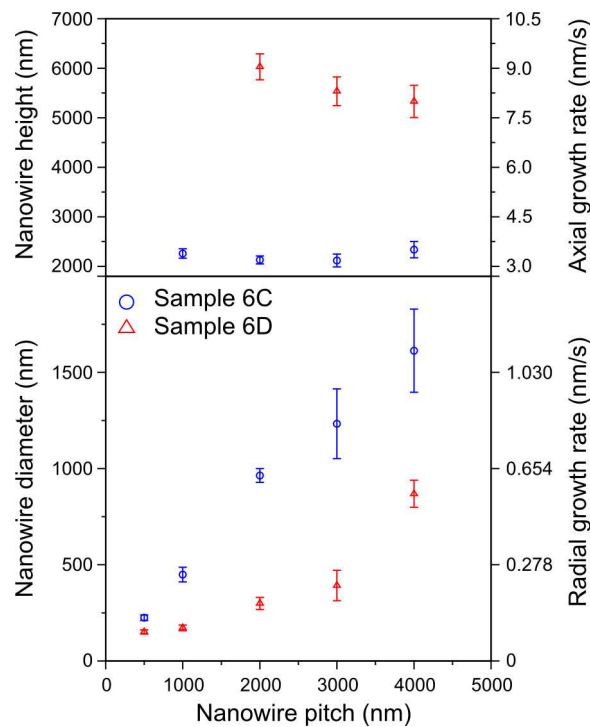


Figure 6.5. Nanowire height and diameter versus pitch for Samples 6C and 6D. (Upper panel) Height and linear axial growth rate versus nanowire pitch. (Lower panel) Diameter and radial growth rate versus nanowire pitch. Note that the right hand axis is nonlinear. Error bars correspond to one standard deviation.

expected to impact on the ability to realise sharp InAsP/InP interfaces within the nanowire.

6.3.2 PL measurements

PL measurements were undertaken using non-resonant HeNe excitation at 632.8nm, with the samples installed in a low temperature flow cryostat. The PL spectra were similar across all four samples and all nanowire pitches. Figure 6.6(a) shows representative spectra taken from various locations across an array of 500nm pitch nanowires on Sample 6C. A broad range of PL emission energies could be observed. For a polytypic InP nanowire, the lowest energy PL emission is governed by recombination of the electron in a bulk zinc blende region with a hole in a neighbouring wurtzite section of the nanowire. Based on low temperature band offsets proposed within the literature⁸, the low energy limit for recombination is $\sim 1.36\text{eV}$. The upper energy limit is equal to the wurtzite InP bandgap energy of $\sim 1.49\text{eV}$. Between these limits transitions can occur at any energy, dependent on the axial height and spatial occurrence of individual zinc blende and wurtzite sections of the nanowire. This is shown schematically in Figure 6.6(c). The low temperature PL spectrum from polytypic InP nanowires is thus characterised by a broad range of emission energies decreasing from the InP wurtzite bandgap of 1.49eV to $\sim 1.36\text{eV}$ ^{8,9}. For sufficiently short sections of wurtzite and zinc blende axial carrier confinement may occur. Recombination of confined states in opposite crystal phases may then resemble that of a quantum dot for a sufficiently narrow nanowire. This has been termed crystal phase quantum dot emission⁹.

Photons detected at energies lower than $\sim 1.36\text{eV}$ potentially originate within the lower bandgap InAsP section of the nanowire. Figure 6.6(b) shows a particularly clear example

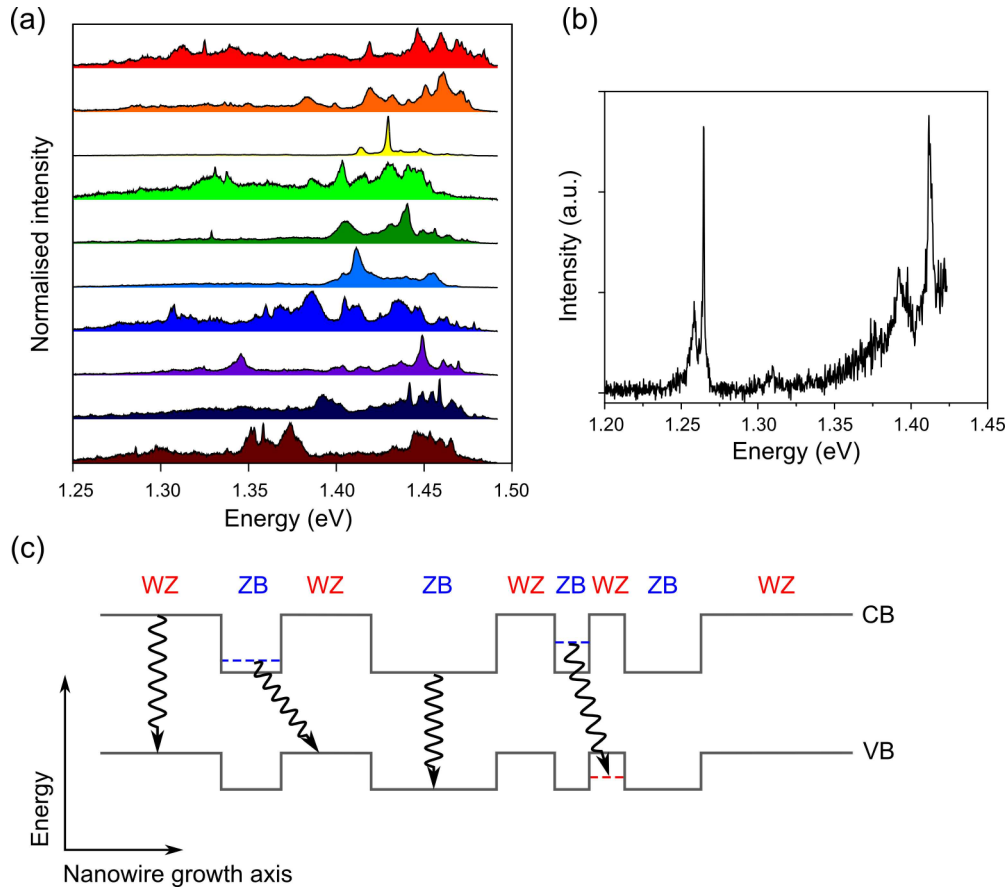


Figure 6.6. PL spectra for InP nanowires. (a) Normalised PL spectra obtained at different locations on a 500nm pitch array. Spectra offset in y for clarity; (b) PL spectrum for 2 μm pitch nanowire array; (c) Schematic band diagram demonstrating carrier recombination in polytypic InP nanowires. Four possible interband recombination pathways are shown. Dashed lines denote confined energy states. ZB – zinc blende, WZ – wurtzite, CB – conduction band, VB – valence band.

of sharp PL emission lines below the minimum energy associated with exciton recombination in polytypic InP, and is thus attributed to recombination within the InAsP region of the nanowire. It is quite possible however that the emission seen here was due to InAsP stacking faults, and no excited states were observed at higher pump power. The conclusion from PL measurements on Samples 6A–6D was that the nanowires were

polytypic, and whilst there was evidence for emission from an InAsP region within the nanowires there was no clear sign of NWQD emission. The PL measurements provided a clear description of the internal structure of the nanowires hence time consuming TEM measurements were not required.

6.3.3 Further development

The significant radial growth observed for the majority of the nanowires in Samples 6A–6D is not necessarily a hindrance, and the resulting nanowires could be of interest for use as efficient absorbing elements in nanowire solar cells. The high nanowire growth rate for Sample 6D would also be beneficial as it would increase throughput in a commercial setting. For solar cell applications the apparently polytypic nature of the nanowires is unlikely to be of major importance, as the small band offsets between wurtzite and zinc blende InP nanowire phases⁸ would provide limited carrier trapping at room temperature and may actually increase the operating voltage⁶. However from the perspective of NWQD formation, the presence of polytypism is much more significant as it introduces spectral diffusion effects as well as reducing the probability for single photon emission. Furthermore, extremely fast growth rates are thought likely to influence the ability to realize an InAsP NWQD within the InP nanowires. For instance, As-P intermixing at the InP/InAsP interface might be exacerbated by high growth rates giving insufficient time for removal of the undesired precursor from the reactor. In order to address this issue, further growth runs were attempted utilising a double dilution PH₃ channel, which enabled reduced flow rates between 5sccm and 50sccm to be measured. In contrast, the 60sccm flow rate which was used for Samples 6A–6D was at the lower limit of what could be measured with the mass flow controller monitoring the single dilution PH₃

channel. Initially the TMI_n flow was also reduced in order that the total flow of precursors was significantly reduced.

Utilising the double dilution channel, at first it was not possible to obtain nanowires (Sample 6E). Instead, unstructured growths were observed in the nanoholes, and the volume of deposited material was much reduced relative to the previous growth runs. This may not have been solely due to the lower precursor flow rates, as the formation of facets with varying growth rates is important for nanowire growth, and it is possible that the lack of such facets prevented the random structures growing at a similar net rate. To mimic the growth conditions of the most recent successful sample (Sample 6D) most closely, the growth was repeated using a PH₃ flow of 50sccm (it was not possible to utilise a flow of 60sccm with the double dilution channel). In order to try and prevent excessive defect formation, the growth time for the first InP section of the nanowire was also reduced from 9 minutes to 4 minutes.

The resulting nanowires for Sample 6F are shown in Figure 6.7. It is clear that whilst nanowires with uniform height were obtained for the 500nm and 1μm pitch arrays, the number of defects within the array increased significantly relative to Sample 6D. The lack of growth on the SiO₂ mask away from the patterned arrays suggests the defective growth originated within the nanoholes, but for some reason failed to produce the facets required for nanowire growth. As the pitch increased further to 2μm and then 3μm the yield of nanowires was seen to decrease with a concomitant increase in defect formation.

The limited success of this growth run raises an important question regarding the accuracy of the mass flow controller used for Samples 6A–6D, for which a 60sccm flow was measured. If this value was indeed correct then there may only exist a narrow range

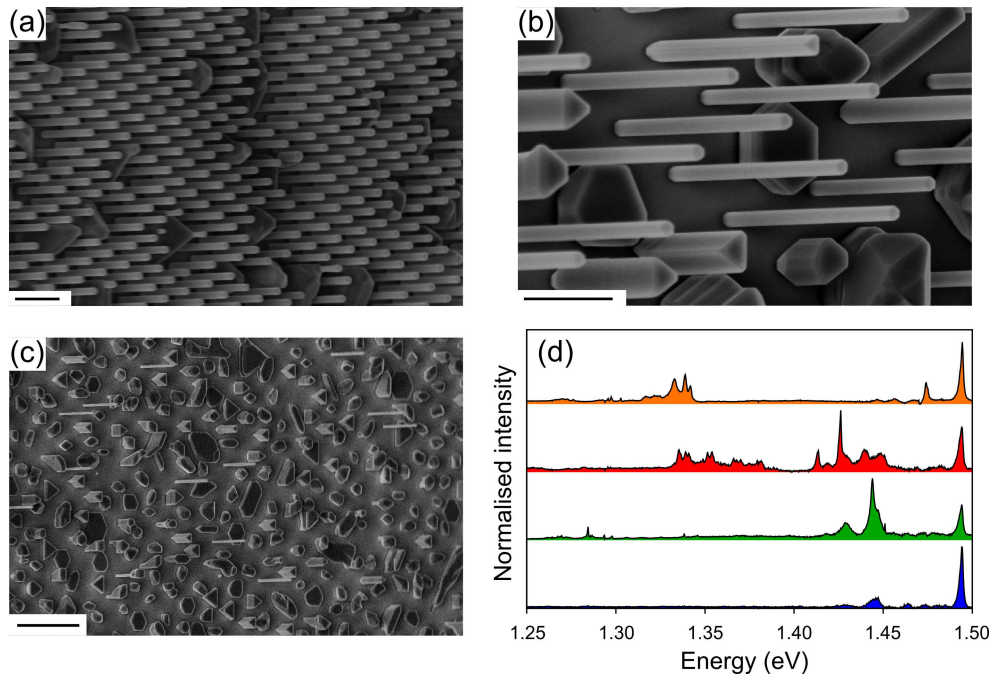


Figure 6.7. SEM images and PL spectra for Sample 6F. SEM images of (a) 500nm pitch (b) 1 μ m pitch and (c) 2 μ m pitch nanowires. Scale bars (a) 1 μ m (b-c) 5 μ m; (d) Normalised PL spectra for different locations across a 500nm pitch array. Spectra offset in y for clarity.

of conditions for which the PH_3 flow can be adjusted in an attempt to reduce the axial growth rate for the case of full SiO_2 coverage of the substrate. This leaves the growth temperature and the TMIn flow rate as the main controls on the growth rate. It is important also to bear in mind that the main aim is to achieve pure phase nanowires. PL spectra from 500nm pitch nanowires on Sample 6F are shown in Figure 6.7(d). The wurtzite InP free exciton transition at $\sim 1.49\text{eV}$ is clearly observed in the spectra. It is evident however that the nanowires are once more polytypic, with a range of emission energies below 1.49eV, as well as emission below $\sim 1.36\text{eV}$ which may be ascribed to the InAsP section of the nanowire. It is possible that a combination of pure phase nanowires

growing at lower growth rates than seen presently is not obtainable on full SiO₂ coverage wafers. Further growth is necessary to evaluate the merits of the competing approaches.

6.4 Conclusion

The catalyst-free growth of InP nanowires on InP (111)A substrates has been developed. The substrates were fully covered by the SiO₂ growth mask, in order to ensure repeatability between samples. This however presented a challenge for the control of the nanowire growth rate, and a much increased radial growth rate was evident at the edge of an array. Growth at an array edge was typically unstructured rather than forming nanowires. SEM analysis revealed that nanowires grown at the highest temperature of 680°C showed the least radial growth, although the vertical growth rate was much increased relative to that at lower temperature. The rate of defect formation was also increased at higher temperature. First attempts to reduce both the axial growth rate and the formation of defects by lowering the PH₃ flow were unsuccessful. PL measurements showed that all the nanowires grown were polytypic, and further growth studies are required to obtain pure phase nanowires before focus turns to formation of InAsP NWQDs.

Bibliography

- (1) Dalacu, D.; Mnaymneh, K.; Lapointe, J.; Wu, X.; Poole, P. J.; Bulgarini, G.; Zwiller, V.; Reimer, M. E. *Nano Lett.* **2012**, *12*, 5919–23.
- (2) Kitauchi, Y.; Kobayashi, Y.; Tomioka, K.; Hara, S.; Hiruma, K.; Fukui, T.; Motohisa, J. *Nano Lett.* **2010**, *10*, 1699–703.
- (3) Dorenbos, S. N.; Sasakura, H.; van Kouwen, M. P.; Akopian, N.; Adachi, S.; Namekata, N.; Jo, M.; Motohisa, J.; Kobayashi, Y.; Tomioka, K.; Fukui, T.; Inoue, S.; Kumano, H.; Natarajan, C. M.; Hadfield, R. H.; Zijlstra, T.; Klapwijk, T. M.; Zwiller, V.; Suemune, I. *Appl. Phys. Lett.* **2010**, *97*, 171106.
- (4) Minot, E. D.; Kelkensberg, F.; van Kouwen, M.; van Dam, J. A.; Kouwenhoven, L. P.; Zwiller, V.; Borgström, M. T.; Wunnicke, O.; Verheijen, M. A.; Bakkers, E. P. A. M. *Nano Lett.* **2007**, *7*, 367–71.
- (5) Joyce, H. J.; Wong-Leung, J.; Yong, C.-K.; Docherty, C. J.; Paiman, S.; Gao, Q.; Tan, H. H.; Jagadish, C.; Lloyd-Hughes, J.; Herz, L. M.; Johnston, M. B. *Nano Lett.* **2012**, *12*, 5325–30.
- (6) Wallentin, J.; Anttu, N.; Asoli, D.; Huffman, M.; Aberg, I.; Magnusson, M. H.; Siefer, G.; Fuss-Kailuweit, P.; Dimroth, F.; Witzigmann, B.; Xu, H. Q.; Samuelson, L.; Deppert, K.; Borgström, M. T. *Science* **2013**, *339*, 1057–60.
- (7) Inari, M.; Takeda, J.; Motohisa, J.; Fukui, T. *Phys. E Low-dimensional Syst. Nanostructures* **2004**, *21*, 620–624.
- (8) Jancu, J.-M.; Gauthron, K.; Largeau, L.; Patriarche, G.; Harmand, J.-C.; Voisin, P. *Appl. Phys. Lett.* **2010**, *97*, 041910.
- (9) Akopian, N.; Patriarche, G.; Liu, L.; Harmand, J.-C.; Zwiller, V. *Nano Lett.* **2010**, *10*, 1198–201.

7 Conclusions and outlook

In the following, the key results of Chapters 2-6 are summarised. An outlook giving directions for further development of catalyst-free nanowire research is then presented.

7.1 Chapter summaries

7.1.1 Chapter 2

Nanowires have been receiving considerable recent interest due to their potential to form the optically active component in a new generation of efficient solar cells. To date, the majority of research has focussed on three regimes of operation: single nanowire solar cells, with potential to power nano-electronic devices; efficient anti-reflection coatings in the form of vertically orientated nanowire arrays; and nanowire arrays as the active layer in single junction solar cells. In this chapter, the efficiency limits of a tandem nanowire-planar solar cell were evaluated using a modified form of the detailed balance theory. An efficiency limit of 43.3% was determined for the case in which the nanowire array absorbs 95% of above bandgap photons. Intriguingly, this occurs for the case in which the array is grown on a silicon substrate, allowing the experimentalist to leverage both the maturity of silicon processing technology and the appealing optical and structural properties of nanowires and nanowires arrays. This work provides the first design criteria for the experimental realisation of the nanowire-planar tandem solar cell.

7.1.2 Chapter 3

In this chapter, the development of the growth of GaAs nanowires by a catalyst-free technique was presented. This acted as a basis for the following chapters of the thesis. A detailed description of the pre-growth fabrication was followed by structural characterisation of the first nanowire samples grown during the course of this research. Two growth regimes were identified. Initially, nanowire growth varied considerably from sample to sample, and this was found to depend on the simultaneous observation of planar growth with a high surface roughness in unpatterned regions of the substrate. Improvement of the pre-growth fabrication process, in particular the final treatment of the wafer prior to growth, was shown to result in smooth planar growth, and this resulted in much more reproducible nanowire growth.

7.1.3 Chapter 4

This chapter discussed the growth of InGaAs nanowire quantum dots (NWQDs) within GaAs nanowires, building on the growth development reported in Chapter 3. The NWQDs were extensively characterised using a combination of photoluminescence and electron microscope techniques. Exciton PL linewidths down to $\sim 140\mu\text{eV}$ were observed. Single photon emission from an individual NWQD was demonstrated, and a low ensemble broadening of $\sim 15\text{meV}$ was measured for an array of nanowires with the same nominal diameter (120-140nm). The unexpectedly large excited state splitting observed for the NWQDs was explained by introducing an additional radial harmonic confinement potential, which was thought to originate from an indium composition profile across the radius of the NWQD. Long PL lifetimes ($\sim 10\text{ns}$) were consistent with previous reports, either for nanowires containing rotational twins or spontaneous emission suppression due

to a reduction in the photonic density of states in the narrow nanowire. Spectral diffusion due to temporally variable charge trapping at rotational twin interfaces was suggested as the likely origin of linewidth broadening. In addition, laser annealing of a NWQD was demonstrated, resulting in a blueshift in the exciton energy of $\sim 1\text{meV}$, and the growth of nanowires containing two NWQDs was also undertaken. This work represents the first detailed study into arrays of catalyst-free InGaAs NWQDs.

7.1.4 Chapter 5

Control of the nanowire morphology using the catalyst-free growth approach was demonstrated for the first time. By fabricating nanoslots or pairs of nanoholes in close proximity, nanowires with elongated cross-section were grown. The elongation ratio was seen to be continuously variable. An InGaAs heterostructure grown within an elongated nanowire was shown to emit linearly polarized light when measured from the top facet of the nanowire, with a measured polarization ratio of 80-90%. The axis of polarization was coincident with the elongation axis of the nanowire. This provides a bottom-up, scalable platform for the formation of linearly polarized single photon sources. A promising growth scheme allowing the realisation of a well confined NWQD in an elongated cross-section nanowire was proposed, utilising a combination of VLS and selective area growth techniques.

7.1.5 Chapter 6

The development of the catalyst-free growth of InP nanowires containing an InAsP NWQD was introduced in this chapter. This was motivated by the potential to produce stacking fault-free nanowires in this materials system, and therefore to reduce the linewidth broadening effects observed in the InGaAs NWQD emission reported in this

thesis. The samples showed PL emission over a broad range of energies ($\sim 1.36\text{eV}$ to 1.49eV) demonstrating that they were polytypic in nature. Some of the PL emission lines were narrow, suggesting the formation of crystal phase quantum dots within the nanowires. Emission at lower energy ($< 1.36\text{eV}$) was thought to be evidence of the successful realisation of an InAsP heterostructure within the nanowire. Control of the nanowire radial growth was demonstrated through use of a higher growth temperature (680°C) and variation of the source fluxes. This was evidenced by the almost complete elimination of radial growth in nanowires of 500nm pitch. Whilst at the very earliest stage of research, this work has promise for the production of high optical quality NWQDs.

7.3 Outlook

Significant developmental work has been presented in this thesis, opening up many future research directions. Four of these are briefly discussed in the following sections.

7.3.1 Nanowire-on-silicon tandem solar cells

In Chapter 2 design criteria for a tandem solar cell formed from a nanowire array grown on a planar substrate were presented, with a notable finding being the possibility for high efficiency devices utilising heterogeneous nanowire growth on silicon. Such growth has been the subject of increasing interest¹⁻³ and is particularly appealing due to the low cost of silicon substrates. Challenges in this regard include the possible requirement for high temperature removal of the native oxide on silicon (beyond the capabilities of many MOCVD reactors) and the growth of polar III-V semiconductors on non-polar silicon. The latter can lead to non-vertical nanowire growth. Pre-growth removal of the native oxide from silicon using an HF etch has shown promising results allowing for a lower temperature growth process. Mechanisms for the promotion of vertical nanowire growth have also been demonstrated⁴. Growth on silicon in this vein is now being undertaken within the LDS research group at the University of Sheffield. This technology has the potential to have a disruptive impact on the solar cell market.

7.3.2 Control of nanowire crystal structure

The optical quality of NWQDs has improved markedly over the past few years. As well as the high degree of homogeneity and PL linewidths down to $\sim 140\mu\text{eV}$ demonstrated in this thesis for the InGaAs materials system, very narrow PL linewidths down to $3\mu\text{eV}$ have been recently demonstrated for InAsP NWQDs⁵. Previous successes in the area of InAsP NWQDs⁶ and control of the InP nanowire crystal structure⁷ inspired the work on InP nanowires presented in this thesis, and the first signs of both have been seen in samples grown at Sheffield. A power-dependent PL spectrum from an array of InP nanowires with 250nm pitch is shown in Figure 7.1. The nanowires had a diameter of $\sim 100\text{nm}$, and the growth procedure included an InAsP NWQD. PL emission can be observed at the bandgap energy for wurtzite InP ($\sim 1.49\text{eV}$), whilst the only emission below this energy consists of a few narrow lines at low pump power and the apparent

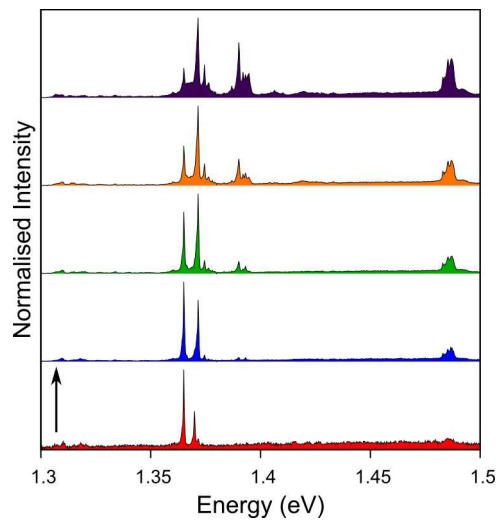


Figure 7.1. Normalised power dependent PL spectra for 100nm diameter InP nanowires with a pitch of 250nm. The nanowires contain an InAsP NWQD. The arrow denotes increasing laser pump power. Spectra offset in y for clarity.

filling of higher energy states at high power. Due to the small nanowire pitch the laser spot excited ~ 28 nanowires. The PL emission below the wurtzite bandgap energy could therefore be evidence of a low yield of NWQDs within the array. It is unlikely that it is due to stacking faults, as the likelihood of only one or two stacking faults occurring in 28 nanowires is thought to be very low. This suggests that the nanowires were purely wurtzite in crystal phase.

Promising results have also been reported elsewhere regarding the control of crystal phase in catalyst-free GaAs nanowires, using a new nanotemplate technique^{8,9}. The materials choice for high crystalline quality NWQDs is thus expanding.

7.3.3 Exploring the limits of catalyst-free nanowire growth

A new technique to control the morphology of catalyst-free nanowires was presented in Chapter 5, allowing for the scalable, bottom-up growth of linearly polarized photon sources. Work is on-going to ensure single photon emission from such structures, which are of particular interest as photon sources for quantum information applications. In a similar manner, definition of the nucleation areas for nanowire growth using EBL patterning allows the formation of nanowire clusters and more complicated arrangements, with the potential for study of cooperative NWQD emission and optomechanical interactions between nanowires.

A requirement in this regard is a 100% yield of nanowires within a cluster. As mentioned in Chapter 4, a significant improvement in the site-to-site repeatability of the catalyst-free nanowire growth was found by etching the patterned substrates for ~ 2 s in 1% HF prior to the final cleaning step before growth. An array of GaAs nanowires with a diameter of 65nm is shown in Figure 7.2(a), demonstrating the high yield now achievable. Representative SEM images of initial growth of closely spaced lines of nanowires are shown in Figure 7.2(b) and Figure 7.2(c). The combination of these structures with an open cavity system developed at Sheffield will allow much interesting physics to be explored in the near future.

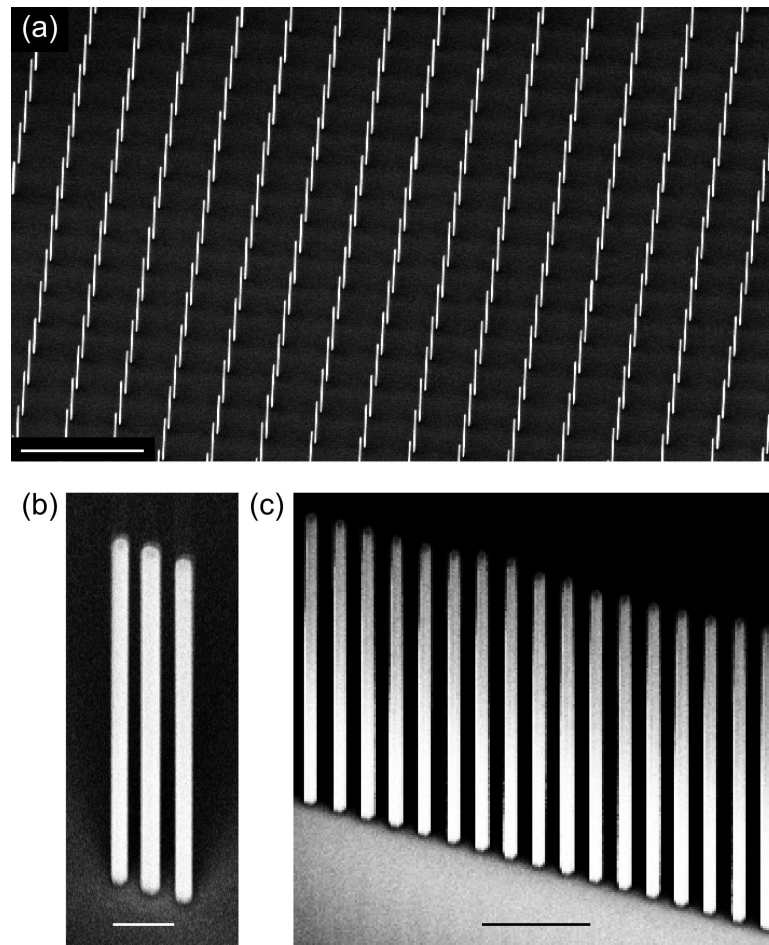


Figure 7.2. SEM images of GaAs nanowires. (a) Array of 65nm diameter nanowires with almost 100% yield; (b) triple and (c) multiple nanowires. Scales bars (a) 10 μ m (b) 500nm (c) 1 μ m. The apparent tapering at the top of the nanowires in (c) is an artefact of the imaging process.

7.3.4 NWQD integration with photonic crystals

Two promising routes towards integration of NWQDs with photonic crystals have been identified, with the ultimate aim of creating a scalable architecture for quantum computing. The first of these concerns a more short term goal, in which a few nanowires could be integrated within slot photonic crystal cavities. The placement of a nanowire within such a cavity has been shown theoretically to allow the realisation of a high optical quality factor device¹⁰. Nanomanipulation in this manner is technologically feasible. A possible fabrication route is shown in Figure 7.3. Typically a 2D photonic crystal is under-etched to provide optical confinement in the direction perpendicular to the plane of the crystal via total internal reflection. A standard depth of 140nm is used for photonic crystals fabricated in Sheffield. This provides an upper limit on the diameter of the nanowire that could be placed in a slot within the crystal. It is thought that the polytypic PL emission observed from InP nanowires could be leveraged in such a device, as at least

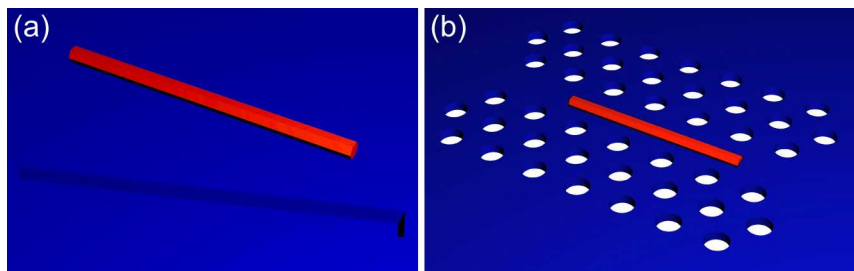


Figure 7.3. Nanowire integration with a slot photonic crystal cavity. (a) Nanowires are dispersed onto a host substrate containing pre-etched rectangular slots (foreground); (b) A single nanowire is manipulated into the slot, before a 2D photonic crystal is patterned around the nanowire. An under-etch can then be undertaken to ensure the photonic crystal is surrounded by air, providing total internal reflection confinement in the direction perpendicular to the plane.

one of the many emission locations in such a nanowire is likely to overlap with a field antinode within the cavity.

Whilst the above is appealing for limited scale up, a longer term aim involves the overgrowth of vertically orientated nanowires, using the defined location of the nanowire to enable accurate fabrication of photonic crystals around the NWQDs. The nanowires must first be grown on a substrate containing an AlGaAs sacrificial layer. A particular challenge is to grow high aluminium content AlGaAs on the (111)B GaAs substrate, although this is not thought to be insurmountable. First attempts at planar overgrowth have already been undertaken at Sheffield.

Bibliography

- (1) Roest, A. L.; Verheijen, M. a; Wunnicke, O.; Serafin, S.; Wondergem, H.; Bakkers, E. P. a M. *Nanotechnology* **2006**, *17*, S271–S275.
- (2) Mårtensson, T.; Svensson, C. P. T.; Wacaser, B. A.; Larsson, M. W.; Seifert, W.; Deppert, K.; Gustafsson, A.; Wallenberg, L. R.; Samuelson, L. *Nano Lett.* **2004**, *4*, 1987–1990.
- (3) Tomioka, K.; Yoshimura, M.; Fukui, T. *Nature* **2012**, *488*, 189–193.
- (4) Tomioka, K.; Tanaka, T.; Hara, S.; Hiruma, K.; Fukui, T. *IEEE J. Sel. Top. Quantum Electron.* **2011**, *17*, 1112–1129.
- (5) Reimer, M. E. Gaussian single photon emission from quantum dots intapered nanowire waveguides. Presented at International Conference on One-Dimensional Nanomaterials, Annecy, France, 24th September **2013**.
- (6) Dalacu, D.; Mnaymneh, K.; Lapointe, J.; Wu, X.; Poole, P. J.; Bulgarini, G.; Zwiller, V.; Reimer, M. E. *Nano Lett.* **2012**, *12*, 5919–23.
- (7) Kitauchi, Y.; Kobayashi, Y.; Tomioka, K.; Hara, S.; Hiruma, K.; Fukui, T.; Motohisa, J. *Nano Lett.* **2010**, *10*, 1699–703.
- (8) Kanungo, P. Das; Schmid, H.; Björk, M. T.; Gignac, L. M.; Breslin, C.; Bruley, J.; Bessire, C. D.; Riel, H. *Nanotechnology* **2013**, *24*, 225304.
- (9) Borg, B. M. Integration of III-V nanowires on silicon using nanotube templates. Presented at International Conference on One-Dimensional Nanomaterials, Annecy, France, 24th September **2013**.
- (10) Danang Birowosuto, M.; Yokoo, A.; Taniyama, H.; Kuramochi, E.; Takiguchi, M.; Notomi, M. *J. Appl. Phys.* **2012**, *112*, 113106.